Electro-thermal Modeling of Lithium-ion Batteries

by

Maryam Yazdan Pour

M.Sc., Iran University of Science and Technology, 2011

B.Sc., Bahonar University, 2007

Thesis Submitted in Partial Fulfillment
of the Requirements for the Degree of

Doctor of Philosophy

in the
School of Mechatronic Systems Engineering
Faculty of Applied Sciences

SIMON FRASER UNIVERSITY
Summer 2015

APPROVAL

Name: Maryam Yazdan Pour

Degree: Doctor of Philosophy

Title: Electro-thermal Modeling of Lithium-ion Batteries

Examining Committee:

Chair: Woo Soo Kim

Associate Professor

Majid Bahrami

Senior Supervisor

Associate Professor

Byron Gates

Supervisor committee

Associate Professor

Krishna Vijayaraghavan

Supervisor committee

Associate Professor

Jason Wang

Internal Examiner

Mechatronic Systems Engineering,

Simon Fraser University

Associate Professor

Zuomin Dong

External Examiner

Professor

Department of Mechanical Engineering

University of Victoria

Date Approved: ....., 2015

Abstract

The development and implementation of Lithium-ion (Li-ion) batteries, particularly in automotive applications, requires substantial diagnostic and practical modeling efforts to fully understand the thermal characteristics in the batteries across various operating conditions. Thermal modeling prompts the understanding of the battery thermal behavior beyond what is possible from experiments and it provides a basis for exploring thermal management strategies for batteries in hybrid electric vehicles (HEVs) and electric vehicles (EVs). These models should be sufficiently robust and computationally effective to be favorable for real time applications. The objective of this research is to develop a complete range of modeling approaches, from full numerical to analytical models, as a fast simulation tool for predicting the temperature distribution inside the pouch-type batteries.

In the first part of the study, a series of analytical models is proposed to describe distributions of potential and current density in the electrodes along with the temperature field in Li-ion batteries during standard galvanostatic processes. First, a three-dimensional analytical solution is developed for temperature profile inside the Li-ion batteries. The solution is used to describe the special and temporal temperature evolution inside a pouch-type Li-ion cell subjected to the convective cooling at its surfaces. The results are successfully verified with the result of an independent numerical simulation. The solution is also adapted to study the thermal behavior of the prismatic and cylindrical-type nickel metal hydride battery (NiMH) batteries during fast charging processes, which demonstrated the versatility of the model. Afterward, to resolve the interplay of electrical and thermal processes on the heat generation and thermal processes, a closed-form model is developed for the electrical field inside the battery electrodes. The solution is coupled to the transient thermal model through the heat source term (Joulean heat). The results of the proposed multi-physics

model are validated through comparison with the experimental and numerical studies for standard constant current discharge tests. The model results show that the maximum temperature in the battery arises at the vicinity of the tabs, where the ohmic heat is established as a result of the convergence/divergence of the current streamlines.

In the second part of the study, an equivalent circuit model (ECM) is developed to simulate the current-voltage characteristics of the battery during transiently changing load profiles. The ECM that is calibrated by a set of characterization tests collected over a wide range of temperature, then coupled with a numerical electro-thermal model. The validated ECM-based model is capable of predicting the time variation of the surface temperature, voltage, and state of charge (SOC) of the battery during different driving cycles and environmental temperatures.

Keywords: Lithium-ion batteries; Thermal management system; Electro-thermal model; Equivalent circuit model; Integral-transformation technique; Separation of variables

To my beloved parents, my dear sisters, and my best friend Mehran

Acknowledgements

This PhD's thesis would be an end to a journey which could have never been walked through without the help and support of the kind people around me, to only some of whom it may be possible to give particular mention in here.

First and foremost, I would like to express my sincere gratitude to my supervisor, Dr. Majid Bahrami, whose support, direction, guidance and encouragement made it possible for this thesis to see the light of this day. His encouraging words throughout my research motivated and kept me going which was invaluable to my thesis.

I am also indebted to Dr. Peyman Taheri for his persistent support, understanding attitude and his never ending patience, not to mention his insightful advice and unsurpassed knowledge, without which this project could have never seen its end.

I would like to express my gratitude to Dr. Gates and Dr. Vijayaraghavan for the useful discussion and comments, which helped me to pursue it goals. I would also like to thank Dr. Jason Wang and Dr. Zuomin Dong for their time reading this thesis and helping to refine it.

I am deeply grateful to my colleagues and lab mates at Laboratory for Alternative Energy Conversion at Simon Fraser University. Their helps, comments, and assistance played an important role in the development of this thesis. In particular, I want to thank Marius Haiducu and Dr. Brian Fraser who helped me accomplish my experiments. Also, I acknowledge Dr. Claire McCague for kindly reviewing and commenting on this writing.

I have to thank my family that have endlessly encouraged and supported me through all stages of my life. Without their presence and support no achievement was possible in my life. My heartfelt appreciation goes to all my friends who were a family to me in these

years; particularly to my dearest fellows; Hossein, Soheil, Arash, Kambiz, and Fattane for all our memorable days and for being on my side, in days of joy and desperation.

And last, but by no means the least, I thank my family and my best friend Mehran for all their love and encouragement. My most special thanks would go to my beloved parents who raised me with love and supported me in all my pursuits.

Thank you all.

Maryam Yazdan Pour

Simon Fraser University

July 2015

Contents

List of Tables

List of Figures

Symbols

General symbols

A	total surface area (m^2)
A_{ij}	areas of individual surfaces (m^2)
a	width of electrode (m)
b	width of tab (m)
Bi_{ij}	Biot numbers at individual surfaces
Bi_{Avg}	surface-averaged Biot number
c	height of electrode (m)
c_p	heat capacity ($J\,kg^{-1}K^{-1}$)
$\mathscr{C}_l$	interpolation coefficients for Y_{ec}
$\mathscr{C}_T$	temperature coefficient for Y_{ec}
$\mathscr{D}_m$	interpolation coefficients for V_{oc}
$\mathscr{D}_T$	temperature coefficients for V_{oc}
e	distance of tab centre from y-axis (m)
F	Faraday constant ($A\,s\,mol^{-1}$)
E°	electrochemical energy of charging (J)
E_{th}	thermal energy of charging (J)
E_{tot}	total energy of charging (J)
$\dot{g}$	heat generation rate ($W\,m^{-3}$)
$\dot{g}_{ohmic}$	ohmic heat generation rate ($W\,m^{-3}$)
$\dot{G}$	source for temperature rise due to initial temperature (K)
$\dot{G}_0$	source for temperature rise (K)
$\dot{G}_{irrev}$	irreversible part of $\dot{G}$ (K)
$\dot{G}_{rev}$	reversible part of $\dot{G}$ (K)
H	ratio of convective to conduction heat transfer coefficients, h/k (m^{-1})

ΔH standard enthalpy of formation ($\mathrm{kJ\,mol^{-1}}$)

h_{ij} convective heat transfer coefficients at surfaces ($\mathrm{W\,m^{-2}\,K^{-1}}$)

$h_{c,ij}$ convective heat transfer coefficients at individual surfaces ($\mathrm{W\,m^{-2}\,K^{-1}}$)

I total charge/discharge current (A)

i in-plane current density ($\mathrm{A\,m^{-2}}$)

I_1 current of charging reaction (A)

I_2 current of oxygen cycle reaction (A)

J reaction current density ($\mathrm{A\,m^{-2}}$)

K_i dimensionless thermal conductivity in x_i direction

ℓ thickness (m)

L height of battery core in Z direction (m)

L_i dimension of battery core in x_i direction (m)

l_c thickness of can (mm)

m mass (kg)

N number of layers in battery core

n electric charge number

$\mathbf{n}$ unit normal vector on electrode

Q capacity (A h)

q in-plane heat flux ($\mathrm{W\,m^{-2}\,K^{-1}}$)

$q_{c,ij}$ convective heat fluxes at individual surfaces ($\mathrm{W\,m^{-2}}$)

q_{diss} heat dissipation flux ($\mathrm{W\,m^{-2}}$)

R_z apparent DC resistance of battery

R radius of battery core (m)

R_d internal resistance (Ω)

r position in r direction (m)

T core temperature (K)

T_0 ambient and initial temperatures (K)

T_{ij} surface temperatures (K)

t time (s)

V operational battery voltage (V)

V_{oc} open circuit potential (V)

$\mathscr{V}$ volume of battery core ($\mathrm{m^3}$)

x	position in Cartesian coordinate system (m)
y	vertical position (m)
Y_{ec}	conductance (S m^{-2})
z	position in z-direction (m)
BMS	battery management system
BTMS	battery thermal management system
ECM	equivalent circuit model
H/PEH	hybrid and plug-in electric vehicle
EV	electric vehicle
Li-ion	lithium-ion
NiMH	nickel-metal hydride
RC	resistance capacitor
VRLA	valve regulated lead-acid

Greek

α_i	normalization factors for eigenfunctions
α	eigenvalues
β	eigenvalues
γ	eigenvalue
δ	thickness (m)
ε	porosity
η_i	normalization factors for eigenfunctions in x_i direction
θ	core temperature rise (K)
θ_{ij}	temperature rise at surfaces (K)
ν	volume fraction
κ	thermal conductivity
λ_i	eigenvalues in x_i direction
ξ_i	dimensionless position in Cartesian coordinate system
ρ	mass density ($\mathrm{kg\,m^{-3}}$)
τ	dimensionless time
Φ	transformation kernel
ϕ	eigenfunction
ψ	transformation kernel
σ	electrical conductivity ($\mathrm{S\,m^{-1}}$)
φ	azimuthal direction

Sub-/Super-script	
am	related to active material
batt	related to battery
case	related to battery case
cc	related to current collector
cell	related to cell (electrode pair)
ec	related to electrochemical reaction
eff	related to current collector
elec	related to electrode
f	related to filler (liquid) structural material
m	related to membrane
n	related to negative electrode
p	related to positive electrode
ref	related to the reference temperature
s	related to solid structural material
$\bar{}$	transformed quantity based on Eq. (5.13a)
$\equiv$	transformed quantity based on Eq. (4.11)

Executive Summary

Among different types of rechargeable batteries, Li-ion cells have received intense attention due to their high specific energy ($\sim$ 180 Wh kg^{-1}), high energy density ($\sim$400 Wh L^{-1}), high operating voltage (up to about 4 V), short charging time, minimal memory effects and low self-discharge rate (around 5-8%), and long life. Such desired features make Li-ion batteries one of the most favoured candidates for wide variety of applications including: military, aerospace, telecommunication, and automotive.

Safety coupled with thermal effects is one of the most important challenges facing further application of Li-ion cells. The development and implementation of Li-ion batteries, particularly in automotive applications, requires substantial diagnostic and practical modeling to fully understand the thermal characteristics for various operating conditions. In this thesis, a number of new analytical and numerical electro-thermal models are reported that can accurately predict the thermal behaviour of Li-ion batteries. In addition, a new battery test bed along with new testing protocols have been developed to measure main electro-thermal parameters of battery operation and to validate the proposed models. The proposed models are compact and computationally effective and can be implemented in real time applications. Therefore, the outcome of the present study provides a proven platform for the design and development of thermal management battery systems (BTMS) in engineering applications such as HEVs, EVs, and grid storage.

Objectives:

The following provides an overview of this thesis goals:

- To develop an in-depth understanding of the interplay between electrical and thermal behaviour of Li-ion batteries under various duty cycles and environmental conditions;

- To develop a complete range of modeling approaches from full numerical to analytical models that can be applied in battery thermal management systems design;

- To develop battery performance and characterization test protocols based on available HEVs/EVs battery test procedure manuals

Methodology: To develop a complete range of models that can describe the electro-thermal dynamics of the battery with modest computational effort, empirical approaches are adapted to decouple the electrical and thermal models of the cell from the complicated and detailed chemical model.

To gather the experimental data required for the model development and solution validation, a battery testing protocol was designed and developed in the *Laboratory for Alternative Energy Conversion* (LAEC) at Simon Fraser University. The main components of the battery test-set are: *i*) a power processing unit (ABC-150) for cycling the batteries; *ii*) an environmental chamber for simulating different environmental conditions and an accelerated rate calorimeter (ARC) for measuring the specific heat capacity; and *iii)* a software (Emerald from Greenlight Innovation) that allows emulating various duty cycles and charging/discharging profiles and data acquisition.

As summarized in the following chart, the modeling methodology presented in this thesis can be divided into two main parts: *i*) analytical solutions, and *ii*) numerical simulations.

Analytical modeling: First, a general three-dimensional analytical thermal solution is proposed to predict the temperature distribution inside Li-ion batteries considering multi-dimensional heat conduction, orthotropic thermal conductivities, and time dependent and temperature dependent heat generation terms. To demonstrate the versatility of the model, the solution is adapted to study the thermal behaviour of the prismatic and cylindrical NiMH batteries during fast charging processes. Thereafter, a new theoretical model is proposed for potential and current density distributions within the cell. By coupling the proposed electrical model with the thermal model through the heat generation term, a new Joulean heat source is introduced to the energy equation to consider the heat produced from the bulk electron movement in the electrodes. The proposed analytical solutions can accurately describe the electro-thermal response of the cell operating at galvanostatic discharge/charge.

Numerical analysis: To model the battery electro-thermal performance at more dynamic duty cycles, an equivalent circuit model is developed as a tool for simulating electrical behaviour of the cell across variety of operating conditions. Using a finite element PDE solver, COMSOL MULTIPHYSICS, an equivalent circuit-based model is introduced to investigate the local distribution of current, potential, and temperature of a Li-ion cell. Accordingly, the list of contributions from the present study is presented below;

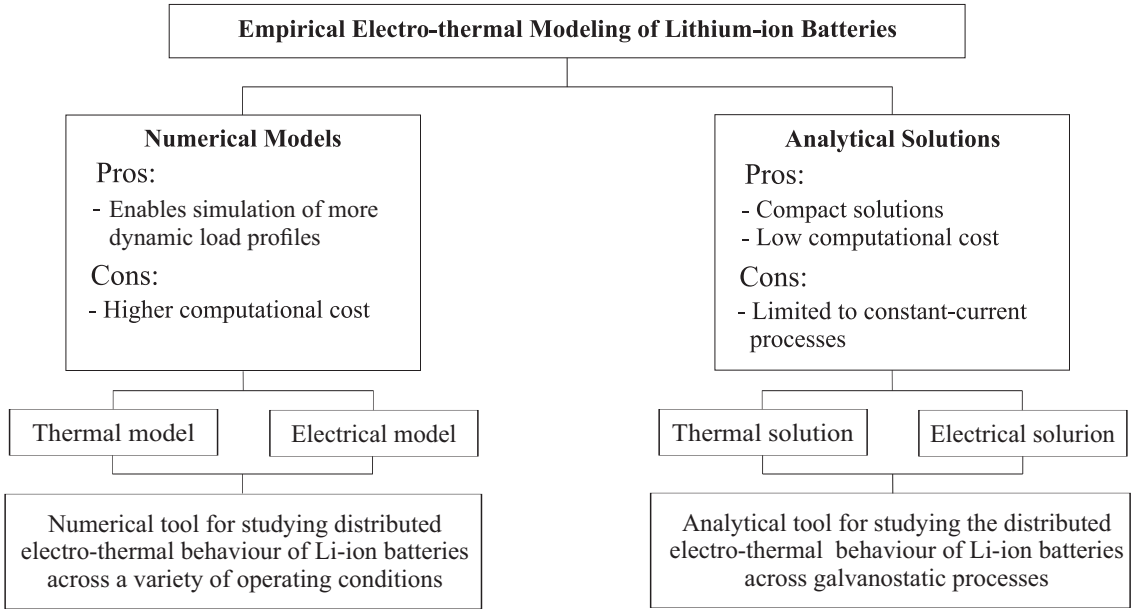

Figure 1: The present research project and deliverable.

- Designed a battery testing setup and studying the behaviour of Li-ion batteries across variety of operating conditions,
- Developed analytical solutions for thermal and electro-thermal models of pouch-type Li-ion batteries during constant current discharge processes, published in Journal of Electrochemical Society and Electrochimica Acta,
- Extended the analytical thermal model to cylindrical-shape and Ni-MH batteries to ensure the versatility of the model to be adapted in different chemistry and geometries, published in Journal of Electrochemical Society,
- Developed a new equivalent circuit model (ECM) to simulate the electrical dynamics of Li-ion batteries across a wide range of operating conditions,
- Developed a new distributed numerical model for the electro-thermal dynamics of Li-ion batteries based on the equivalent circuit model.

Chapter 1

Introduction

Climate change, diminishing reserves of fossil fuels, and energy security demand alternatives to our current course of energy usage and consumption. A broad consensus concurs that implementing energy efficiency and sustainable energy technologies are necessities now rather than luxuries to be deferred to some distant future [1]. Of particular interest for the sustainable energy technology are (1) powering electric vehicles that can compete with car powered by internal combustion (IC) engines and resolved the issue with CO_2 emission and (2) stationary storage of electrical energy from renewable energy sources [2].

Investments for the exploitation of renewable energy resources are increasing worldwide, with particular attention to wind and solar power energy plants as the most mature technologies [3]. However, a major barrier to wide ranging application of renewable energy sources is continuity of supply; generation of power by solar and wind sources, for example, can be hampered by time of day, dust, cloud and weather conditions. Thus, utilization of these intermittence resources requires high efficiency energy storage systems. Electrochemical systems, such as batteries and supercapacitors that can efficiently store and deliver energy on demand in stand-alone power plants, as well as provide power quality and load leveling of the electrical grid in integrated systems, are playing a crucial role in this area [3]. Selection of a storage system for a specific application is often made based on the amount of energy and power density that can be delivered from the system. Although specific energy and power are important, other factors must also be taken into account when selecting a system for a spinoff application, including reliability, safety, self-discharge, temperature and even humidity. A useful means of representing the operational performance of energy storage and energy conversion devices is a graph of specific energy ($A \times V \times h / kg =$

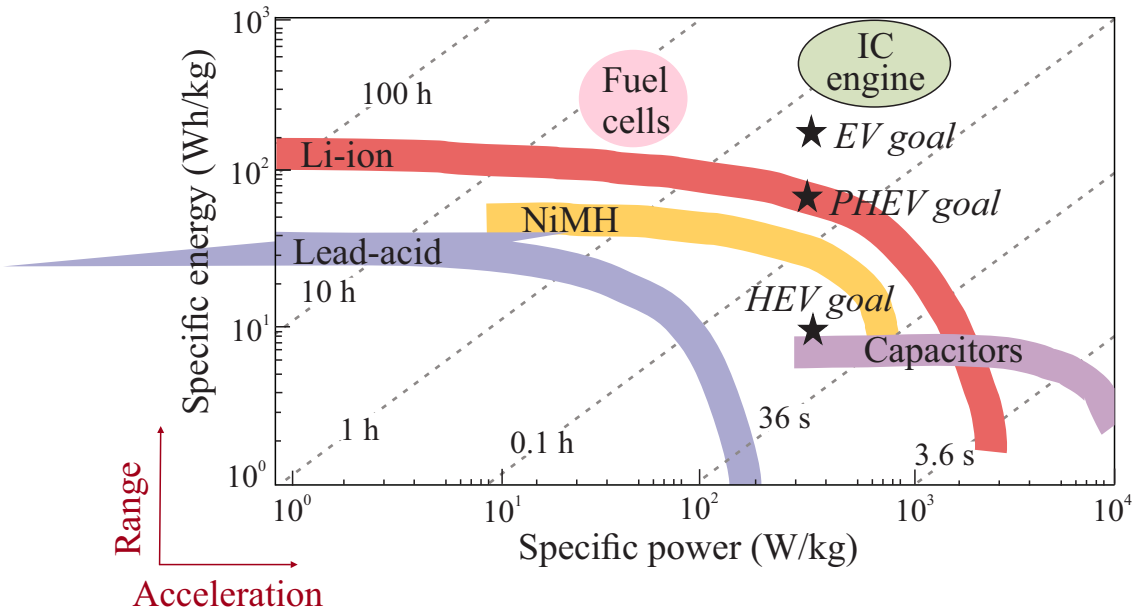

Figure 1.1: *Ragone* plots (specific power density in W/kg versus specific energy density in Wh/kg) for an array of energy storage and energy conversion devices, courtesy to [4].

W × h / kg) vs. specific power (W / kg). This graph is known as a *Ragone* plot, and in Fig. 1.1 it is shown for supercapacitors and three common rechargeable batteries namely: NiMH, lead acid, and Li-ion battery. Note that this plot shows specific energy and power on a cell level for batteries made for many different applications, from consumer electronic to vehicles. The following sections present the analysis of the above-mentioned electrochemical technologies for both the stationary and mobile applications [4].

1.1 Electrochemical energy storage

1.1.1 Rechargeable batteries

Batteries are devices that convert the chemical energy contained in an electrochemically active material directly into electrical energy by means of a redox reaction. For a rechargeable system, the battery allows the storage of a defined amount of chemical energy and can be re-charged when the electrochemically active material has been transformed. Several types of rechargeable systems exist, from the mature lead acid to different newer technologies at various developmental stages [5].

Lead acid batteries

The lead acid battery was the first known type of rechargeable battery. It was suggested by French physicist Gaston Plante in 1860 for means of energy storage. Lead acid batteries continue to hold a leading position, especially in wheeled mobility and stationary applications [6]. The lead acid battery is combination of a lead, lead dioxide and an electrolyte composed of sulfuric acid and water.

Lead acid batteries are offered in two different types: *i*) the flooded type which is the cheapest and tends to be used in automotive and industrial applications, *ii*) the sealed type, also called valve regulated lead-acid (VRLA), which has been rapidly used in a wide range of applications including power supplies and standalone power supplies for remote areas. Both the power and energy capacities of lead acid batteries depend on the size and geometry of the electrodes which makes it unfavourable for automotive industry. The power capacity can be improved by increasing the surface area of each electrode, which means greater quantities of thinner electrode plates in the battery.

Low cost, high power, and easy recyclability are among the advantages of the lead acid batteries. One main drawback of lead acid batteries is usable capacity decreases when high power is discharged. In addition, as shown in Fig. 1.1, lead acid batteries have four times less specific energy than that offered by Li-ion batteries, and it is expected to be gradually displaced by Li-ion and NiMH, due to environmental impact concerns.

NiMH batteries

Since 1990, when first NiMH batteries commercialized in Japan, they have been adapted to a wide range of applications from hand-held electronics to HEVs. The NiMH battery consists of a positive nickel hydroxide and negative metal hydride, and nylon separator sheets. The electrodes that accommodate active materials required in the battery chemistry and the separator sheets have porous structures, and their pores are filled with a concentrated KOH solution as the electrolyte. Recently, Li-ion batteries are realized as the new competitor for NiMH cells, thanks to their outstanding energy density, minimal memory effect and low self discharge rate. Nonetheless, NiMH cells are expected to sustain their position in the market due to their environmental friendliness, relatively low price, and better thermal stability.

Nickel-metal-hydride is not without drawbacks. Figure 1.1 shows that the NiMH battery has twice less specific energy compared to Li-ion batteries that limits their application in electric power-train. NiMH also has high self-discharge and loses about 20% of its capacity within the first 24 hours, and 10% per month thereafter. Modifying the hydride materials lowers the self-discharge and reduces corrosion of the alloy, but this decreases the specific energy [7]. Moreover, NiMH batteries generate heat during fast-charge and high-load discharge which can play a crucial role in their safety, performance, and longevity.

Li-ion batteries

Pioneer work with the lithium battery began in 1912 under G.N. Lewis, but it was not until the early 1970s that the first non-rechargeable lithium batteries became commercially available. Attempts to develop rechargeable lithium batteries followed in the 1980s but the endeavour failed because of instabilities in the metallic lithium used as anode material [7]. Historically, first Li batteries developed for portable electronics (cellular phones, cordless, notebooks). Lithium is the lightest of all metals, has the greatest electrochemical potential and provides the largest specific energy per weight. Thus, Li-ion batteries have characteristics of high energy and power density and have been shown to be less affected by memory effect, compared to other types of batteries, see Fig. 1.1. These traits make the Li-ion battery the most likely candidate to assist sustainable mobility such as EVs, HEVs, scooters, motorcycles, electrical bicycles [8–10]. Longevity, low self-discharge (less than half that of NiMH), and rapid charging and high load capabilities are among the advantages offered by Li-ion batteries.

Supercapacitors

Supercapacitors are electrochemical devices that store energy by virtue of the separation of charge, unlike batteries, which store energy through chemical transformation of electrode materials. Super capacitors continue to develop and mature as an energy storage technology, though somewhat still in the shadow of rechargeable batteries.

During the storage of electrochemical energy in a battery, chemical inter-conversions of the electrode materials occur usually with concomitant phase changes. Although the overall energy changes can be conducted in a relatively reversible thermodynamic route, the charge and discharge processes in a storage battery often involve irreversibility in inter-conversions of the chemical

electrode-reagents. Accordingly, the cycle-life of storage batteries is usually limited, and varies with the battery type. By contrast, with energy storage by a capacitor, only an excess and a deficiency of electron charges on the capacitor plates have to be established on charge and the reverse on discharge, and no chemical changes are involved. Accordingly, a capacitor has an almost unlimited recyclability, typically between 10^5 and 10^6 times [6].

As shown in Fig. 1.1, electrochemical capacitors have superb specific power compared to batteries, but modest specific energies. This translates, in transportation terms, as good acceleration but poor range, which is precisely opposite to batteries. From practical and technological viewpoints, electrochemical capacitors are robust devices with excellent cycle life that can improve the effectiveness of battery based systems by shrinking the volume of batteries required and reducing the frequency of their replacement.

1.1.2 Advanced rechargeable battery technology

In addition to the above-mentioned energy storage systems that have been commercialized, a large number of battery technologies are still under development that can be categorized as: 1) rechargeable metal-air batteries and 2) flow batteries [6]. By virtue of removing much of the mass of the positive electrodes, metal-air batteries offer the best prospects for achieving specific energy that can be comparable with petroleum fuels. Lithium-air (oxygen) and sodium-air (oxygen) are two main categories of such advanced technology. Since this subject is not in the scope of this study, the readers are referred to Ref. [6, 11–13] for more information in this regard.

A flow battery is a rechargeable battery where the energy is stored in one or more electro-active species dissolved into liquid electrolytes. Flow batteries can be fitted to a wide range of stationary energy storage systems and they are not recommended for vehicular applications. Flow batteries are classified into redox flow and hybrid flow batteries where more detailed discussion can be found in Refs. [6, 14].

Overall, the high energy density, lightweight, no memory effect and low self-discharge rate make Li-ion based batteries superior to other energy storage devices for vehicular applications including HEVs, EVs, and plug-in-hybrid-electric vehicles (PHEVs), which is also the main focus of this study.

1.2 Challenges in electric and hybrid-electric vehicles

The strategy for electrifying vehicles with high capacity batteries in order to reduce or remove the contribution of internal combustion engine into powertrain has attracted an intense attention. Li-ion batteries have become the dominant battery technology for automotive industry due to several compelling features such as high power and energy density, high voltage, long cycle life, excellent storage capabilities, and memory-free recharge characteristics [30]. While Li-ion batteries are growing fast in popularity, safety issues and cost (related to cycle and calendar life) that all are coupled to thermal effects in batteries, are the main barriers to the development of large fleets of vehicles on public roads equipped with Li-ion cells [15]. It is evident that under high discharge conditions, which involve high rates of Joulean heat generation and exothermic electrochemical reactions, batteries are prone to excessive temperature rise. The temperature profile presented in Fig. 1.2 is an evidence of temperature rise in the battery at different discharge rate of 1 C, 2 C, and 3 C, which correspond to 20 A, 40 A, and 60 A discharge currents.

Figure 1.2 illustrates that over a short 30 minute time period (short from a vehicle operation viewpoint) for 2C and a 20 minute time period for 3C discharge, enough heat is generated to increase the cell temperature to 50 °C (for 2C) and 55 °C (for 3C) from a 24 °C start condition. This value is only for a single prismatic cell with free convection boundary condition, so even a greater temperature can result when extrapolated to the approximately 100 prismatic cells in a battery pack of PHEVs, HEVs, and EVs, where there is no free boundary convection, but only conduction between pouch cells,; this problem is explained next. This temperature evolution can initiate swelling [16], thermal runaway [17], electrolyte fire, and in extreme cases explosion [18]. Moreover, exposure of Li-ion batteries to sub-freezing temperatures drastically reduces their energy and power [19]. Therefore, for optimum performance and longevity, the Li-ion battery should operate within 25-40 °C, also it is desirable to maintain the temperature variation between battery modules in the battery pack less than 5 °C [20].

Hence, the development and implementation of Li-ion batteries, particularly in automotive applications, requires substantial diagnostic and practical modeling efforts to fully understand the thermal characteristics in the batteries across various operating conditions [21–23]. Indeed, thermal modeling prompts the understanding of the battery thermal behavior beyond what is possible from experiment, and it provides a basis for exploring thermal management strategies for batteries in HEVs and EVs [24]. Once a battery is characterized to the extent that calculations can be used to

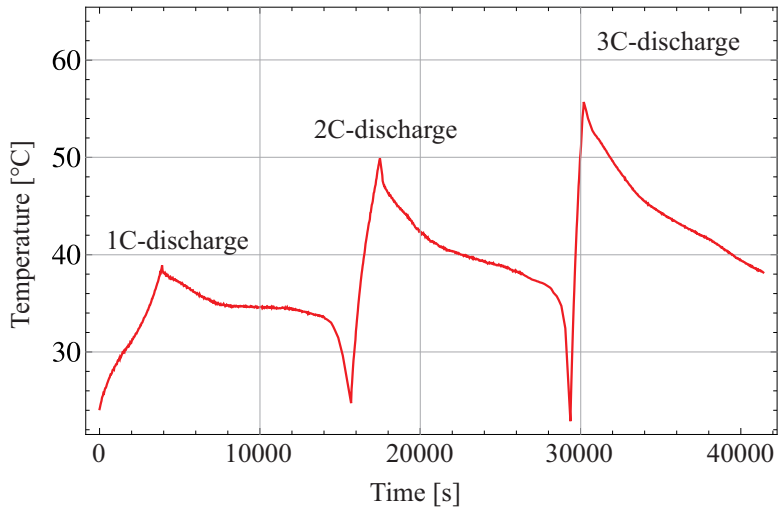

Figure 1.2: Temperature rise at the surface of a prismatic Li-ion cell during 1 C, 2 C, and 3 C discharge rates, each followed by 1 C charge process.

provide a good estimation of electro-chemical-thermal behaviour, it is possible to complete the design of the battery system on the vehicle, and to size the heat exchangers and related thermal-system components necessary to heat or cool the battery [25].

1.3 Research motivation

This work has been impelled by a collaborative research project with a local company, Future Vehicle Technologies (FVT), that aims to introduce a high performance electric sports car called *eVaro* as shown in Fig. 1.3. The company requires an intelligent system to control and keep the temperature of their 21 kWh battery pack within the desirable range.

As shown in Fig. 1.2, during operation with high discharge rates, Li-ion batteries can heat up to 55 °C or greater, particularly when cells are stacked into modules and then packs, and when they are in a warm ambient temperature. Hence an efficient battery thermal management system (BTMS) is required to maintain the battery temperature within the desirable range and ensure optimal vehicle operation in terms of safety, performance, and battery longevity.

As an effective tool, mathematical simulations of the battery can help to obtain a fundamental understanding about how the heat is generated inside the battery, how it can be conducted out of the battery during different operating conditions, and how the proper temperature control of a battery can be achieved. To fulfill this aim, a series of modeling studies are developed to estimate the amount of heat generation at the cell level, and predict the transient distribution of electrical and

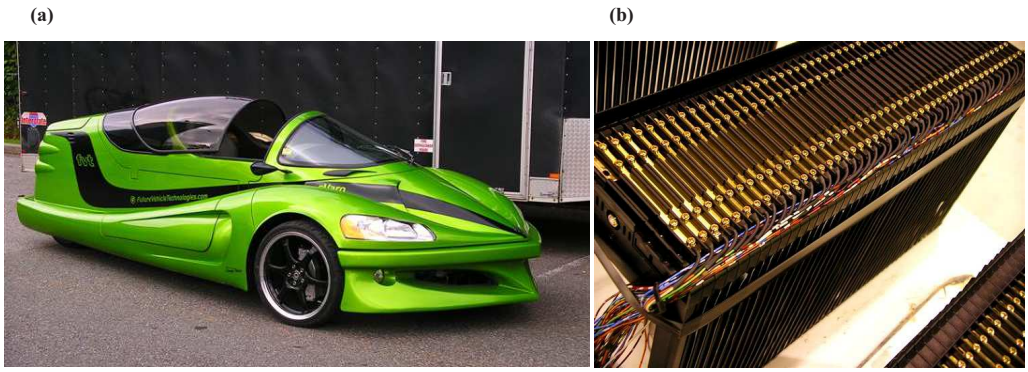

Figure 1.3: a) *Evaro*, the high performance electric sports car introduced by Future Vehicle Technologies, b) battery pack used in *evaro*.

thermal behaviour of the battery at different operating conditions with minimum computational effort. Using this information, one can expand the model to a module/pack level in order to design a proper BTMS.

Accordingly, the aim of this work is to propose computationally effective multi-physics models capable of predicting the distributed electro-thermal behaviour of the battery across different load and environmental conditions. These models should be computationally effective and be easily extended to module/pack levels to predict their thermal behaviour for the design of an efficient BTMS.

1.4 Research objectives

Given that the problems of safety, performance, and longevity of batteries are all linked to the thermal performance of the battery, reliable battery thermal models are needed to predict the heat generation and transport inside batteries as a tool for designing efficient thermal management systems depending upon the cell design and operation conditions. The developed mathematical model should be computationally affordable to be applied for scale-up batteries (module/pack) that is the ultimate model for BTMS design. Accordingly, the present work aims to propose a series of empirical multi-physics models to characterize and simulate the thermal response of the battery at actual operating conditions. Accordingly, the objectives of this research can be summarized as:

- To develop battery performance and characterization test protocols to collect the data required for developing the empirical multi-physics models.

- To develop an in-depth understanding of the interplay between electrical and thermal behaviour of Li-ion batteries under various loads and environmental conditions.
- To develop a complete range of computationally effective modeling approach from full numerical to analytical models that can be applied in BTMS design.

To provide the experimental data required for the modeling and to validat the proposed models, a battery testing protocol was designed and developed in the Laboratory for Alternative Energy Conversion (LAEC) at Simon Fraser University. The main components of the battery test-set are: a power processing unit (ABC-150) for cycling the batteries, an environmental chamber for simulating different environmental conditions and an accelerated rate calorimeter (ARC) for measuring the specific heat capacity and heat generation rate of the battery.

1.5 Thesis structure

The thesis is organized as follow. Chapter 1: introduces the research importance along with the motivation and objectives.

Chapter 2: reviews related research in Li-ion batteries.

Chapter 5: presents the work performed to design battery performance and characterizing test protocols.

Chapter 3: presents a three-dimensional analytical model to study the thermal behaviour of prismatic-shaped batteries.

Chapter 4: presents a computationally-effective thermal model for spirally wound batteries.

Chapter 6: presents a distributed analytical electro-thermal model.

Chapter 7: presents a distributed numerical electro-thermal model.

Chapter 8: presents conclusions, summary of contributions, and future works.

Chapter 2

Introduction to Li-Ion Batteries and Literature Review

According to a recent market report published by Transparency Market Research [26], the global market for Li-ion battery was worth USD 11.70 billion in 2012 and is expected to reach USD 33.11 billion in 2019, growing at a 14.4 % compound annual growth rate (CAGR). As presented in Fig. 2.1, the consumer segment, which accounted for 60.3 % of total Li-ion battery revenues in 2013, is expected to see its market share reduced to 23.9 % in 2020. This predicted reduction in total market share reflects the expected significant growth in Li-ion battery demand in the automotive and grid and renewable energy storage segments. In Fig. 2.1, the global market demand for Li-ion batteries in 2013 is compared with the one predicted in 2020. Despite revenue growth, market share in the

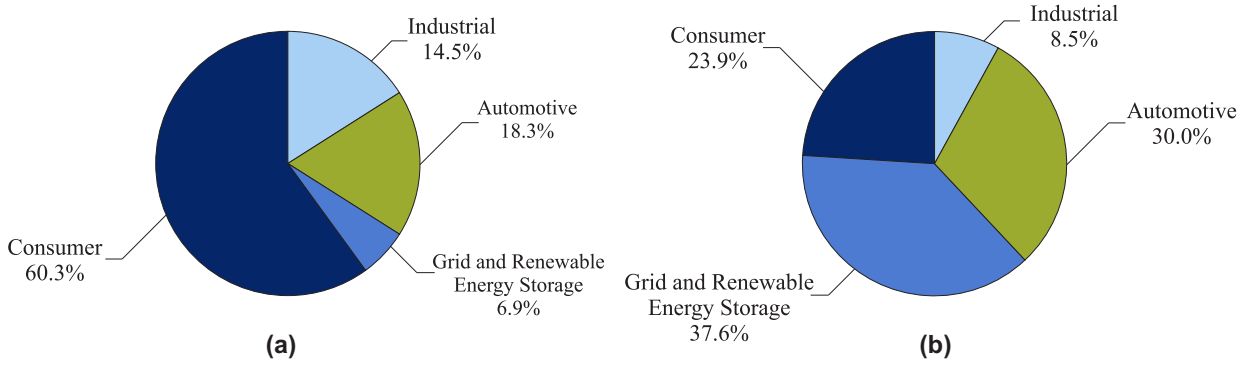

Figure 2.1: Market segment of Li-ion batteries in consumer device vendors, industrial goods manufactures, grid and renewable energy storage segments and automobile manufacturers in a) 2013 and b) predicted 2020, courtesy to [27].

industrial segment is expected to decline because of the explosive growth in the automotive segment and grid and renewable energy storage segment.

2.1 Li-ion cell operation

In Fig. 2.2, the internal structure of the battery from cell scale to electrode scale is illustrated. Figure 2.2a and b depict the unfolded and folded layered structure in the battery. This layered configuration is also referred as "sandwiched configuration" [28]. In Fig. 2.2c, a schematic presentation on charge transfer between electrode pairs during charge and discharge cycle is given, this is also the fundamental scale for thermo-electro-chemical battery simulations, since the collective behaviour of these unit cells represents the overall battery behaviour.

Li-ion battery uses a cathode (positive electrode), an anode (negative electrode) and electrolyte as conductor. The cathode is made of a composite material and defines the name of the Li-ion battery cell. The electrolyte can be liquid, polymer or solid. In case of a polymer or solid electrolyte, the electrolyte will act as a separator as well. The separator is porous to enable the transport of lithium ions. It prevents the cell from short-circuiting and protects the cell from thermal runaway. In advanced Li-ion cells, anode (negative electrode) is typically made of carbon-Li intercalation compound, and for this, usually is referred as graphite electrode, while the cathode includes metal-oxide materials. Indeed, what the cathode is made from determines the cell's capacity as it will be discussed in next chapter. The critical feature is the rate at which the cathode can intercalate and deintercalate free lithium ions.

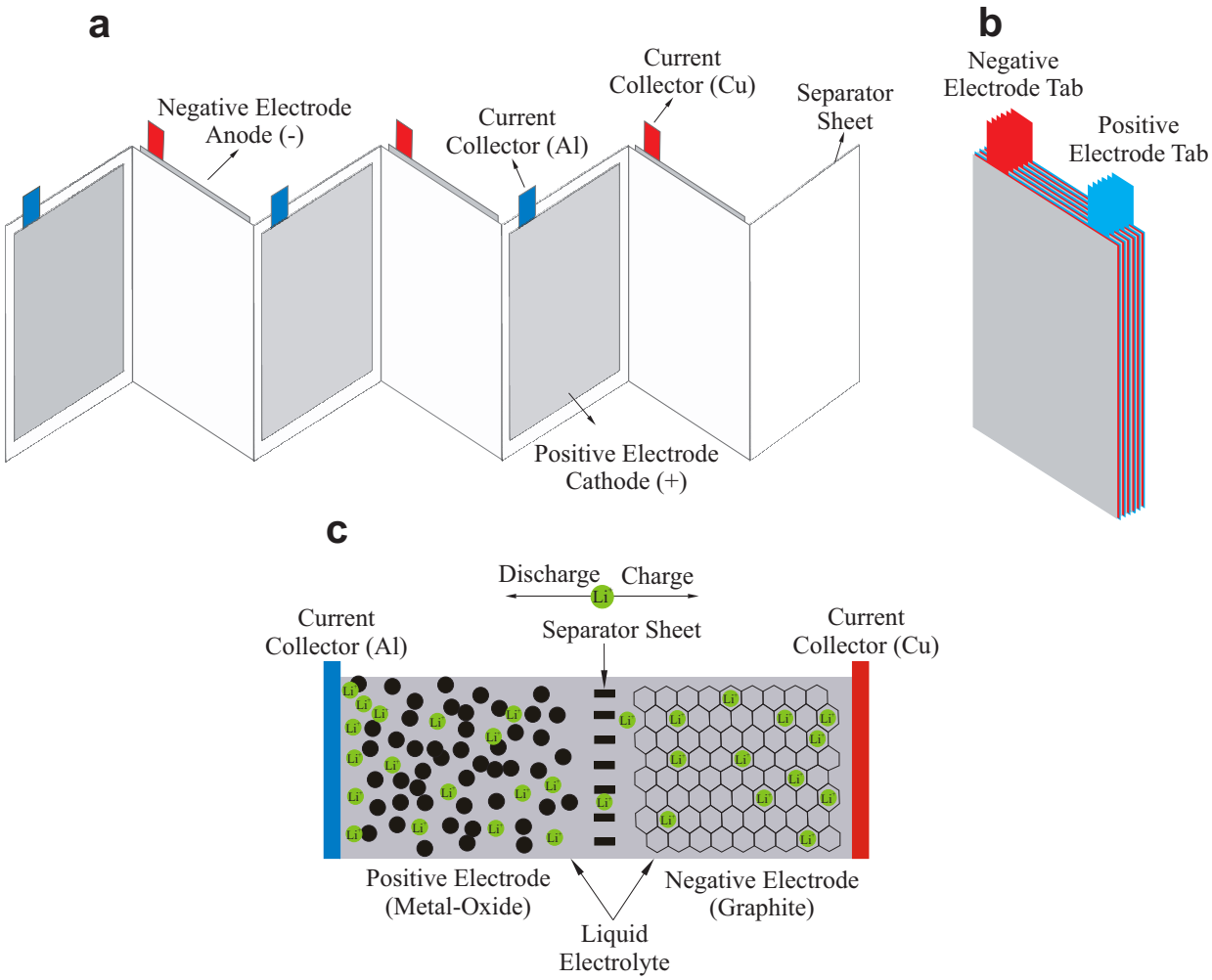

Figure 2.2: (a) Schematic of the layered structure of lithium-ion battery cells. Repeated layers of negative electrodes, separator sheets, and positive electrodes construct the battery core, (b) Folded battery core diagram. This configuration is also referred as a sandwiched layout, (c) Components of the unit cell, and charge transfer during charge and discharge cycles are illustrated.

The overall chemical reactions inside the Li-ion battery in general form is as;

$$6\mathrm{C} + \mathrm{Li\ M}_y\ \mathrm{O}_z \rightleftharpoons \mathrm{Li}_x\ \mathrm{C}_6 + \mathrm{Li}_{1-x}\ \mathrm{M}_y\ \mathrm{O}_z \tag{2.1}$$

where $x \leq 1$, M is the metal in the positive electrode (nickel, cobalt, manganese, or their combination), and O is oxygen. For the charge and discharge processes, the reactions proceed from left to right, and right to left, respectively. Charge and discharge reactions in the electrodes are

$$6\mathrm{C} + x\mathrm{Li}^+ + x\mathrm{e}^- \rightleftharpoons \mathrm{Li}_x\ \mathrm{C}_6 \quad (\text{negative electrode}), \tag{2.2a}$$

$$\mathrm{LiM}_y\mathrm{O}_z \rightleftharpoons \mathrm{Li}_{1-x}\ \mathrm{M}_y\mathrm{O}_z + x\mathrm{Li}^+ + x\mathrm{e}^- \quad (\text{positive electrode}). \tag{2.2b}$$

The charge and discharge reactions for rechargeable Li-ion battery are endothermic and exothermic, respectively. If the battery reaction is ideally reversible, the thermodynamic equation under a constant temperature and constant pressure yields the following relation [29]:

$$\Delta G = \Delta H - T\Delta S \tag{2.3}$$

where the residual energy at energy conversion between the enthalpy change ΔH of the battery reaction and the electrical work ($\Delta G = -nFV_{\mathrm{oc}}$) can be compensated by the heat energy of $T\Delta S$. The heat, Q_{s}, by entropy change, ΔS, is described by the following equation:

$$Q_{\mathrm{s}} = T\Delta S\frac{I}{nF} \tag{2.4a}$$

$$-\frac{\partial \Delta G}{\partial T} = nF\frac{\partial V_{\mathrm{oc}}}{\partial T} \tag{2.4b}$$

where T is battery temperature, I is charge/discharge current (defined as positive during charge cycle), F is Faraday constant, V_{oc} is cell voltage for open-circuit, and n is the charge number participating to the reaction ($n = 1$ for Li-ion battery). The reaction directions for charge and discharge cycles are opposite to each other, thus Q_{s} is endothermic during charge cycle and exothermic during discharge process.

When electric current flows through the cell, the cell voltage, V, deviates from V_{oc} due to over-potential or electrochemical polarization. The total over-potential can be deconvoluted into several parts: the charge transfer or activation over-potential, the ohmic over-potential, and the concentration over-potential. The energy loss by this polarization dissipates as irreversible heat that is

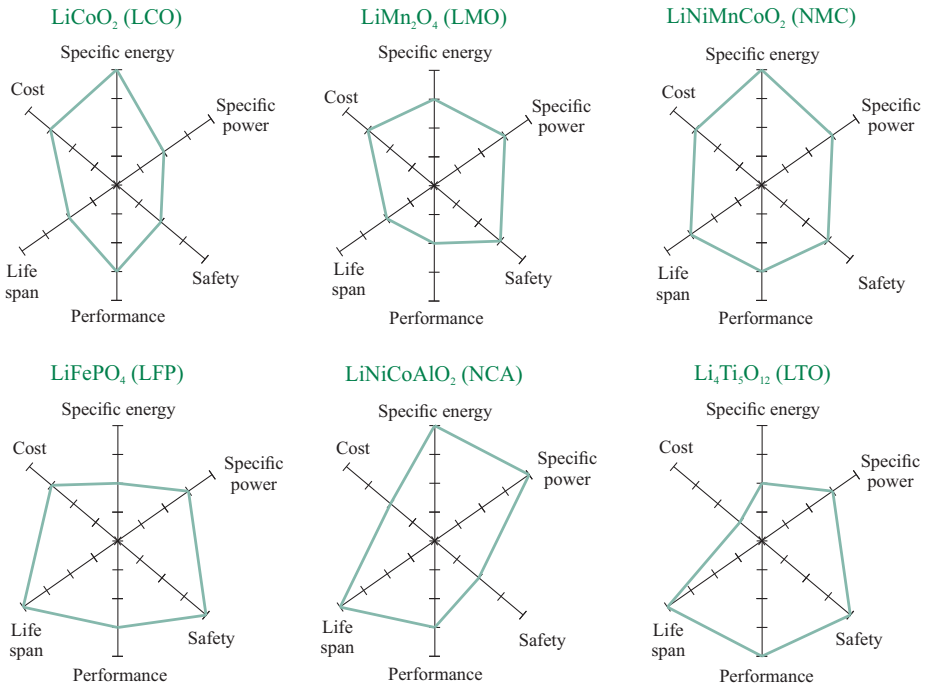

Figure 2.3: Comparison of suitable Li-ions for EV in terms of specific energy or capacity; specific power or the ability to deliver high current; safety or the chances of venting with flame if abused; performance at hot and cold temperatures; life span reflecting cycle life and longevity; and cost.

exothermic during both charge and discharge cycles. In the following chapters, more discussion will be provided in this regard.

The term ”Li-ion” includes a number of different chemistries; Fig 2.3 shows the chemistries under development in automobile industry. Each chemistry offers a different mix of cost, durability, performance, and safety as discussed in the following.

Lithium cobalt oxide (LCO), $LiCoO_2$, due to its high specific energy is the most common type of Li-ion batteries in small consumer electronics. The battery consists of a cobalt oxide cathode and a graphite carbon anode. As it is shown in Fig 2.3, the drawback of LCO is relatively short life span, low thermal stability and limited load capabilities (specific power).

The three-dimensional spinel structure of the cathode in lithium manganese oxide (LMO), $LiMn_2O_4$, provides low internal resistance, high thermal stability and enhanced safety. Nonetheless, it has limited cycle and calendar life. From Fig 2.3, one can conclude that using LMO in the

cathode can roughly offer a capacity that is one-third lower than LCO based cathode, but the battery still holds 50% more energy than nickel-based chemistry.

Lithium nickel manganese cobalt oxide (NMC), $LiNiMnCoO_2$, is the most modern manganese-based Li-ion batteries with the cathode combination of nickel, manganese, and cobalt offers a unique blend that improve the specific energy, prolong the life span, and lowers raw material cost due to reduced cobalt content. Figure 2.3 shows that NMC has satisfactory overall performance and excels on specific energy which makes it the preferred candidate for the electric bikes and other electric power-trains [7].

Lithium iron phosphate (LFP), $LiFePO_4$, as the cathode material for rechargeable lithium batteries offers acceptable electrochemical performance with low internal resistance. Li-phosphate battery is more tolerant to full charge conditions and is less stressed than other lithium-ion systems if kept at high voltage for a pronged time. It also has excellent safety and long life span but offers moderate specific energy, lower operating voltage, and higher self-discharge rate compared to other Li-ion based batteries.

Lithium nickel cobalt aluminum oxide (NCA), $LiNiCoAlO_2$, is another type of Li-ion based battery that shares similarity with NMC in terms of high specific energy and reasonable specific power and a long life span which makes it a candidate for electric vehicles applications. However, high cost and marginal safety remain problematic, see Fig. 2.3.

Lithium titanate (LTO), $Li_4Ti_5O_12$ that replaces the graphite in the above-mentioned Li-ion batteries, is considered as a promising anode material for applications that require high rate capability and long cycle life. Due to low nominal cell voltage, they can be fast-charged and deliver a high discharge current. LTO-based batteries provide much better low temperature performance compared to graphite-based batteries which makes them excellent in safety. Nonetheless, as it is illustrated in Fig 2.3, low energy density and high cost are the main drawbacks of LTO that needs to be improved.

As a summarized in Table 2.1, these battery technologies are ranked in terms of key parameters (safety, power and energy density, and life) that are required in vehicular applications.

Table 2.1: Key parameters of different Li-ion chemistries.

Parameter	Highest performing chemistry	Lowest performing chemistry
Safety	$Li_4Ti_5O_{12}$, $LiFePO_4$	$LiCoO_2$
Power	$LiFePO_4$	$LiCoO_2$
Energy	$LiCoO_2$, $LiNiCoO_2$, $LiNiCoAlO_2$	$LiFePO_4$
Life	$LiFePO_4$, $LiNiCoAlO_2$	$Li_4Ti_5O_{12}$

In general, the batteries can either be of high power density type or high energy density type. Power density provides a good measure on how much energy can be released due to discharge at a given time with regards to kg or litres. A high energy density battery is useful in applications where a longer driving distance is required e.g. in EVs and PHEVs which is intended to be driven on pure electricity for long distances. A high power density battery is useful in an application where a short but intensive power pulse is required; e.g. in an ordinary HEVs as the electric motor often only assists the combustion engine in short periods [30].

2.2 Battery glossary

Cell, module and packs: EVs and HEVs have a high voltage battery pack that consists of individual modules and cells organized in series and parallel. A cell is the smallest, packaged form a battery can take and is generally one to six volts. A module consists of several cells connected in either series or parallel. A battery pack is then assembled by connecting modules together, again either in series or parallel.

C-rates: The charge and discharge current of a battery is measured in C-rate. Most portable batteries are rated at 1 C. This means that a 20 A h battery would provide 20 A for 1 hour if discharged at 1 C rate. The same battery discharged at 0.5 C (1/2 C) would provide 10 A ($20 \times 0.5 = 10$) for 2 hours. 1 C is often referred to as a 1 hour discharge; a 0.5 C would be 2 hour and 0.1 C a 10 hour discharge.

State of charge (SOC): The state of charge refers to the amount of charge in a battery relative to its predefined full and empty states i.e. the amount of charge in Amp-hours left in the battery. Manufacturers typically provide voltages that represent when the battery is empty (0 % SOC) and full (100 % SOC). SOC is generally calculated using current integration to determine the change in battery capacity over time.

Depth of discharge (DOD): It is a measure of how much energy has been withdrawn from a battery and is expressed as a percentage of full capacity. For example, a 100 Ah battery from which 40 Ah has been withdrawn has undergone a 40 % depth of discharge (DOD). Depth of discharge is the inverse of state of charge (SOC). A battery at 60% SOC is also at 40 % DOD.

Open circuit voltage (OCV): The open circuit voltage (OCV) is the voltage when no current is flowing in or out of the battery, and, hence no reactions occur inside the battery. OCV is a function of state-of-charge and is expected to remain the same during the life-time of the battery. However,

other battery characteristics change with time, e.g. capacity is gradually decreasing as a function of the number of charge-discharge cycles.

Terminal voltage (V): The voltage between the battery terminals with load applied. Terminal voltage varies with SOC and discharge/charge current.

Nominal voltage (V): The reported or reference voltage of the battery, also sometimes thought of as the normal voltage of the battery.

Cut-off voltage (V): The minimum allowable voltage. It is this voltage that generally defines the empty state of the battery.

Charge voltage (V): The voltage that the battery is charged to when charged to full capacity. Charging schemes generally consist of a constant current charging until the battery voltage reaching the charge voltage, then constant voltage charging, allowing the charge current to taper until it is very small.

Capacity or nominal capacity (Ah for a specific C-rate): The coulometric capacity, the total Amp-hours available when battery is discharged at a certain discharge current (specified as a C-rate) from 100 % SOC to the cut-off voltage. Capacity is calculated by multiplying the discharge current (in Amps) by the discharge time (in hours) and decreases with increasing C-rate.

Specific energy ($\mathrm{Wh\,kg^{-1}}$): The specific energy of a battery is expressed as a nominal energy per unit mass, such as Wh / kg. It is highly dependent on the battery chemistry and packaging.

Energy density ($\mathrm{Wh\,L^{-1}}$): The energy density of a battery is expressed as a nominal energy per unit volume, such as Wh / L. It is highly dependent on the battery chemistry and packaging.

Power density ($\mathrm{W\,L^{-1}}$): The power density of a battery is expressed as a nominal power per unit volume, such as W / L or kW / L. It is highly dependent on the battery chemistry and packaging.

Internal resistance: The internal resistance is sometimes considered as the ohmic resistance of the cell, which is the direct voltage change after application of a current step on a cell in equilibrium. Another definition for the internal resistance is the sum of the ohmic, activation and diffusion polarization resistances, which is the largest possible voltage drop in the cell. Nevertheless, the result in power dissipation in the form of heat will result due to the complete voltage drop. The voltage drop can be mainly divided as:

- IR drop is due to the current flowing across the internal resistance of the battery, by ohmic resistance.

- Activation polarization refers to the various retarding factors inherent to the kinetics of an electrochemical reaction, like the work function that ions must overcome at the junction between the electrodes and the electrolyte.

- Concentration polarization takes into account the resistance faced by the mass transfer (e.g. diffusion) process by which ions are transported across the electrolyte from one electrode to another.

The internal resistance of a battery is dependent on temperature, C-rate and SOC. Different values for the internal resistance can be found depending on the measurement method. This is caused by the time constants associated with the activation and diffusion polarization resistances; whether the battery electrodes are in equilibrium or not is also important in determining the value of the internal resistance [7].

2.3 Literature review

Since Li-ion battery performance is strongly linked to temperature, it is vital to understand how heat is generated and dissipated inside a battery. Heat generation inside batteries is a complex process that requires understanding of how the electro-chemical reaction rates change with time and temperature and how current is distributed within larger batteries [15]. A variety of processes coexist during both charge and discharge cycles of Li-ion batteries. These processes, based on their corresponding transport fields, are conventionally divided into chemical, electrical, and thermal categories [31]. Accordingly, an ideal mathematical model for Li-ion batteries must be a thermo-electro-chemical model, which simultaneously describes transient transport fields for mass, charge, and energy in a three-dimensional domain of a porous medium, i.e., electrodes and separator sheets [32].

The electro-chemical processes happen in the macroscopic level and can locally be divided in two distinct parts: *i*) the processes in the electrolyte (solution phase), and *ii*) the processes in the electrodes (solid phase). These processes are strongly coupled; the former involves the transport (migration, diffusion, and convection) of mass and charge between the electrodes through an electrolyte solution accompanied by interfacial reactions at the surface of electrodes, while the latter deals with transport (mostly via conduction) of charges within the solid phase of the electrode assembly, i.e. current collectors and active material particles. The most well-known electro-chemical

model for Li-ion batteries is the porous-electrode model, proposed by Newman and co-workers [33–35]. To approximate the amount of heat generated during the aforementioned process, a physics-based e. g., electro-chemical-thermal model at the electrode level, see Fig. 2.2d, is needed. The multi-physics models require a large amount of computational power to solve time-varying-spatial partial differential equations. Such detailed models are quite useful for the cell design and optimization, however, they are typically of very high-order and complexity and are not suitable for real-time applications. In other words, they are too complex to be applied in studying the characterization of the electro-thermal performance of battery modules/packs, or to the design of cooling systems and control algorithms. Also, for the case of Li-ion cells, due to the simple treatment of active material in the porous-electrode model, numerous transport properties are needed to fit the experimental data. More recently, reduced-order electro-chemical models for Li-ion cells are introduced [36–39]. The order reduction decreases the computational time and allows the model implementation into a real-time on-board electronic control unit, which is of particular interest in vehicle applications to estimate Li-ion concentrations and associated state-of-charge (SOC) values. Nonetheless, the simplified models neglect some dynamics and consequently they cannot accurately predict the current-voltage behavior across different operating conditions.

To avoid complex systems of equations, reduced models are used to investigate the behaviour of Li-ion batteries. "Electro-thermal" [40, 41] and stand alone "thermal" models [42–44] are among the reduced models. Reduced models, in which some physical processes are neglected, are empirical based model that require experimental data. In case of an existing battery, for which the experimental data is obtainable, empirical models which mimic the electro-chemical performance of the battery can be generated. Indeed, simplicity and robustness of such models enables them to be applied in real-time embedded systems. Empirical models are relatively fast and simple, thus are favored in design of BTMS and control algorithms for BMS.

Thermal models

The thermal process inside the battery is described by a general energy balance detailed in Ref. [8]. Since chemical processes in the battery can be exothermic or endothermic, and charge transfer in the battery materials leads to ohmic heating, the heat generation term [45] in the energy balance equation is tightly linked to the electro-chemical process. The collective behavior of electro-chemical processes, deduced from measurements, can be included as the heat source in a standalone thermal model. Based on this decoupling strategy, there are several battery thermal models available

in the literature, see Table 2.2, including one-dimensional [46], two-dimensional [8, 47] and three-dimensional models [9, 43, 44, 48] in which a variety of cell designs modes of operation, and thermodynamic properties are considered. For an extensive bibliography on battery thermal models see Ref. [15].

To the author's best knowledge, all the multi-dimensional thermal models developed for such batteries rely on numerical solutions; thus, lack of a theoretical method is evident. The only available analytical solution is the work of Newman and Tiedemann [49], where the classical technique of separation of variables is employed to solve the transient heat conduction problem for batteries with constant heat generation and constant-temperature boundary conditions.

Electro-thermal models

Electro-thermal models can incorporate the ohmic heating due to electrical current in the electrodes of the battery. Also, the electro-thermal models can be applied to describe the distributed electrical response of the battery with modest computational effort as opposed to the detailed electrochemical model with high fidelity. These empirical electro-thermal models are based on two main methodologies: *i*) equivalent circuit models [25, 50] and *ii*) fitting function models.

Table 2.2: Summary of electro-thermal simulations using empirical approaches to predict the rate of heat generation.

lescription	Battery geometry	Type of the battery	Current range	Temperature range	Refs
l models					
sional	-	Lithium-ion	0.1-2 C	80 to 120 °C	[46]
sional	Prismatic	Lithium-ion	0.3 to 8 C	25 °C	[8]
sional	Prismatic	Lithium-ion	0.3 to 0.8 C	100 °C	[47]
sional	Prismatic	Lithium-ion	6.1 C	100 °C	[44]
sional	Prismatic	Lithium-ion	0.3 to 1.8 C	25 °C	[43]
sional	Prismatic	Nickel/iron	1 to 3 C	25 °C	[9]
thermal models based on ECM					
sional	-	NiMH	-	25 °C	[25]
sional	Cylindrical	Lithium-ion	-	5 to 45 °C	[51]
sional	Cylindrical	Lithium-ion	1 to 2.5 C	10 to 40 °C	[52]
sional	Pouch	Lithium-ion	-	5 to 40 °C	[53]
sional	Pouch	Lithium-ion	-	-	[54]
sional	Pouch	Lithium-ion	-	-10 to 40 °C	[55]
thermal models based on fitting function model					
sional	Pouch	Lithium-ion	1 to 5 C	25 °C	[41]
sional	Pouch	Lithium-ion	0.5 to 5 C	25 °C	[56]
sional	Pouch	Lithium-ion	1 to 5 C	25 °C	[57]
sional	Pouch	Lithium-ion	0.5 to 5 C	-10 to 0 °C	[58]
sional	Pouch	Lithium-ion	0.5 to 1.5 C	25 to 35 °C	[59]

i)ECM-based studies

The equivalent circuit models that are a simplification of electro-chemical models, utilized the electrical circuit elements, such as voltage sources, resistors, and capacitors, to represent the $I-V$ characteristics of the battery [50, 52, 53, 60–63]. Essentially, they are lumped models with relatively few parameters making them applicable for explicit approximation of the heat generated from the electrochemical heat reactions and implicit calculation of the heat produced from the bulk electrons displacement along the electrodes.

A wide range of ECM has been applied to calculate SOC, state of health (SOH) and electrical behaviour of Li-ion batteries used in vehicle applications. The simplest ECM, called the Rint model, consists of a voltage source as OCV and an internal resistance [64, 65]. The Rint model can accurately simulate the voltage-current characterization of the battery at the constant current charge/discharge processes, nonetheless, it has limitations in simulation of dynamic response of the battery to transiently charging/discharging load profile.

This problem is addressed by adding parallel resistance-capacitor (RC) networks to the Rint model in order to describe the dynamic characteristics of the battery. There are numerous RC-based models available in the literature such as first order RC [54, 62, 66–68], second order RC [50, 52, 55, 65, 69, 70], and third order RC models [53]. It is shown that number of RC branches in the equivalent circuit is an important factor that determines the accuracy of the prediction and complexity of the model. Nonetheless, by increasing the number of RC-branches, the computational cost will increase which is not favorable.

The polarization characteristic of the battery can be simulated by the first order model to some extent, but the difference between concentration polarization and electrochemical polarization leads to inaccurate results at the end of the charge or discharge process. It is shown that this issue is addressed in a third order RC models that consists of three parallel RC-networks to refine the description of polarization characteristics and simulate the concentration polarization and the electrochemical polarization separately. In spite of the popularity of ECM for describing the dynamic $I-V$ characteristics of batteries, most of them are developed based on isothermal conditions, and the parameters are considered constant over a wide range of temperature, limiting their use in on-board battery management system [60], also there are few studies in the literature, that applied this approach to provide a basis for exploring thermal management strategies for Li-ion batteries.

Verbrugge *et al*. [62] used a first-order ECM to simulate the lumped electro-thermal behaviour of nickel metal hydride (NiMH) battery over a range of conditions applicable to electric vehicle

applications. A similar model was adapted to a cylindrical shaped Li-ion battery in Ref. [51], in which a second-order ECM was coupled to a lumped thermal model through heat generation term and temperature dependency of ECM parameters. Since former studies are based on lumped models, they fail to provide information about the the local temperature distribution along the battery.

Miranda *et al*. [52] and Saw *et al*. [53] apply an ECM based thermal model to analyze the one-dimensional thermal response of $LiFePO_4$ batteries. The ECM used in Miranda work was extended to a wider operating conditions in terms of temperature (10-40 °C) and current (12–30 A).

Sun *et al*. [54] adapted the ECM approach to analyze the thermal performance of Li-ion battery pack. Their study incorporated a 3D-pack-level sub-model, a 1D-battery pack network sub-model, and a 3D-thermal and electrical coupled cell/module level sub-model to quickly predict the battery temperature variation across the pack.

The potential distribution and temperature evolution in a large-scale Li-ion battery were studied by Jung *et al*.[55] through a multi-dimensional electro-thermal model. A second order ECM model was employed to approximate the heat generated inside the battery and the electrochemical reaction current density. The model parameters were determined as function of both state-of-charge (SOC) and temperature which were implemented by bilinear interpolation method.

ii) *Fitting function-based Models*

The fitting function is basically equivalent to the Rint model where OCV and electrochemical conductance (corresponding to the battery inertial resistance) are considered in simulating the $I-V$ characteristics of the battery. The fitting function approach originally, proposed by Gu [71], is based on a linear polarization expression confirmed by experimental observations [71] and electrochemical simulations [32] that formulates the linear dependency of the discharge voltage on the current density at a fixed depth-of-discharge (DOD). From the collected $I-V$ data during standard constant-current processes, parameters in the polarization expression (OCV and electrochemical conductance) can be defined as functions of DOD.

Since the fitting parameters in the polarization expression are only functions of DOD, and they do not have any time dependent relaxation term, the model is limited in simulating dynamic response of the battery to a transient charging/discharging load profile. To simulate the performance of the battery under a more dynamic duty cycle, RC-based models are recommended. However, the fitting function model is capable of describing the galvanostatic behaviour of the battery, where a high rate of heat generation is involved, that can be applied in battery cooling system design.

Kwon *et al*. [40] applied a simple ECM model (Rint), originally proposed by Gu [71], to construct a two-dimensional electrical model to predict the potential field and current density distribution in the positive and negative electrodes of Li-ion batteries. The data collected at a fixed environmental temperature was used to determine the model parameters.

Following Kwon [40], Kim *et al*. [41, 56, 57] proposed an electro-thermal model to simulate the potential and temperature distributions of the cell. The presented electro-thermal model was employed to accommodate the dependence of the discharge behaviour on the environmental temperature [58]. Recently, Wu *et al*. [59] extended the Kim *et al*. model to study the effect of heat generated by the electrical contact resistance between the tab and the leading cable on the temperature distribution of battery.

Although the fitting function model offers a level of simplicity that enables one to obtain analytical solutions for the governing equations, all the above-mentioned studies used numerical approach to model electrical and thermal distribution inside the battery. From the computational point of view, analytical solutions are highly in demand because they are continuous in the independent variables, and show explicitly how the parameters of the system are involved. Furthermore, analytical solutions give much insight into a system, which is one of the primary objectives of modeling.

As the summery to this section, to the best knowledge of the author, the lack of information on the the electro-thermal modeling of the Li-ion battery cell in the available literature can be listed as below:

- No available closed-form analytical model that can describe the evolution of temperature in the batteries for different discharge rates considering multi-dimensional heat conduction, orthotropic thermal conductivities, and time dependent and temperature dependent heat generation terms. Such a model that can be easily adapted to different types of batteries in terms of geometry and chemistry.

- No theoretical model to predict the distribution of potential and current density in the electrodes that can be used for the design of electrode and current collectors.

- Lack of an analytical electro-thermal model accounting for all the main source of heat generation occurring in the large-scale battery.

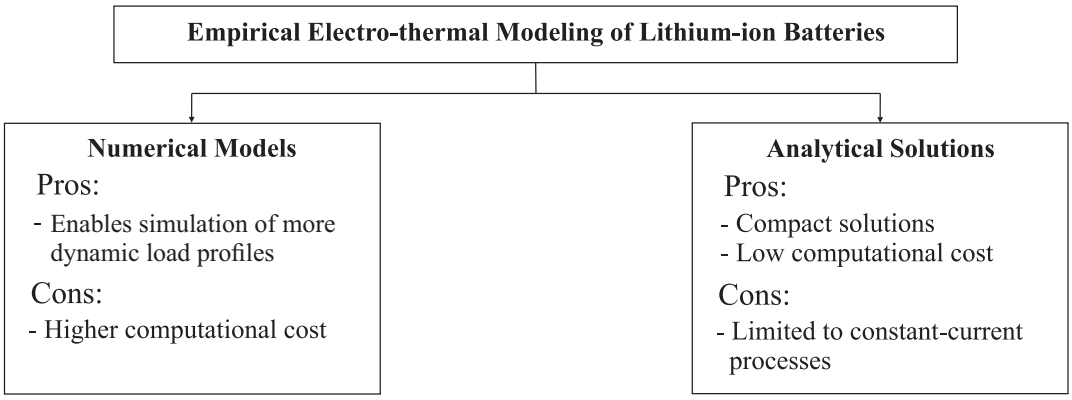

Figure 2.4: Pros and cons related to numerical and analytical approaches applied in electro-thermal model development.

2.4 Scope of thesis

The goal of this project is to present a complete range of computationally efficient modeling approaches to study how temperature distribution affects the performance of a battery cell. This would serve as a tool to design models characterizing the thermal behavior of Li-ion batteries to be applied in the area of performance and thermal management studies for battery pack cooling systems. To meet these objectives, the model must be both sufficiently simple to be executed almost in real-time, and accurate enough to provide a reasonable estimation of thermal dynamics inside the cell. Computationally efficient models that can provide a reasonable estimate of the cell electro-thermal field, with limited calibration effort, can be useful tools for battery pack designers and integrators.

As presented in Fig. 2.4, the modeling methodology presented in this thesis can be divided into main parts: *i*) analytical solutions and *ii*) numerical simulations.

Part i): A general three-dimensional thermal solution is proposed to predict temperature distribution inside a prismatic shaped battery considering multi-dimensional heat conduction, orthotropic thermal conductivities, and time dependent and temperature dependent heat generation terms. To demonstrate the versatility of the model, the solution is adapted to study the thermal behaviour of the prismatic and cylindrical NiMH batteries during fast charging processes. Thereafter, using the battery testing setup designed in Laboratory of Alternative Energy Conversion (LAEC) at Simon Fraser University (SFU), the required experimental data (voltage and temperature profile) for model development and validation is collected. Based on the collected data, a new theoretical model is

proposed for potential and current density distributions within the cell. By coupling the proposed electrical model with the thermal model through heat generation term, a new Joulean heat is introduced to the energy equation to consider the heat produced from bulk electron movement in the electrodes.

Part ii): Using a finite element PDE solver, COMSOL MULTIPHYSICS, a numerical electro-thermal model is developed to simulate the local distribution of current, potential, and temperature of a Li-ion battery. The model is based on a second order RC model capable of dynamic response simulation. The ECM parameters are defined as functions of both SOC and temperature.

Chapter 3

Battery Testing Platform

As discussed in the previous chapter, empirical models that mimic the electrochemical performance of battery can be applied to the development of stand-alone electro-thermal models. These models can be implemented in the control algorithms for battery management system with minimum computational effort. The empirical model, requires experimental data in order to determine the model components as a function of the operating parameters. Accordingly, the focus of this chapter is to design a programmable and regenerative multi-channel battery testing platform to collect the experimental data required for the model development and validation.

3.1 Sample battery

Pouch-type Li-ion cells, ePLB C020 battery fabricated by EiG Corporation in South Korea, was considered as the sample battery. The batteries were provided by our industrial partner Future Vehicle Technologies. This battery uses $Li[Ni\,Co\,Mn_2]O_2$ and graphite as active materials at the cathode the and anode, respectively. The nominal voltage and capacity of the battery are 3.65 V and 20 Ah, with specific energy of 175 $Wh\,kg^{-1}$. The weight of the battery is approximately 407 g, thus, its energy content is approximately 71 Wh. Mechanical and electrical specifications of the battery are listed in Table 3.1. Fig. 3.1a shows the layered structure of the battery core, i.e., electrode-separator stack. The sample battery includes 18 negative electrodes, 17 positive electrodes, and 36 layers of polymer (polypropylene) separator sheets. The electrodes, that include current collector foils laminated by thin layers of a polymer (polyethylene oxide), are connected in parallel. Aluminum and copper foils are used as current collectors in positive and negative electrodes, respectively. The

Table 3.1: Specifications of ePLB C020, EiG battery.

Mechanical characteristics	
Thickness (L_1)	7 [mm]
Width (L_2)	125 [mm]
Height (L_3)	195 [mm]
Weight	407 [g]
Electrical characteristics	
Nominal voltage	3.65 [V]
Nominal capacity	20 [Ah]
Specific energy	175 [Wh kg^{-1}]
Energy density	370 [Wh L^{-1}]
Operating conditions	
Recommended voltage limit for discharge	3 [V]
Lower voltage limit for discharge	2.5 [V]
Maximum continuous discharge current	5C
Maximum discharge current (peak¡10 s)	10C
Operating temperature	Between -30$°C$ and +40$°C$

Table 3.2: Thickness, thermophysical, and electrical properties of battery components [40, 41, 44].

Material/Layer	Thickness [μm]	Number of layers	Density [kh m^{-3}]	Heat capacity [J k^{-1} K^{-1}]	Thermal conductivity [W m^{-1} K^{-1}]	Electrical conductivity [S m^{-1}]
Aluminum current collector	21	17	2702	903	238	37.8×10^{6}
Copper current collector	12	18	8933	385	398	59.6×10^{6}
Separator sheet	25	36	1017 (wet)	1978 (wet)	0.34 (wet)	25×10^{-6}
Positive active material	70	34	2895 (wet)	1270 (wet)	1.58 (wet)	13.9 (wet)
Negative active material	79	36	1555 (wet)	1437 (wet)	1.04 (wet)	100 (wet)
Pouch (case)	162	2	1150	1900	0.16	-

polymer layers (electrodes and separator sheets) are porous media soaked in an electrolyte liquid, a mixture of ethylene carbonate and dimethyl carbonate, and accommodate active materials required in the battery chemistry. The battery core is packed in a polymer laminate aluminum pouch case as presented in Fig. 3.1c. For parallel connection of the cells, electrode tabs of the same type are welded together to form the battery terminals. The thickness and thermophysical properties of the battery core layers/materials are provided in Table. 3.2. The thermophysical properties reported in Table. 3.2 are obtained from the literature for a similar battery type [40, 41, 44]. However, in the following section a measured value for the heat capacity will be provided.

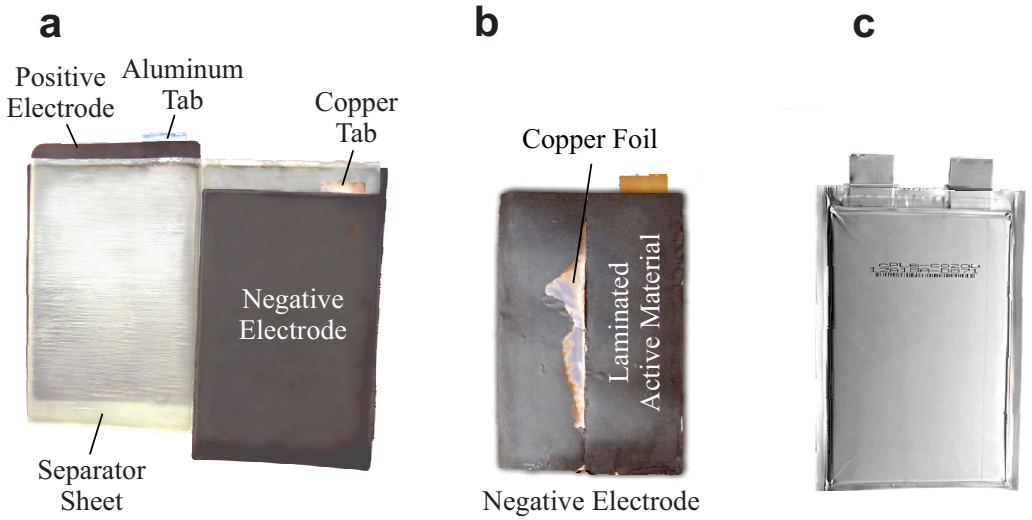

Figure 3.1: a) Core structure of the experimental battery. b) Layered structure of a negative electrode. c) The actual experimental battery with the pouch case.

3.1.1 Experimental equipment

Power processing unit

The power processing unit (ABC-150, AeroVironment, USA) shown in Fig. 3.2a, consists of two independent channels used to charge, discharge, and cycle the battery. Being bi-directional and operable in power mode makes ABC-150 a system for accurate EVs and HEVs battery testing. This load processing device offers power up to 125 k W, with a voltage range of 8 to 445 VDC. It has a maximum response time of 50 milliseconds and a typical response time of less than 10 milliseconds. Essentially, the battery testing requires implementation of a wide range of test programs and cycles. Different battery technologies have their own special characteristics that must be monitored or accounted for in testing. To account for all of these variations, the battery test system must have extremely flexible test automation. In this regard, Emerald software developed by Greenlight Innovation (Canada) was employed as it offers a powerful test scripting architecture able to meet all needed requirements. The software as a test manager, provides flexible test control including looping, branching, global and local stops conditions, and user-defined variables. Any load cycle including charge and discharge protocols should be scripted in Emerald software that can control the power processing unit. A PC, connected to the power processing unit through a controller area network (CAN) connection, is used for software-hardware communication and for data collection. A schematic of the experimental setup is shown in Fig. 3.2b.

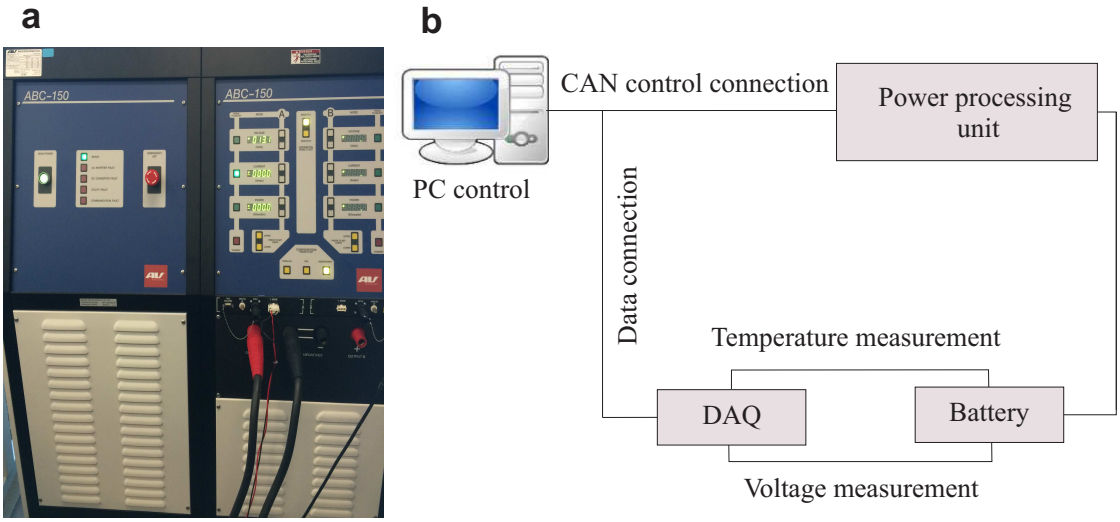

Figure 3.2: a) Power processing unit, (ABC-150, AeroVironment, USA), is applied to cycle the battery, b) The experimental setup for battery cycling and voltage and surface temperature measurement.

Data acquisition system (DAQ)

A fully configurable analog data acquisition system (DAQ) from Greenlight Innovation was used to collect temperature and voltage of cells with up to 100 Hz continuous data sampling. It consists of two modules, each contains 32 available slots for various analog input channels. The first 13 channels were used for voltage sensors in daisy-chain configuration, and the rest of them are allocated to temperature sensors. The collected data is displayed in the Emerald software for monitoring purposes, see Fig. 3.3; the data is also recorded to a data output file with a variable recording time to optimize data storage space and ease data analysis.

Accelerated rate calorimeter

The specific heat capacity and the amount of heat generation in a battery are important parameters to characterize the battery thermal behaviour, can be measured using an accelerated rate calorimeter (ARC) and a battery performance calorimeter (BPC, Thermal Hazard Technology, UK) as shown in Fig. 3.4. The operational temperature range of the calorimeter is from -40 to 200 °C, with a heat detection sensitivity at 0.02 K min^{-1}. The system enables specific heat capacity, c_p, measurements as a function of temperature. The calorimeter can operate in two different running modes: 1) adiabatic, which allows an accurate measurement of heat released from the batteries during cycling, and 2) isothermal, which functions in a similar way to an environmental chamber

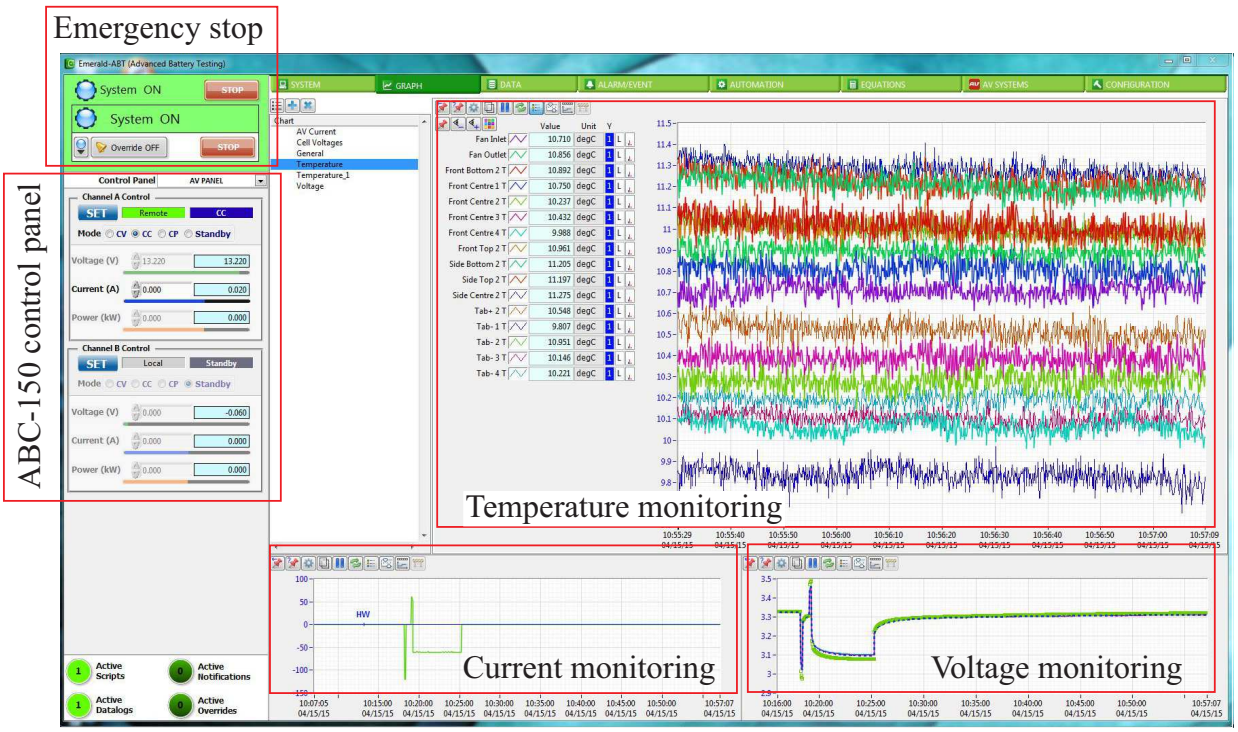

Figure 3.3: A demonstration of monitoring the collected data (temperature, voltage, and current) in the Emerald software.

(i.e., keeping track of the battery temperature). To ensure that the system operates in the desired manner, a calibration test should be performed prior to the any sample testing. The BPC calibration is generally conducted over the temperature range of -20 °C to 120 °C. The calibration sample is a piece of metal, ideally aluminum or copper due to their high thermal conductivity. The size of the calibration sample should be the same as the targeted battery. In this case, a block of aluminum with the same size of the experimental battery was used as the calibration sample.

Environmental chamber

To simulate different environmental conditions, an environmental chamber (Platinous H-series, ESPEC, USA) is used as shown in Fig. 3.5. The environmental chamber with an interior space of 900 liters, operating over a temperature range from -70 °C to 180 °C, and relative humidity range of 10 % to 98 %, is used for conducting the experiments.

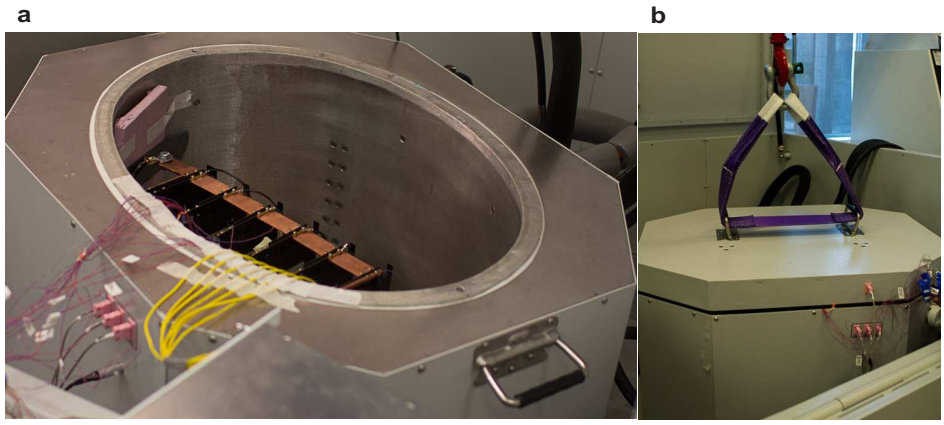

Figure 3.4: Battery performance calorimeter (PBC, Thermal Hazard Technology, UK) used to measure the specific heat measurement. a) Opened chamber for battery set-up, b) closed chamber for testing.

Figure 3.5: Environmental chamber (Platinous H-series, ESPEC, USA) used to simulate different environmental conditions.

3.1.2 Test procedure

Battery preparation

During battery testing, the temperature and voltage of the batteries should be monitored to assure they remain within the range recommended by the manufacturer. The most popular method of temperature monitoring is direct measurement via contact between a sensing element and part of the cell. In this study, T-type (copperconstantan) thermocouples with the accuracy of $\pm 0.5\,^{\circ}$C are used as temperature sensors. Owing to their stability and oxidation resistance, T-type thermocouples are suitable for temperature measurements from -200 to 350°C. The voltage at the battery tabs (terminals) and the temperature at different locations were collected through the DAQ system every 10 milliseconds. Each battery was equipped with T-type thermocouples attached to the battery

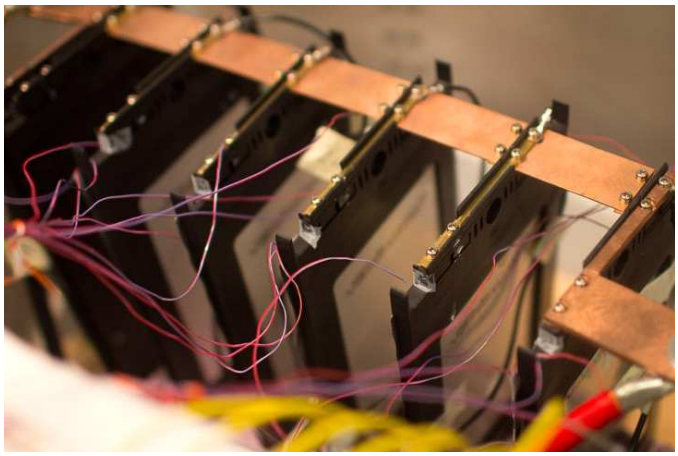

Figure 3.6: A demonstration of the experimental batteries with the measuring instruments: T-type thermocouples and voltage sensors attached to the batteries surface and tabs, respectively.

surface (two in the vicinity of the tabs, one at the center, and two at the bottom corners) and the voltage sensor connected to the tabs as shown in Fig. 3.6. A thermally conductive and electrical insulator thermal paste provided by Omega was applied to allow a thermal connection and prevent electrical connection between the tip of the thermocouples and the battery surface.

Specific heat capacity test

Using the ARC-calorimeter, the specific heat capacity, c_p, of the battery was measured over 300 to 320 K range of temperature. During the test, a heater mat, slightly smaller than the experimental cell, is sandwiched between two identical cells. After placing the sample in the ARC test chamber, the specific heat measurement test was performed by setting up the ARC to power the thermal mat and record the temperature rise over the chosen range. In Fig. 3.7, an sample of measured value for specific heat with respect to temperature is shown. Dependency of c_p on T is approximated by a quadratic polynomial fit

$$c_p(T) = -81481.2 + 518.523\,T - 0.811504\,T^2 \tag{3.1}$$

The above correlation was used for numerical simulations, and an average value of 1250 ($\mathrm{J\,kg^{-1}\,K^{-1}}$) was used in the analytical model.

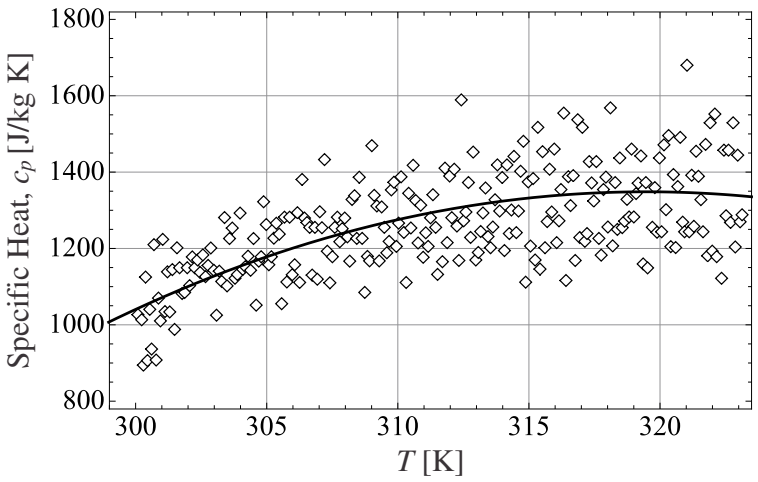

Figure 3.7: Dependency of specific heat capacity c_p on temperature. A quadratic polynomial (line) is fitted to experimental data (symbols).

Galvanostatic discharge test

The $I-V$ characteristics of the battery across different constant-current discharge processes is captured by galvanostatic discharge tests. Before every discharge test, the constant current-constant voltage (CC-CV) protocol (20 A, 4.15 V max with 2 A cutoff) was used to fully charge the battery at the room temperature of 22°C. For equilibrium voltage and temperature to be established, the fully charged batteries were allowed to rest for at least six hours before a discharging test.

Voltage response of the battery, V_{batt}, during discharge processes at various C-rates (0.5 C, 1 C, 2 C, 3 C and 4 C) was measured at a constant environmental temperature of 22 °C and the results are plotted in Fig. 3.8. During the discharge process, the batteries are subjected to natural convection cooling. Because of the excessive temperature rise (above the safety limit) in the battery during 4 C-rate discharge, the voltage measurement is terminated before completion of the process. In Chapter. 6, the data collected is applied to characterize the fitting function model and to validate the proposed analytical electro-thermal model.

Hybrid pulse power characterization test

To characterize the equivalent circuit model that will be discussed in Chapter 7, the batteries were cycled with hybrid pulse power characterization (HPPC) test at different environmental temperatures. Essentially, the HPPC test intends to determine dynamic power capability of the battery over the useable voltage range by using a test profile that incorporates both discharge and charge

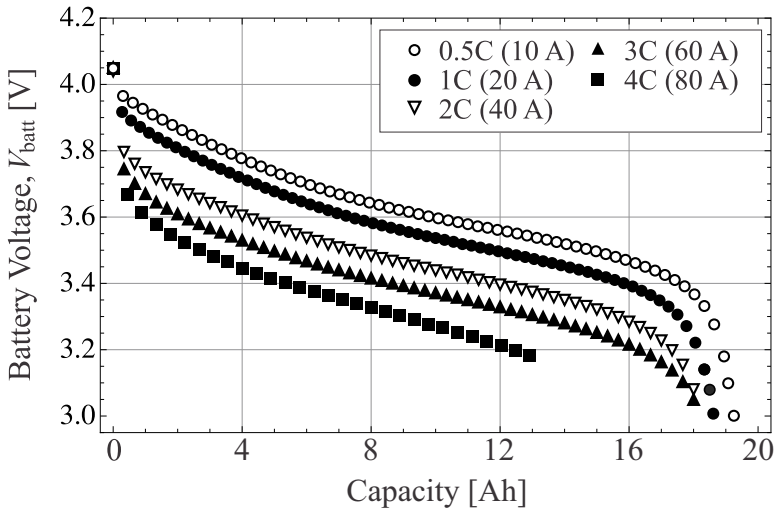

Figure 3.8: Measured voltage response of the battery during constant-current discharge processes at different discharge rates at environmental temperature of 22 °C.

Table 3.3: Relative currents for discharge and charge pulses in HPPC [72].

Pulse duration (s)	Cumulative time (s)	Relative currents
10	10	1.00
40	50	0
10	60	- 0.75

pulses [72]. The main profile is made up of single repetitions of the HPPC profile, separated by 10 % DOD constant current discharge segments and each followed by a 1 hour rest period to allow the cell to return to an electrochemical and thermal equilibrium condition before applying the next profile. The HPPC profile, presented in Fig. 3.9, determines the 10-second discharge-pulse and 10-second charge-pulse power capabilities at each 10 % DOD increment. The current values for the discharge and charge pulses are presented in Table 3.3 are selected from the *Battery Test Manual for Plug-In Hybrid Electric Vehicles* [72]. This study uses positive values for discharge current whereas charge (regen) values are negative.

Prior to executing HPPC profile, the batteries were first discharged to 100 % DOD under constant-current profile, relaxed for 1 hour and then charged to 100 % SOC under CC-CV protocol. The battery is relaxed for 1 hour to reach electrical and thermal equilibrium. The sequence of discharge/charge protocols, rest periods, pulse segments, and HPPC profiles is also illustrated in Fig. 3.9. The HPPC tests were performed at environmental temperatures of 0 °C, 25 °C, 45 °C, and 55 °C and the results are presented in Fig. 3.10.

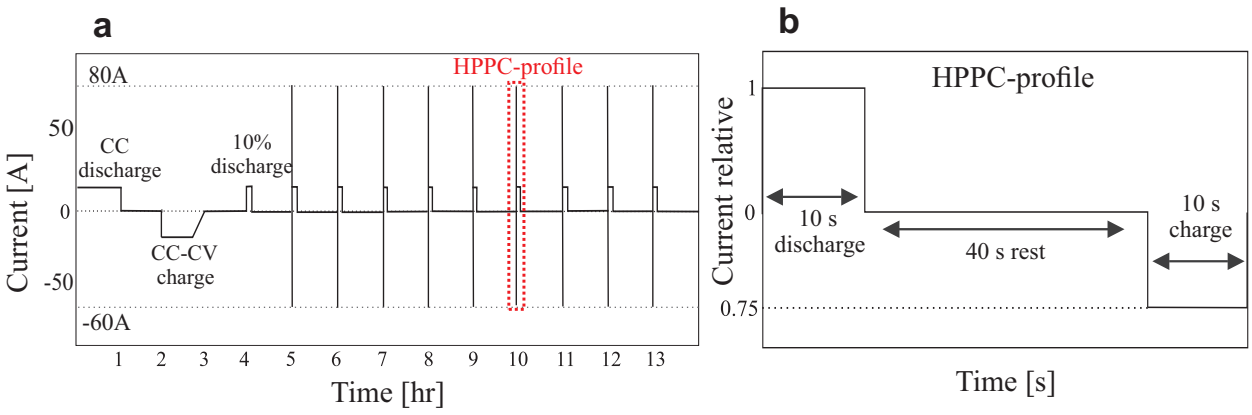

Figure 3.9: a) Complete Hybrid Pulse Power Characterization (HPPC) test, b) the HPPC pulse profile.

3.1.3 Summary

The experimental data required for model development and validation in the next chapters, were acquired in this chapter. Hence, in this chapter a programmable and regenerative multi-channel battery testing platform was designed to collect the experimental data including, galvanostatic tests and HPPC profile. A power processing unit, ABC-150 was applied to charge, discharge, and cycle the batteries. Emerald software, a test scripting tool, was applied to control the power processing unit, establish a battery safety profile based on the special characteristics recommended by manufacturer, and to provide different load cycle protocols. Using accelerated rate calorimeter, the specific heat capacity of the battery was measured over a temperature range of $300 - 320\,\mathrm{K}$. Different environmental conditions, from sub-ambient to warm-ambient, were simulated by the ESPEC environmental chamber. The voltage response of the battery to constant-current discharge processes and HPPC-profile required for the model development were provided in this chapter.

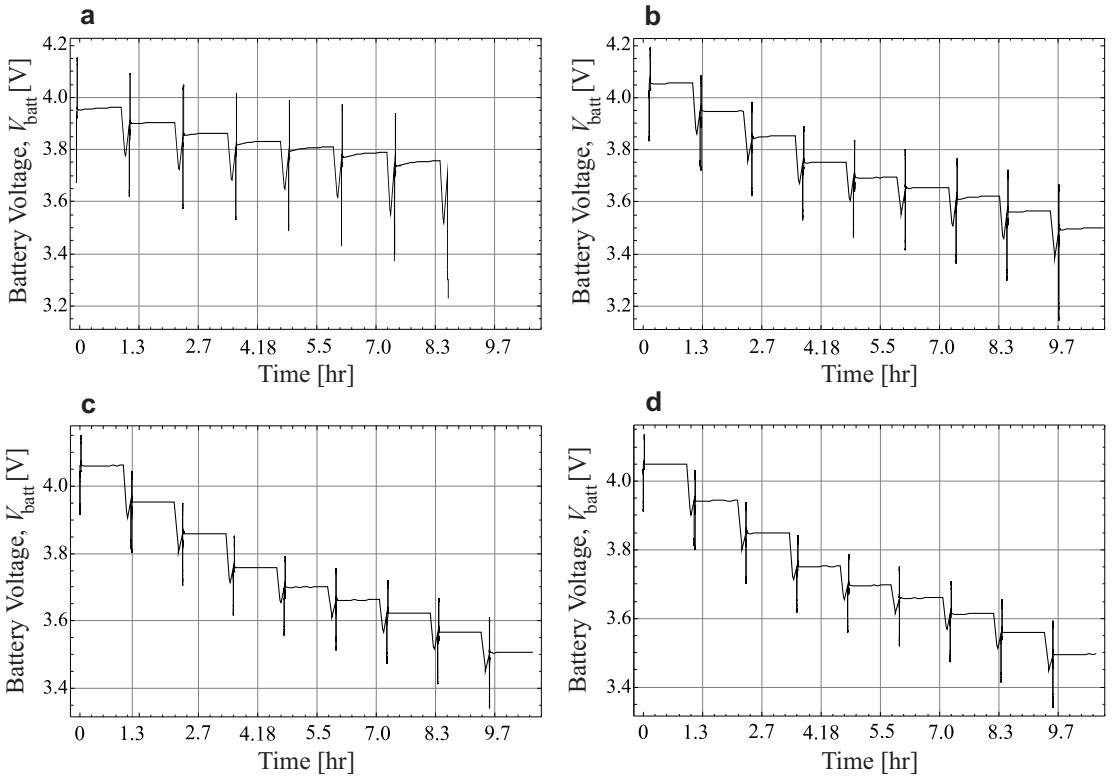

Figure 3.10: Voltage response of the battery to the Hybrid Pulse Power Characterization (HPPC) test at a) 0 °C, b) 25 °C, c) 45 °C, d) 55 °C.

Chapter 4

Transient Three-Dimensional Thermal Model for Batteries with Thin Electrodes

A three-dimensional analytical model is proposed to investigate the thermal response of batteries, with a plurality of thin electrodes, to heat generation during their operation. The model is based on an integral-transform technique that gives a closed-form solution for the fundamental problem of unsteady heat conduction in batteries with orthotropic thermal conductivities, where the heat generation is a function of both temperature and depth-of-discharge.

To demonstrate the versatility of the proposed solution, the model is applied to study the transient thermal response of a Li-ion battery operating at constant-current discharge and a nickel-metal hydride (NiMH) battery during fast charging processes at constant-currents.

4.1 Formulation of the problem

The core of the battery is considered as a three-dimensional rectangular orthotropic solid of length L_1, width L_2, and height L_3, and as the domain of the study. For better reading, a two-dimensional schematic of the domain is shown in Fig. 4.1. Heat is generated non-uniformly within the domain, while heat transfer with a surrounding medium is allowed at boundary surfaces. The unsteady temperature distribution inside the domain is described by a three-dimensional energy balance equation which only includes conduction terms,

$$\rho c_p \frac{\partial T}{\partial t} = \kappa_1 \frac{\partial^2 T}{\partial x_1^2} + \kappa_2 \frac{\partial^2 T}{\partial x_2^2} + \kappa_3 \frac{\partial^2 T}{\partial x_3^2} + \dot{g}, \quad 0 \le x_1 \le L_1, \quad 0 \le x_2 \le L_2, \quad 0 \le x_3 \le L_3, \quad t > 0, \tag{4.1}$$

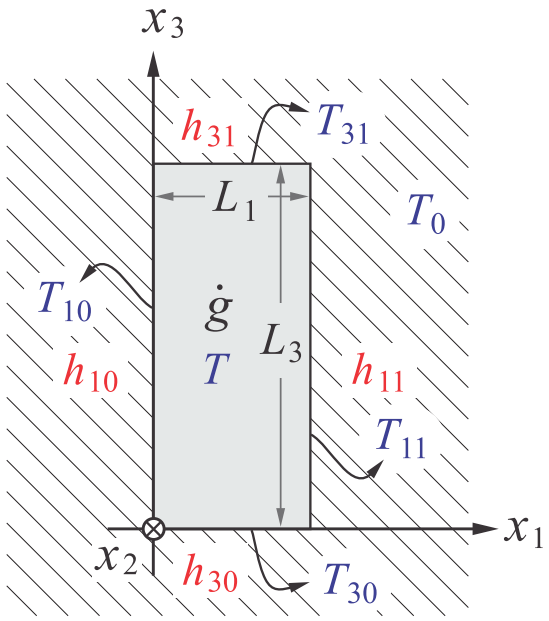

Figure 4.1: Two-dimensional schematic of the battery core in x_1–x_3 plane with internal heat generation $\dot{g}$, and heat dissipation at boundaries. The ambient temperatures is denoted by T_0.

in which t is time, and $\mathbf{x} = \{x_1, x_2, x_3\}$ represents the components of the position vector in Cartesian coordinate system. The functions $T(\mathbf{x}, t)$ and $\dot{g}(\mathbf{x}, t)$ denote the temperature and volumetric heat generation rate inside the battery core, respectively (see Fig. 4.1). The density, ρ, specific heat, c_p, and orthotropic thermal conductivities, κ_i, are the thermophysical parameters for the core region.

Convection thermal boundary conditions are applied at the surfaces of the battery case,

$$-\kappa_i \frac{\partial T}{\partial x_i} + \left[\frac{\delta_{\text{case}}}{\kappa_{\text{case}}} + \frac{1}{h_{i0,\text{case}}}\right]^{-1} (T_{i0} - T_0) = 0, \quad \text{at} \quad x_i = 0 \quad (i = 1,2,3), \tag{4.2a}$$

$$+\kappa_i \frac{\partial T}{\partial x_i} + \left[\frac{\delta_{\text{case}}}{\kappa_{\text{case}}} + \frac{1}{h_{i1,\text{case}}}\right]^{-1} (T_{i1} - T_0) = 0, \quad \text{at} \quad x_i = L_i \quad (i = 1,2,3) \tag{4.2b}$$

where $h_{ij,\text{case}}$ are the convective heat transfer coefficients at different surfaces of the case, and T_{ij} are the corresponding surface temperatures. The index, i, represents the direction of the normal vector on a boundary surface, while $j = 0$ and $j = 1$ denote surfaces at $x_i = 0$ and $x_i = L_i$, respectively (see Fig. 4.1). The thickness of the battery case and its thermal conductivity are denoted by δ_{case} and κ_{case}. The environment temperature, T_0, is assumed to be a constant.

The initial temperature of the domain is the same as environment temperature, T_0,

$$T = T_0, \quad \text{at} \quad t = 0. \tag{4.3}$$

In this study, we consider constant ambient temperatures; however, the method allows definition of ambient temperatures as a function of both space and time [73, 74].

The rate of heat generation inside the battery can be approximated from the well-known energy balance analysis proposed by Bernardi *et al*. [75],

$$\dot{g} = \pm \frac{I}{\mathscr{V}} \left[(V - V_{\text{oc}}) + T \frac{dV_{\text{oc}}}{dT} \right], \tag{4.4}$$

with positive and negative signs for charge and discharge processes, respectively. The parameters I and V denote operational current and voltage of the battery, and $\mathscr{V}$ is the battery core volume. Open circuit voltage (OCV) of the battery, also known as equilibrium potential, is denoted by V_{oc}. The term $I(V - V_{\text{oc}})/\mathscr{V}$ is the irreversible heat generation due to Joule heating, and the term $IT(dV_{\text{oc}}/dT)/\mathscr{V}$ is the reversible heat generation caused by the entropy change in electro-chemical reactions [75].

4.2 Analytical solution

Equation (5.2) is a linear energy balance equation for which an analytical solution is accessible. The key assumption in the derivation of the linear energy equation is that the thermophysical properties are assumed to be independent of temperature, which is generally acceptable over a reasonably narrow temperature range of interest (i.e., the desired operating temperature range for batteries). Furthermore, due to the porosity of battery components, the motion of the electrolyte is neglected, thus the convective terms do not appear in the governing energy equation.

To generalize the analysis, dimensionless quantities can be introduced. We use the largest value of κ_i/L_i^2, which happens to be in x_1 direction, to scale the governing equations, i.e., Eqs. (5.2), (5.3), (4.3), and (4.4).

The dimensionless coordinate system, ξ_i, and dimensionless time, τ, are defined as,

$$\xi_i = \frac{x_i}{L_i} \quad (i = 1,2,3), \quad \tau = \frac{\kappa_1/L_1^2}{\rho c_p/t}. \tag{4.5}$$

Rewriting the initial-boundary-value problem, i.e., Eqs. (5.2), (5.3), and (4.3), in terms of dimensionless position and time gives,

$$\frac{\partial \theta}{\partial \tau} = \frac{\partial^2 \theta}{\partial \xi_1^2} + K_2 \frac{\partial^2 \theta}{\partial \xi_2^2} + K_3 \frac{\partial^2 \theta}{\partial \xi_3^2} + \dot{G}, \quad 0 \le \xi_1 \le 1, \quad 0 \le \xi_2 \le 1, \quad 0 \le \xi_3 \le 1, \quad \tau > 0, \tag{4.6}$$

with the boundary conditions,

$$-\frac{\partial\theta}{\partial\xi_i}+\mathrm{Bi}_{i0}\theta_{i0}=0, \quad \text{at} \quad \xi_i=0 \quad (i=1,2,3), \tag{4.7a}$$

$$+\frac{\partial\theta}{\partial\xi_i}+\mathrm{Bi}_{i1}\theta_{i1}=0, \quad \text{at} \quad \xi_i=1 \quad (i=1,2,3), \tag{4.7b}$$

and the initial condition,

$$\theta=0, \quad \text{at} \quad \tau=0. \tag{4.8}$$

In Eq. (4.6), K_i and $\dot{G}$ are the dimensionless thermal conductivities and heat generation, respectively, and in the transformed boundary conditions [cf. Eq. (4.7)] Bi_{ij} are Biot numbers,

$$K_i=\frac{\kappa_i/L_i^2}{\kappa_1/L_1^2} \quad (i=1,2,3), \quad \dot{G}=\frac{\dot{g}}{\kappa_1/L_1^2}, \quad \mathrm{Bi}_{ij}=\frac{h_{ij}L_i}{\kappa_i} \quad (i=1,2,3;j=0,1), \tag{4.9}$$

The temperature rise inside the battery core is denoted by θ, and the temperature rise on its boundaries are θ_{ij},

$$\theta=T-T_0, \quad \theta_{ij}=T_{ij}-T_0. \tag{4.10}$$

The transformed system [cf. Eqs. (4.6)–(4.8)] that describes temperature rise with respect to the dimensionless space and time, is solved analytically using a finite-integral transform technique, as described below.

The triple integral transformation and the inversion formula for temperature function are defined as [73],

$$\overline{\theta}(\lambda_{1l},\lambda_{2m},\lambda_{3n},\tau)=\int_{\xi_1'=0}^{1}\int_{\xi_2'=0}^{1}\int_{\xi_3'=0}^{1}\psi\left(\lambda_{1l},\xi_1'\right)\cdot\psi\left(\lambda_{2m},\xi_2'\right)\cdot\psi\left(\lambda_{3n},\xi_3'\right) \cdot\theta\left(\xi_1',\xi_2',\xi_3',\tau\right)\cdot d\xi_1'\cdot d\xi_2'\cdot d\xi_3', \tag{4.11}$$

and,

$$\theta(\xi_1,\xi_2,\xi_3,\tau)=\sum_{l=1}^{\infty}\sum_{m=1}^{\infty}\sum_{n=1}^{\infty}\psi(\lambda_{1l},\xi_1)\cdot\psi(\lambda_{2m},\xi_2)\cdot\psi(\lambda_{3n},\xi_3)\cdot\overline{\theta}(\lambda_{1l},\lambda_{2m},\lambda_{3n},\tau). \tag{4.12}$$

The functions $\psi(\lambda_{1l},\xi_1)$, $\psi(\lambda_{2m},\xi_2)$, and $\psi(\lambda_{3n},\xi_3)$ are the transformation kernels (normalized eigenfunctions) in ξ_1, ξ_2, and ξ_3 directions,

$$\psi(\lambda_i,\xi_i)=\frac{\phi(\lambda_i,\xi_i)}{\alpha_i^{1/2}} \quad (i=1,2,3), \tag{4.13}$$

and $\phi\left(\lambda_i, \xi_i\right)$ are eigenfunctions of the following Sturm–Liouville system corresponding to Eqs. (4.6) and (4.7),

$$\frac{d^2\phi}{d\xi_i^2} + \lambda_i^2 \phi = 0 \quad (i = 1,2,3), \tag{4.14a}$$

$$-\frac{d\phi}{d\xi_i} + \mathrm{Bi}_{i0}\phi = 0, \quad \text{at} \quad \xi_i = 0 \quad (i = 1,2,3), \tag{4.14b}$$

$$+\frac{d\phi}{d\xi_i} + \mathrm{Bi}_{i1}\phi = 0, \quad \text{at} \quad \xi_i = 1 \quad (i = 1,2,3), \tag{4.14c}$$

In Eqs. (4.13) and (4.14), λ_i denote an infinite list of eigenvalues in ξ_i direction. In Eqs. (4.11) and (4.12) components of λ_i in ξ_1, ξ_2, and ξ_3 directions are denoted by λ_{1l}, λ_{2m}, and λ_{3n}, respectively. The subscripts l, m, and n are the indices for the list components. The eigenvalues in each direction are positive roots of the following transcendental equation [73],

$$\tan\lambda = \frac{\lambda\left(\mathrm{Bi}_{i0} - \mathrm{Bi}_{i1}\right)}{\lambda^2 - \mathrm{Bi}_{i0}\,\mathrm{Bi}_{i1}}, \quad (i = 1,2,3). \tag{4.15}$$

Eigenvalues normalization factors, α_i, which appears in Eq. (4.13), are obtained as [73],

$$\alpha_i = \frac{1}{2}\left[\left(\lambda_i^2 + \mathrm{Bi}_{i0}^2\right)\left(1 + \frac{\mathrm{Bi}_{i1}}{\lambda_i^2 + \mathrm{Bi}_{i1}^2}\right) + \mathrm{Bi}_{i0}\right], \quad (i = 1,2,3). \tag{4.16}$$

The integral transform of Eq. (4.6), according to transformation (4.11), yields the following ordinary differential equation for $\bar{\theta}$,

$$\frac{d\bar{\theta}}{d\tau} + \Delta_{lmn}\bar{\theta} = \bar{\dot{G}}, \quad \text{with} \quad \bar{\theta}\left(\tau\right) = 0 \quad \text{at} \quad \tau = 0. \tag{4.17a}$$

Δ_{lmn} will be defined in the following sections as the solution is applied to two different batteries.

Quantities with a bar refer to transformed quantities as given by Eq. (4.11), i.e.,

$$\bar{\dot{G}}\left(\lambda_{1l}, \lambda_{2m}, \lambda_{3n}, \tau\right) = \int_{\xi_1'=0}^{1}\int_{\xi_2'=0}^{1}\int_{\xi_3'=0}^{1} \psi\left(\lambda_{1l}, \xi_1'\right)\cdot\psi\left(\lambda_{2m}, \xi_2'\right)\cdot\psi\left(\lambda_{3n}, \xi_3'\right) \cdot\dot{G}\left(\tau\right)\cdot d\xi_1'\cdot d\xi_2'\cdot d\xi_3', \tag{4.17b}$$

Equation (4.17a) is a first-order, linear, and inhomogeneous ODE with a constant coefficient Δ_{lmn}. Its solution $\bar{\theta}\left(\lambda_{1l}, \lambda_{2m}, \lambda_{3n}, \tau\right)$ can be obtained as,

$$\bar{\theta} = \exp\left(-\Delta_{lmn}\,\tau\right)\left[\int_\tau \bar{\dot{G}}(\tau)\exp\left(\Delta_{lmn}\,\tau\right)d\tau + \mathscr{C}\right], \tag{4.18}$$

for which the corresponding integrating constant $\mathscr{C}$ must be evaluated from the given initial condition, $\bar{\theta}\left(\lambda_{1l}, \lambda_{2m}, \lambda_{3n}, 0\right) = 0$. Substitution of this solution into the inversion formula (4.12) gives the final solution in series form.

In Eqs. (4.11) and (4.12), when a double integral and its corresponding summation are used (instead of the triple ones), a two-dimensional solutions can be obtained by following the presented procedure. Chapter 6 will describe the adaption of this solution to a two-dimensional thermal model.

4.3 Application of analytical solution of thermal model to pouch-type Li-ion batteries

Determination of the volumetric heat generation rate $\dot{g}(\mathbf{x},t)$ inside the battery is one of the most challenging tasks in thermal modeling of battery systems. Complexities associated with this task are rooted in the strong coupling of heat generation rate to the rate of chemical reactions, current density distribution, and local Joule heating effects inside the battery core [33, 76, 77]. In this part of the study, only the heat generated from the chemical reactions has been considered; to complete our model, the effect of local Joule heating is included in Chapter. 6.

Based on Eq. (4.4), the source for temperature rise, $\dot{G}$, in Li-ion batteries is,

$$\dot{G} = \frac{\dot{g}}{\kappa_1/L_1^2} = \pm\dot{G}_{\text{irrev}} \pm \dot{G}_{\text{rev}} \pm \dot{G}_0, \tag{4.19}$$

with positive and negative signs for charge and discharge processes, respectively. The terms in Eq. (4.19) and the positive constant, α, are,

$$\dot{G}_{\text{irrev}} = \alpha\,(V - V_{\text{oc}})\,, \quad \dot{G}_{\text{rev}} = \alpha\theta\frac{\mathrm{d}V_{\text{oc}}}{\mathrm{d}\theta}, \quad \dot{G}_0 = \alpha T_0\frac{\mathrm{d}V_{\text{oc}}}{\mathrm{d}\theta}, \quad \text{and} \quad \alpha = \frac{I/\mathscr{V}}{\kappa_1/L_1^2}, \tag{4.20}$$

Accordingly, the $\bar{\dot{G}}$ and Δ_{lmn} defined in Eq. (5.29) can be tailored for Li-ion battery as;

$$\bar{\dot{G}} = \pm\bar{\dot{G}}_{\text{irrev}} \pm \bar{\dot{G}}_0, \tag{4.21a}$$

$$\Delta_{lmn} = \lambda_{1l}^2 + K_2\lambda_{2m}^2 + K_3\lambda_{3n}^2 \mp \alpha\frac{\mathrm{d}V_{\text{oc}}}{\mathrm{d}\theta} \tag{4.21b}$$

In this study, we assume that open circuit potential, V_{oc}, linearly depends on temperature [44], that is, $\mathrm{d}V_{\text{oc}}/\mathrm{d}T = \text{constant}$.

4.3.1 Results and discussions

In this section, thermal behavior of a sample lithium-ion pouch cell during discharge processes is investigated using the proposed analytical approach. The required calculations, as presented in Section 5.2, are programmed symbolically in Mathematica© to obtain a generic solution in series

form, i.e., Eq. (4.12). It should be noted that compared to the existing multi-dimensional numerical approaches, e.g. Refs. [8, 9, 43, 44, 46–48, 56], our analytical model demands minimum numerical effort, which is required for evaluation of eigenvalues from the transcendental equation [cf. Eq. (4.15)].

Thermophysical properties of the sample lithium-ion battery

This section demonstrates how to apply the proposed analytical solution to investigate the transient thermal behaviour of pouch-type Li-ion cell introduced in Section 3.1.

Density, heat capacity, and thermal conductivity of porous polymer layers in the electrodes and separator sheets must be measured after they are soaked in the electrolyte liquid. Since heat capacity and thermal conductivity of battery components are not reported by the manufacturer, the data provided in Table. 3.2 is used to estimate the battery thermophysical properties.

To avoid the complexities associated with multi-material multi-layered structure of the battery [cf. Fig. 3.1], we use averaged/effective transport properties in this study. The product value of density and heat capacity can be averaged based on density, heat capacity, and volume of each layer (component) [15, 44],

$$\rho c_p = \frac{\sum_{j=1}^{N} \rho_j c_{p,j} \mathscr{V}_j}{\mathscr{V}} = 2767.45 \left[\mathrm{kJ/m^3K}\right], \tag{4.22}$$

for which the required data are provided in Tables 3.1 and 3.2. The quantity $\mathscr{V}$ is the total battery volume, $\mathscr{V}_j$ is the volume of the jth component (layer), and N is the total number of components (layers). Furthermore, the concept of *equivalent resistance network* can be employed to define effective thermal conductivity in different directions. There are series thermal resistors in the x_1 direction and parallel thermal resistors in the x_2 and x_3 directions. Accordingly, by using the data from Tables 3.1 and 3.2, through-plane and in-plane orthotropic conductivities are evaluated as [44],

$$\kappa_1 = \frac{\sum_j \delta_j}{\sum_j (\delta_j/\kappa_j)} = 0.97 \ [\mathrm{W\,m^{-1}\,K^{-1}}], \tag{4.23a}$$

$$\kappa_2 = \kappa_3 = \frac{\sum_j \delta_j \kappa_j}{\sum_j \delta_j} = 26.57 \ [\mathrm{W\,m^{-1}\,K^{-1}}], \tag{4.23b}$$

where δ_j denotes the thickness of the jth component (layer) in x_1 direction, and $\sum_j \delta_j = L_1$.

It must be emphasized that as a consequence of the laminated arrangement of the battery core, interfacial phenomena of contact resistance at porous-porous and porous-solid interfaces must be

considered in evaluation of effective thermal conductivities. However, for Li-ion polymer batteries, since the contact interfaces are wet due to the presence of the electrolyte liquid, the effects of contact resistance are assumed to be negligible. This simplification is usually justified given that thermal conductivities of electrolyte and polymer compounds are in the same order [44].

The pouch case of the battery is made of polyethylene-laminated aluminum foil. As reported in Tabel 3.2, since the thickness of the pouch is small, 162 mm, and its through-plane thermal conductivity is not very different from the battery bulk (compare to Eq. (4.23b)). For an accurate boundary treatment, the outer surface temperature of the case is related to surface temperature of the battery core; see Eq. 4.2b.

4.3.2 Battery temperature distribution

The dimensions of the battery as given in Table 3.1 are chosen to be $L_1 = 0.007$ m, $L_2 = 0.125$ m, and $L_3 = 0.195$ m. The effective thermophysical properties of the battery core are evaluated from Eqs. (5.1) and (4.22). In this part of the study, the experimental data, reported by EiG for its ePLB C020 cell, on variation of cell potential (voltage) versus depth-of-discharge (DOD) for different discharge rates, shown in Fig. 4.2, are applied. For discharge processes, based on the recommended voltage limit in Table. 3.1, the cut-off voltage of 3 V is considered. Heat generation rate inside the battery is approximated from Eq. (4.4). Since the capacity of the sample battery is 20 Ah, the empirical data for C/2, 1 C, 2 C, 3 C, and 5 C discharge rates, as shown in Fig. 4.2b, correspond to 10 A, 20 A, 40 A, 60 A, and 100 A discharge currents, during 2 h, 1 h, 30 min, 20 min, and 12 min process, respectively. In Fig. 4.2b, variations of open-circuit and operating voltages at different discharge currents are plotted versus dimensionless time, τ, where in account for Eq. (4.5), $t = 139.8\,\tau$. For different discharge modes, summation of irreversible heat generation, $\dot{G}_{\text{irrev}}(\tau)$, and the constant heat generation, $\dot{G}_0$, are plotted in Fig. 4.3 for $T_0 = 25^{\circ}C$. The term $V - V_{\text{oc}}$ is evaluated by fitting fifth-order polynomials to the data points in Fig. 4.2b, and using Eq. (4.20). Linear transformations in (4.5) and (4.19) can be used to relate the magnitude of G to g, which in our case is $\dot{g} = 19,796\,\dot{G}$. The sharp increase in heat generation at the end of discharge corresponds to large differences between OCP and operating voltages. Battery thermal management systems operate based on heat transfer at battery surfaces, and their design depends on a variety of parameters, including: *i*) the thermal management strategy, which can be either active or passive [78] or a combination; *ii*) the type of the coolant (gas or liquid); *iii*) coolant circulation design (flow passage area,

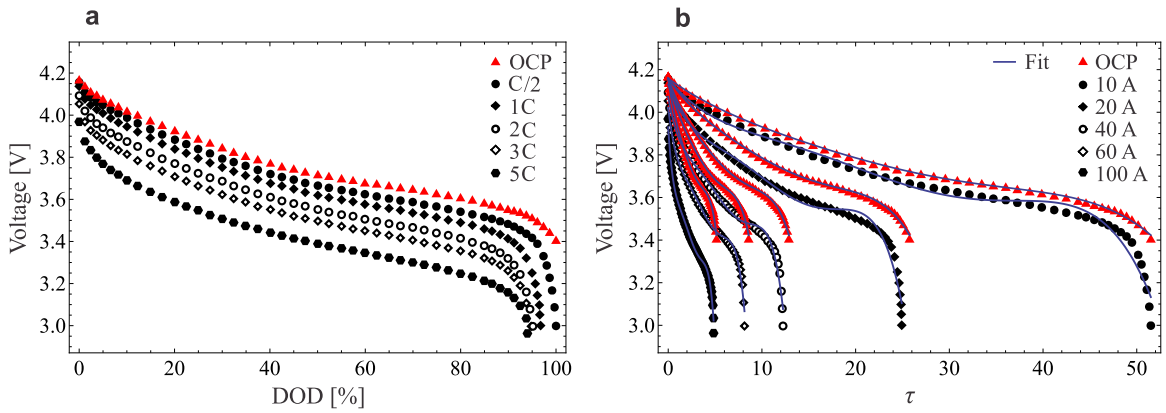

Figure 4.2: a) Experimental data reported by EiG Corp. on the variation of battery voltage with DOD at 25 °C for different discharge conditions in C-rate. A 1C-rate means that the current completely discharges the battery in 1 h. The red triangle symbols represent open circuit voltage (OCV); b) variation of open circuit voltage (OCV) and operation voltage of the battery versus dimensionless time, τ ($t = 139.8\tau$ s), for different discharge currents. Solid lines in plot (b) represent fifth-order polynomial fits to the experimental data.

laminar or turbulent flow, etc); *iv*) the size and the shape of the battery assembly; *v*) a recommended operational temperature for the battery. We assume small and moderate heat transfer coefficients to investigate the possibility of natural and forced convection cooling with air. The ambient and initial temperatures are assumed to be $T_0 = 298.15$ K, thus, based on the recommended operation temperature in Table 3.1, the maximum temperature rise of $\theta = 25$ K is acceptable during the battery operation, which means the critical temperature is $T_{\text{Cri}} = 323.15$ K. Here, only discharge operation mode is considered, but the same method can be used for charging process if variations of OCV and operation voltage are given during charging period.

Variation of the maximum temperature, T_{Max}, at the center of the battery $\xi = (0.5, 0.5, 0.5)$, minimum temperature, T_{Min}, at the corner of the battery $\xi = (0, 0, 0)$, and averaged battery temperature, T_{Ave}, as a function of battery utilization (DOD) are shown in Fig. 4.4. The average temperature is calculated as,

$$T_{\text{Ave}} = T_0 + \int_{\xi_1=0}^{1} \int_{\xi_2=0}^{1} \int_{\xi_3=0}^{1} \theta\,(\xi_1, \xi_2, \xi_3, \tau)\, \mathrm{d}\xi_1\, \mathrm{d}\xi_2\, \mathrm{d}\xi_3. \tag{4.24}$$

The temperatures T_{Max}, T_{Min}, and T_{Ave} obtained from the proposed analytical model for different discharge modes and heat transfer coefficients are compared to numerical results from the COMSOL Multiphysics finite element package (Version 4.2a). The comparison shows a good agreement between the analytical and numerical results. In the numerical calculation, the relative tolerance was set to 10^{-4}. The presented analytical results are obtained using only the first eigenvalue in each

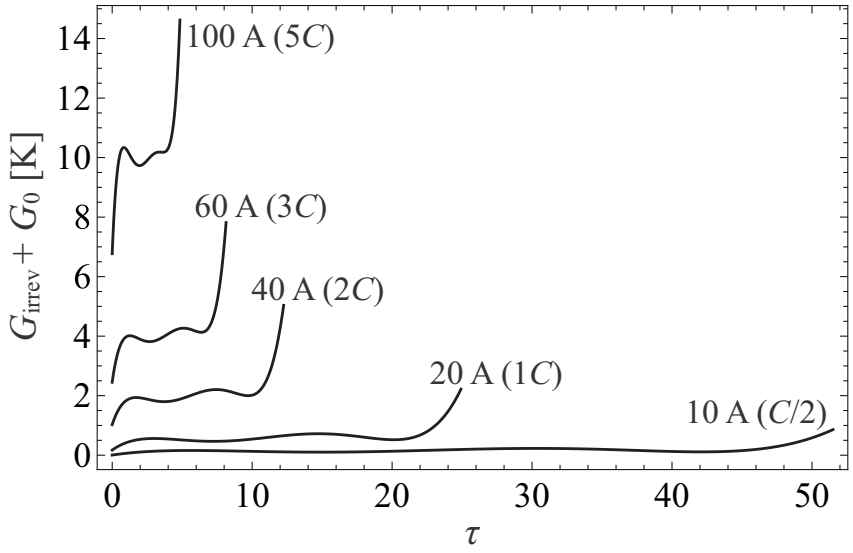

Figure 4.3: The Variation of $\dot{G}_{\text{irrev}} + \dot{G}_0$ versus dimensionless time, τ, is shown for different discharge currents at 25°C.

direction, which means the temperature is calculated only from the leading term of Eqs. (4.11) and (4.12),

$$T(\xi_1, \xi_2, \xi_3, \tau) \;=\; T_0 \;+\; \psi(\lambda_{11}, \xi_1) \;\cdot\; \psi(\lambda_{21}, \xi_2) \;\cdot\; \psi(\lambda_{31}, \xi_3) \;\cdot\; \overline{\theta}(\lambda_{11}, \lambda_{21}, \lambda_{31}, \tau), \quad (4.25)$$

and,

$$\overline{\theta}(\lambda_{11}, \lambda_{21}, \lambda_{31}, \tau) = \int_{\xi_1'=0}^{1} \int_{\xi_2'=0}^{1} \int_{\xi_3'=0}^{1} \psi\left(\lambda_{11}, \xi_1'\right) \cdot \psi\left(\lambda_{21}, \xi_2'\right) \cdot \psi\left(\lambda_{31}, \xi_3'\right) \cdot d\xi_1' \cdot d\xi_2' \cdot d\xi_3'. \quad (4.26)$$

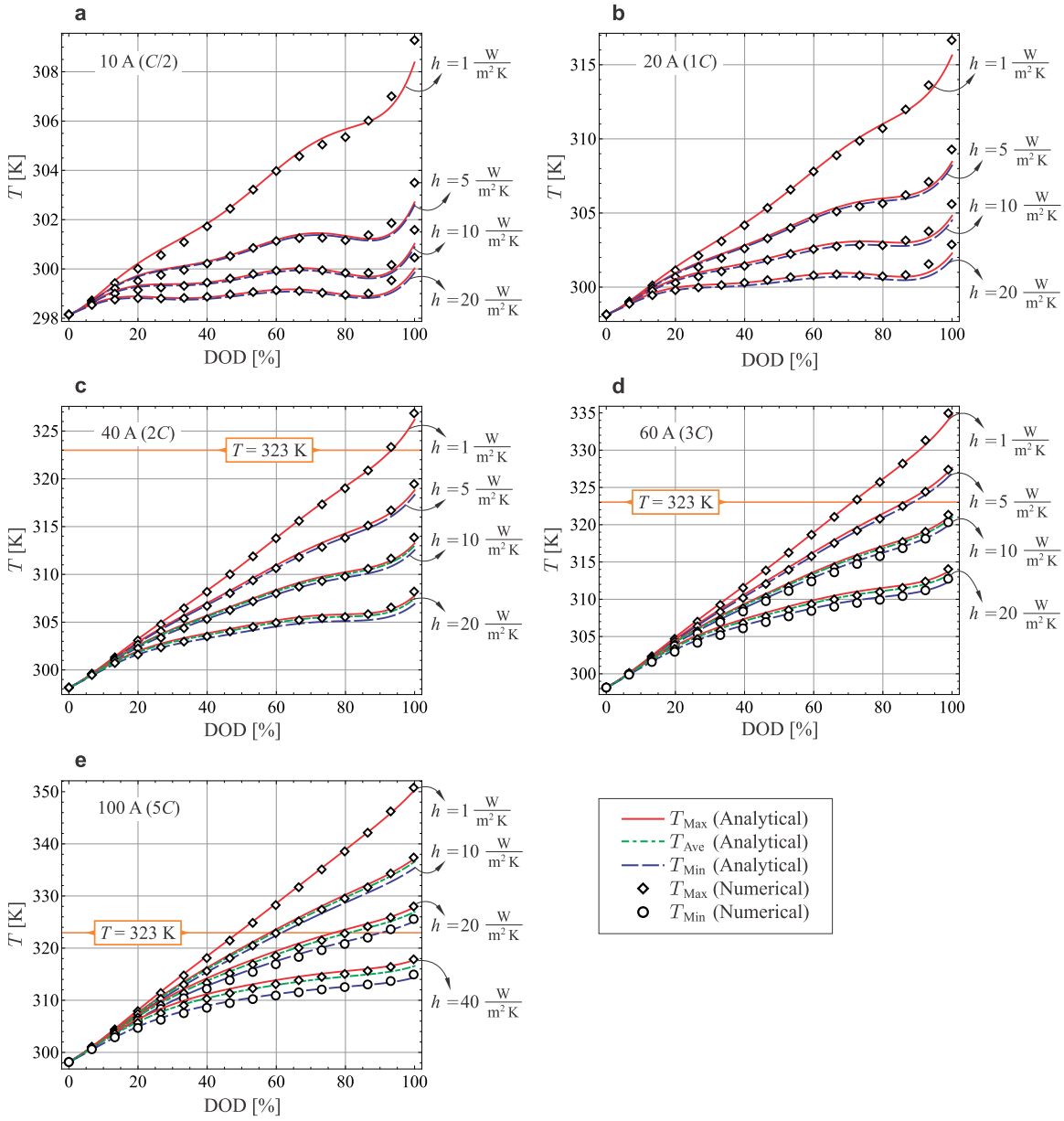

Figure 4.4: Temperature variation versus DOD is shown for different discharge rates. Maximum temperature at the battery center (red solid line), minimum temperature at the battery corner (blue long-dashed line), and average temperature (green dot-dashed line) are compared to numerical data for maximum temperature (diamond symbols) and minimum temperature (circular symbols). In plots (a)-(d), thermal response of the battery during 10 A, 20 A, 40 A, and 60 A discharge currents is shown for h_{ij}= $\{1, 5, 10, 20\}$ W m^{-2} K^{-1}. For the case of 100 A discharge current (plot e), higher heat transfer coefficients are examined to lower the temperature below the critical temperature $T_{\text{Cri}} = 323.15$ K.

The conclusion of more terms from the series solution is expected to improve the accuracy of the analytical results. Indeed, our calculations confirm that series solutions up to five terms provide a better matching with the numerical data, particularly for large Biot numbers. Further increase of the terms in the series solution increases the computational cost to a level comparable with the numerical solution, while improvements in the results are negligible.

Thermal behavior of an adiabatic battery is approximated by setting $h_{ij} = 1$ W m^2 K^{-1}, while $h_{ij} = \{5, 10\}$ W m^2 K^{-1} represent natural-convection cooling effects. Higher value of h_{ij} represents forced-convection cooling. Plot (a) and (b) in Fig. 4.4 show that for 10 A and 20 A discharge rates, cell temperature does not reach to the critical temperature of $T_{\text{Cri}} = 323.15$ K, and natural-convection cooling suffices to limit the temperature rise below 7 K. However, as shown in plots (c)-(e), for 40 A, 60 A, and 100 A discharge currents, thermal runaway might initiate in the cell as its temperature exceeds the critical temperature. To avoid overheating of the battery in such cases, minimum heat transfer coefficients of $h = 5$ W m^2 K^{-1}, $h = 10$ W m^2 K^{-1}, and $h = 40$ W m^2 K^{-1}, must be respectively applied to guarantee safe performance of the battery. The difference between T_{Max} and T_{Min} increases when higher rates of heat generation and surface heat dissipation are applied. In design of battery thermal management systems, such temperature non-uniformities are avoided, as they accelerate the rate of battery degradation.

Throughout the results, T_{Ave} is closer to T_{Max} rather than T_{Min}. This trend, which is more visible in Fig. 4.4e, indicates that due to low thermal conductivity of the battery bulk, low temperature regions are limited to a small portion of the battery volume, i.e., the corners.

As given in Eq. (4.20), the coefficient $\mathrm{d}V_{\text{oc}}/\mathrm{d}\theta$, dictated by battery chemistry [79], can significantly alter the magnitude of the heat generation rate. In Fig. 4.5, the increase of T_{Max} and T_{Min} are shown for $\mathrm{d}V_{\text{oc}}/\mathrm{d}\theta$=$\{0, 0.1, 0.4\}$ m V K^{-1}, while the battery is discharged at 3C-rate (60 A) and subjected to a cooling heat transfer coefficient of h_{ij}=10 W m^{-2} K^{-1}. When $T_{\text{Max}} - T_{\text{Min}}$ is small, one can use a lumped thermal model [80, 81] to approximate the thermal behavior of the battery. Conventionally, the Biot number is used to indicate the applicability of lumped thermal models; a Biot number less than 0.1 typically indicates a less than 5% error due to the lumped model assumption [82].

We define a surface-averaged Biot numbers for the battery,

$$\text{Bi}_{\text{Ave}} = \frac{1}{A} \sum_{i=1}^{3} \sum_{j=1}^{3} \text{Bi}_{ij} A_{ij}, \tag{4.27}$$

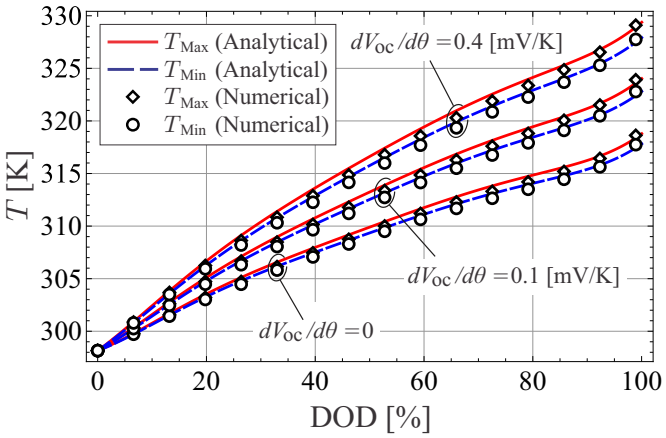

Figure 4.5: The minimum and maximum temperature rise are shown for $\mathrm{d}V_{oc}/\mathrm{d}\theta=\{0, 0.1, 0.4\}$ $\mathrm{m}^{-2}\,\mathrm{K}^{-1}$ during a 60 A discharge with $h_{ij} = 10$ $\mathrm{W\,m}^{-2}\,\mathrm{K}^{-1}$. Analytical results (lines) are compared to numerical data (symbols).

Table 4.1: Directional surface-averaged Biot numbers.

Heat transfer coefficient [$\mathrm{W\,m}^{-2}\,\mathrm{K}^{-1}$]	Bi_{1j}	Bi_{2j}	Bi_{3j}	$\mathrm{Bi}_{\mathrm{Ave}}$
$h = 5$	0.036	0.023	0.037	0.035
$h = 10$	0.072	0.047	0.073	0.071
$h = 15$	0.108	0.070	0.1110	0.106
$h = 20$	0.144	0.094	0.147	0.141
$h = 30$	0.216	0.141	0.220	0.213
$h = 40$	0.289	0.188	0.293	0.284

where A is the total battery surface area, and A_{ij} is the area of the surface normal to x_i direction; $j = 0$ and $j = 1$ denote the surface at $x_i = 0$ and $x_i = L_i$, respectively. Biot number Bi_{ij} characterizes the ratio of convective heat transfer to conductive heat transfer at A_{ij} surfaces. Since the thermal conductivity and dimensions of the battery are invariant, the only parameter affecting Bi_{ij} is h_{ij} . In Table 4.1 , Biot numbers for some cases are listed. The surface-averaged Biot number suggests that for $h < 15$ $\mathrm{W\,m}^{-2}\,\mathrm{K}^{-2}$ at all surfaces, a lumped thermal model is acceptable since $\mathrm{Bi}_{ij} < 0.1$. For forced-convective cases with $h > 15$ $\mathrm{W\,m}^{-2}\,\mathrm{K}^{-2}$ a multi-dimensional approach must be applied as $\mathrm{Bi}_{ij} > 0.1$; however, since Biot number in x_2 direction is always less than the other two directions (see Table 4.1), a two-dimensional model in x_1-x_3 plane is also acceptable. Note that an increase in h in x_2 direction can change the choice for a two-dimensional model. Our criterion for a proper choice of a two-dimensional model is that it should capture both minimum and maximum temperatures in the battery. The analysis of averaged Biot number and its application to simplify the thermal problem is valid only for homogeneous heat generation. In Fig. 4.6, temperature distribution at the end of a 100 A discharge process is shown on $\xi_1 = 1/2$, $\xi_2 = 1/2$, and $\xi_3 = 1/2$ planes.

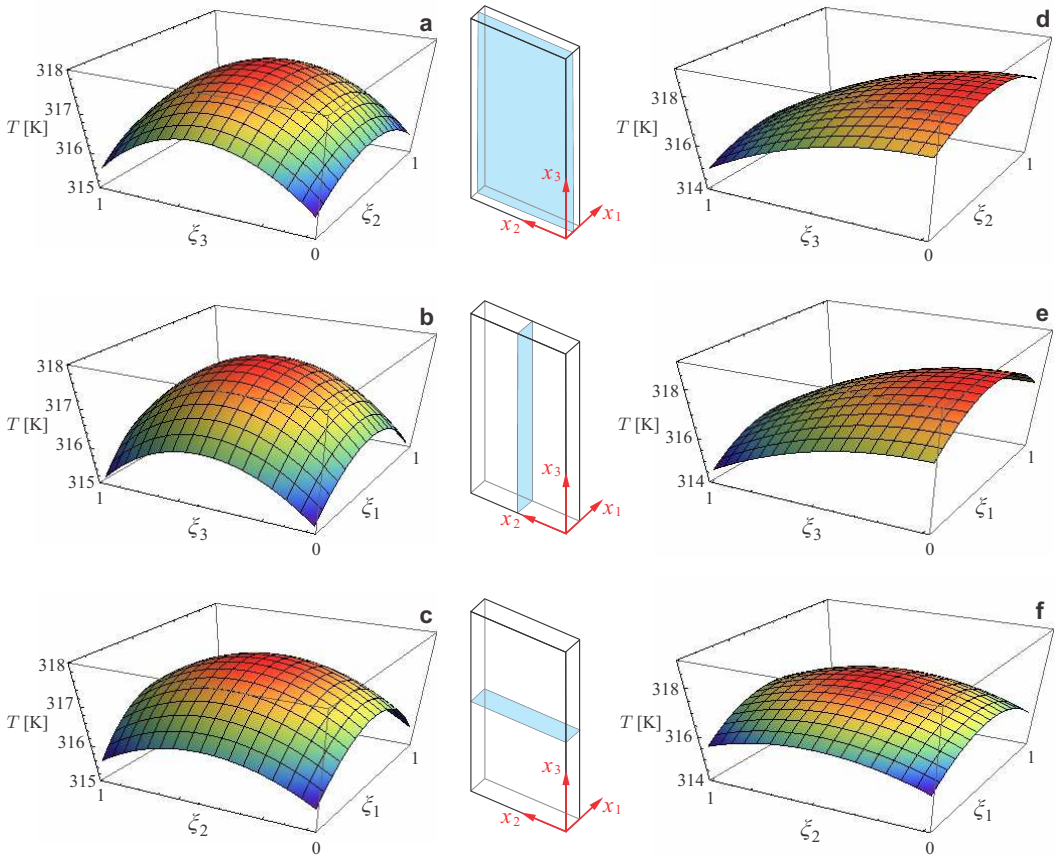

Figure 4.6: In plots (a)-(c), the temperature distribution at the end of a 100 A discharge process is shown for $h_{ij} = 40\,\mathrm{W\,m^{-2}\,K^{-1}}$ at all surfaces of the battery. In plots (d)-(f), the temperature distribution at the end of a 100 A discharge process is shown for $h_{31} = 1\,\mathrm{W\,m^{-2}\,K^{-1}}$ and $h_{ij} = 40\,\mathrm{W\,m^{-2}\,K^{-1}}$ for other surfaces. Ambient and initial temperature of 293.15 K was assumed. As a result of the system transformation, the results are mapped into a square region.

Plots (a)-(c) show the temperature distribution when $h_{ij} = 40\ \mathrm{W\,m^{-2}}$ is applied on all boundaries. Plots (d)-(f) correspond to the case in which $h_{31} = 1\ \mathrm{W\,m^{-2}}$, and on other surfaces $h_{ij} = 40\ \mathrm{W\,m^{-2}}$. The latter case is defined to examine the effects of non-uniform boundary conditions on the temperature distribution. In practical applications, indeed, at one side of the battery that is used for electrical connections, heat transfer coefficient differs from other sides (usually less). As a result of system transformation, i.e., Eq. (4.5), the solutions are mapped into a square region. A simple backward transformation can be used to remap the solutions into the original physical dimensions.

Plots (a)-(c) in Fig. 4.6 have the maximum temperature rise of $T_{\mathrm{Max}} = 317.7$ K, whereas the minimum temperature rise exists at the corners of ξ_1–ξ_3 plane. This confirms the result of Biot

number analysis, i.e., the best geometry choice for a two-dimensional modeling is a x_1–x_3 surface. This argument applies also for plots (d)-(f).

Finally, it should be emphasized that experimental observations show that maximum temperature in our sample battery occurs in the vicinity of battery tabs, where current density, and thus, Joulean heat generation are maximum. At this stage of the study, the thermal model has not been coupled with an electrical model to account for the Joulean heat, however, this work will be discussed in Chapter 6.

4.4 Application of analytical solution of thermal model to prismatic NiMH batteries

In this section, the proposed solution is adapted to investigate the thermal behaviour of NiMH batteries under fast-charging processes at constant currents.

To highlight the importance of operational temperature in NiMH batteries it suffices to mention that high temperatures lead to pressure buildup as a result of gas accumulation from the side reactions [83, 84], which in turn may cause structural failure, electrolyte leakage (capacity fade), and explosion hazard [85]. For NiMH batteries, it is evident that thermal issues are more pronounced during charging processes rather than discharging [86, 87].

For nickel based batteries, several rigorous mathematical models at the electrode level have been developed, for examples see Refs. [88–96]. Such models are suitable to, i) investigate underlying physicochemical mechanisms, ii) optimize electrode designs (electrode thickness and particle size) on scale-up battery systems, and iii) predict battery behavior in different operating conditions. However, for batteries detailed thermo-electro-chemical simulations are not plausible computationally; instead, stand-alone thermal models or electro-thermal models that focus on the thermal response of the battery under different operating conditions are desirable.

Similar to Li-ion batteries, the main challenge in thermal modeling of NiMH batteries is the evaluation of heat generation rate during charge/discharge processes. A common practice is to use direct or indirect calorimetry techniques for *in-situ* measurement of the battery heat generation and its corresponding temperature [85, 97]. An alternative approach is to approximate the heat generation rate in a battery from its electrical performance, and solve the energy balance equation

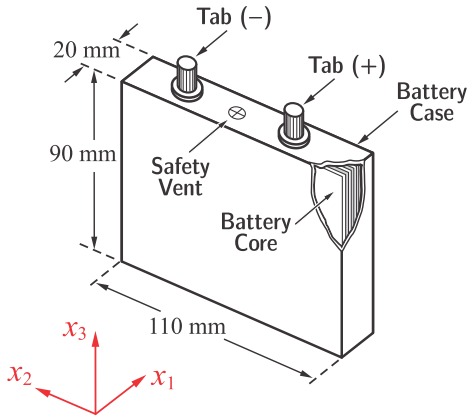

Figure 4.7: Schematic and dimensions of the sample 30 Ah NiMH battery.

for temperature [98]. In this study, the latter approach is employed to investigate thermal response of a NiMH battery during rapid-charging processes.

To the author's best knowledge, multi-dimensional thermal models for NiMH batteries are all based on numerical approaches and are mostly adapted for cylindrical cells. Therefore, the lack of a theoretical distributed model is apparent in the literature.

4.4.1 Structure and thermophysical properties of the sample NiMH battery

We consider a 30 Ah prismatic NiMH cell (NEXcell battery, USA), for which experimental and numerical temperature data during rapid-charging processes are reported in Ref. [99]. As shown in Fig. 4.7, the dimensions of the battery are $20 \times 110 \times 90$ mm. In our analysis, we divide the battery into two regions: the core region, and the case region. The battery core ($L_1 \times L_2 \times L_3 = 19 \times 109 \times 89$ mm), includes a plurality of positive nickel electrodes, negative metal hydride electrodes, and nylon separator sheets. All components of the battery core are encased in a stainless steel container, i.e., the case region, with the thickness of 0.5 mm. The electrodes that accommodate active materials and the separator sheets that serve as ion-exchange membranes have porous structures, and their pores are filled with a concentrated KOH solution as the electrolyte. For the considered battery, the total thickness, porosity, and thermal conductivity of battery layers and electrolyte liquid are listed in Table 4.2, borrowed from Ref. [99]. To evaluate thermal conductivities of porous electrodes and separators, it is assumed that their pores are fully filled with the electrolyte liquid, and their thermal

Table 4.2: Total thickness, porosity, and thermal conductivity of battery components [99].

Material/Layer	Thickness (total) δ [mm]	Porosity ε	Thermal conductivity κ [$\mathrm{W\,m^{-1}\,K^{-1}}$]
Negative electrode	5.40	0.27	1.16
Positive electrode	7.37	0.22	1.14
Separator sheet	6.23	0.74	0.22
Electrolyte	-	-	0.57
Case	0.50	-	16

conductivities are approximated as [100],

$$\kappa = \kappa_{\mathrm{s}}\,(1-\varepsilon) + \kappa_{\mathrm{f}}\,\varepsilon, \tag{4.28}$$

where ε is the porosity of each layer, listed in Table 4.2. The subscripts 's' and 'f' correspond to solid structural materials (electrodes and separators), and liquid filler (electrolyte), respectively.

The concept of equivalent thermal resistance network discussed in Section 4.3.1 is employed to define effective thermal conductivities for the whole battery core. Therefore, by using the data from Table 4.2 and Eqs. (4.23a) and (4.23b), through-plane and in-plane orthotropic conductivities of the battery are 0.74 [$\mathrm{W\,m^{-1}\,K^{-1}}$] and 0.84 [$\mathrm{W\,m^{-1}\,K^{-1}}$], respectively.

Accordingly, evaluated orthotropic thermal conductivities, κ_i, density, ρ, and specific heat, c_p, are listed in Table 4.3.

Table 4.3: Thermophysical properties and the entropic heat generation coefficient for the battery core [99].

Parameter	κ_1 [$\mathrm{W\,m^{-1}\,K^{-1}}$]	κ_2 [$\mathrm{W\,m^{-1}\,K^{-1}}$]	κ_3 [$\mathrm{W\,m^{-1}\,K^{-1}}$]	ρ [$\mathrm{kg\,m^{-3}}$]	c_p [$\mathrm{J\,kg^{-1}\,K^{-1}}$]	$T\,(dV_{\mathrm{oc}}/dT)$ [V]
Values	0.74	0.84	0.84	3520	3200	0.023

4.4.2 Heat generation approximation during fast charging process

In this section, we discuss how to estimate the amount of heat generated during fast-charging process of NiMH battery according to Eq. (4.4).

During the charging process of a NiMH battery, both primary charging reactions (main redox reactions) and side reactions occur inside the battery. The main charging reactions in the positive (nickel) and negative (metal hydride) electrodes are,

- Primary reactions:

$$\text{Negative} \quad : \quad \mathrm{H_2O + M + e^- \rightarrow OH^- + MH} \tag{4.29a}$$

$$\text{Positive} \quad : \quad \mathrm{Ni(OH)_2 + OH^- \rightarrow NiO(OH) + H_2O + e^-} \tag{4.29b}$$

- Side reactions:

$$\text{Negative} \quad : \quad \frac{1}{2}\mathrm{O_2 + H_2O + 2e^- \rightarrow 2OH^-} \tag{4.30a}$$

$$\text{Positive} \quad : \quad \mathrm{2OH^- \rightarrow} \frac{1}{2}\mathrm{O_2 + H_2O + 2e^-} \tag{4.30b}$$

At low values of SOC, the primary charging reaction is dominant at the negative electrode and the rate of oxygen evolution is suppressed. However, at high values of SOC, particularly during the overcharge period, oxygen gas evolves at higher rates since at high potentials the aqueous electrolyte is thermodynamically unstable. This leads to higher rates of internal oxygen cycle reaction, and consequently, the open-circuit voltage decreases to zero [96]. At high SOC, the heat generation rate increases rapidly owing to the oxygen recombination heat at the positive electrode.

To account for the effects of side reactions in battery heat generation, the total charging current, I, is split into the current of charging reaction, I, and the current of internal oxygen cycle reaction (side reactions), I_2. The linear current splitting scheme that is used in our analysis, for which side reactions initiate at SOC=75%, is shown in Fig. 4.8. For for the considered NiMH battery, Eq. (4.4) becomes,

$$\dot{g} = \frac{1}{\mathscr{V}}\left(IV - I_1 V_{\mathrm{oc}} + I_2 T \frac{dV_{\mathrm{oc}}}{dT}\right), \tag{4.31}$$

where $I = I_1 + I_2$.

The SOC corresponding to the onset of side reactions is a battery characteristic. For example, in some cylindrical NiMH batteries, side reactions start at SOC $> 90\%$. Such a battery will be introduced in next chapter, and these effects are more pronounced when the batteries are overcharged [97, 98]. Adiabatic calorimetry of the battery during a constant current charging process allows the rate of heat generation inside the battery to be related to its temperature rise. When battery temperature increases, the chamber of an accelerating rate calorimeter (ARC) can follow the temperature of the battery. Thus, no heat exchange happens between the battery and the chamber, and all the heat generated inside the battery will be used for its temperature rise, i.e.,

$$\dot{g} = \frac{I}{\mathscr{V}}\left[(V - V_{\mathrm{oc}}) + T\frac{dV_{\mathrm{oc}}}{dT}\right] = \rho c_p \frac{dT}{dt}, \tag{4.32}$$

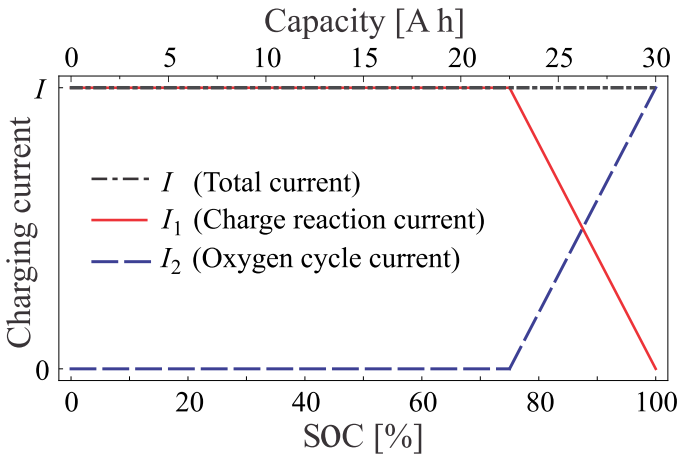

Figure 4.8: Schematic of the linear current splitting model in NiMH batteries [99]. When battery's state-of-charge (SOC) exceeds 75%, side reactions occur. The total current of the battery, I, is summation of the main charging reaction current, I_1, and the oxygen cycling current, I_2.

as long as SOC $< 75\%$.

By replacing $V - V_{\rm oc} = I R_z$, the following relation can be obtained [101],

$$\frac{R_z}{m c_p} I + \frac{T}{m c_p} \frac{dV_{\rm oc}}{dT} = \frac{1}{I} \frac{dT}{dt}, \tag{4.33}$$

where R_z is the apparent DC cell resistance. Based on Eq. (4.33), for a given charging current, I, if $(1/I)\,(dT/dt)$ is plotted against I, a straight line is obtained with the slope $R_z/m c_p$ and the intercept $(T/m c_p)\,(dV_{\rm oc}/dT)$.

For different charging currents, values of $(1/I)\,(dT/dt)$ for the considered battery are reported in Ref. [99]. Since the mass of battery is known, the values for c_p and $T\,(dV_{\rm oc}/dT)$ are obtained, as listed in Table 4.3. Note that from the calorimetry measurement, the total heat capacity of the battery (core and case) is evaluated as 2788 [J kg^{-1} K^{-1}], but the heat capacity of the core will be used in our calculations, which is approximated as $c_p = 3200$ [J kg^{-1} K^{-1}].

4.4.3 Results and discussions

Prior to adapting the theoretical solution proposed in Eq. (4.12), the $\bar{\dot{G}}$ and Δ_{lmn} defined in Eq. (5.29) should be tailored for NiMH battery based on Eq. (4.31);

$$\dot{G} = \dot{G}_{\rm irrev} + \dot{G}_{\rm rev}, \tag{4.34a}$$

with,

$$\dot{G}_{\text{irrev}} = \frac{1/\mathscr{V}}{\kappa_1/L_1^2}\left(IV - I_1 V_{\text{oc}}\right), \qquad \dot{G}_{\text{rev}} = \frac{1/\mathscr{V}}{\kappa_1/L_1^2}\left(0.023\, I_2\right). \tag{4.34b}$$

and

$$\Delta_{lmn} = \lambda_{1l}^2 + K_2\lambda_{2m}^2 + K_3\lambda_{3n}^2. \tag{4.34c}$$

During battery operation, both $\dot{G}_{\text{irrev}}$ and $\dot{G}_{\text{rev}}$ vary with SOC (or time), since I_1, I_2, V and V_{oc} are functions of SOC (or time). The charge reaction current, I_1, contributes only to the irreversible heat, while the oxygen cycle current, I_2, contributes to both reversible and irreversible heats.

4.4.4 Model validation with numerical data

The voltage response of the considered NiMH battery during charging processes at 15 A and 20 A are reported in Ref. [99]; shown by symbols in Fig. 4.9. For each constant-current charging process, polynomials are fitted to the measured values; shown with lines in Fig. 4.9, and these polynomials are used to evaluate $\dot{g}$ from Eq. (4.31), see Fig. 4.10. The linear transformation in (4.34a) is used to relate the magnitude of $\dot{g}$ to $\dot{G}$, which in our case is $\dot{g} = 2050\,\dot{G}$. Due to splitting of the current into charge reaction current and oxygen cycle current [cf. Fig. 4.8], the rate of heat generation turns out to be a noncontinuous function; shown as solid lines in Fig. 4.10. In order to facilitate the computations, $\dot{G}$ and $\dot{g}$, are approximated with ninth-order polynomials; shown as dashed lines in Fig. 4.10. The sharp increase in heat generation for SOC $> 75\%$ corresponds to the oxygen cycle reaction. Experimental investigations [85, 97] confirm such a behavior in NiMH batteries. Variations of the maximum temperature, $T_{\max}$, at the center of the battery $\xi = (0.5, 0.5, 0.5)$ and the minimum temperature, $T_{\min}$, at the corner of the battery $\xi = (0, 0, 0)$ as a function of SOC are shown in Fig. 4.11. We assume convective heat transfer at all surfaces of the battery case, with small and moderate heat transfer coefficients, $h_{ij,\text{case}} = \{6, 25\}$, to present cooling effects of natural- and forced-convection with air. Both ambient and initial temperatures are set to $T_0 = 23^{\circ}\text{C}$. The temperatures $T_{\max}$ and $T_{\min}$ calculated numerically with a finite element solver (COMSOL Multiphysics, Version 4.2a), shown with symbols, are used to validate the results from the proposed analytical model, shown with lines. In the numerical calculation, the relative tolerance was set to 10^{-6}. Figures 4.11a and 4.11b correspond to the battery thermal response at 15 A charging, whereas Figs. 4.11c and 4.11d represent the same information for a 20 A charging current. Two sets of analytical results are shown for $T_{\max}$ and $T_{\min}$. The dashed lines denote analytical solution with the first

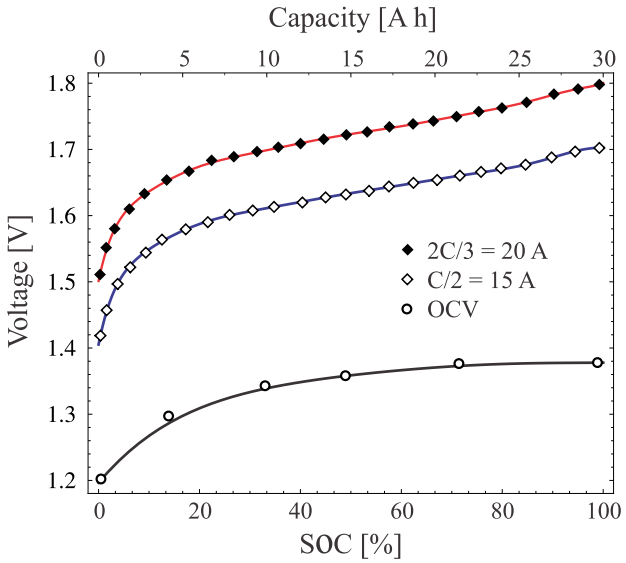

Figure 4.9: Variations of the battery voltage versus SOC are shown during charging processes. Symbols indicate experimental data [99] for open-circuit voltage (circles), 15 A charging current (white diamonds), and 20 A charging current (black diamonds). Solid lines represent sixth-order polynomial fits to the experimental data.

eigenvalue in each direction only, i.e., the first term approximation, and the solid lines present series solutions with multiple eigenvalues. The comparisons show a fair agreement between the analytical and numerical results, and as expected, increase in the number of eigenvalues increases the accuracy of analytical solutions at a higher computational cost.

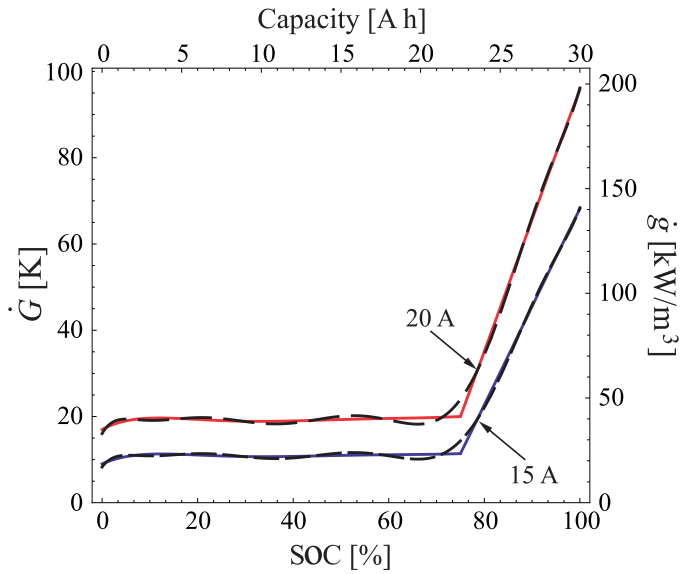

Figure 4.10: Variations of heat generation rate, $\dot{g}$, and the source for temperature rise. $\dot{G}$, versus SOC are shown for 15 A and 20 A charging currents. Dashed lines represent ninth-order fitting polynomials.

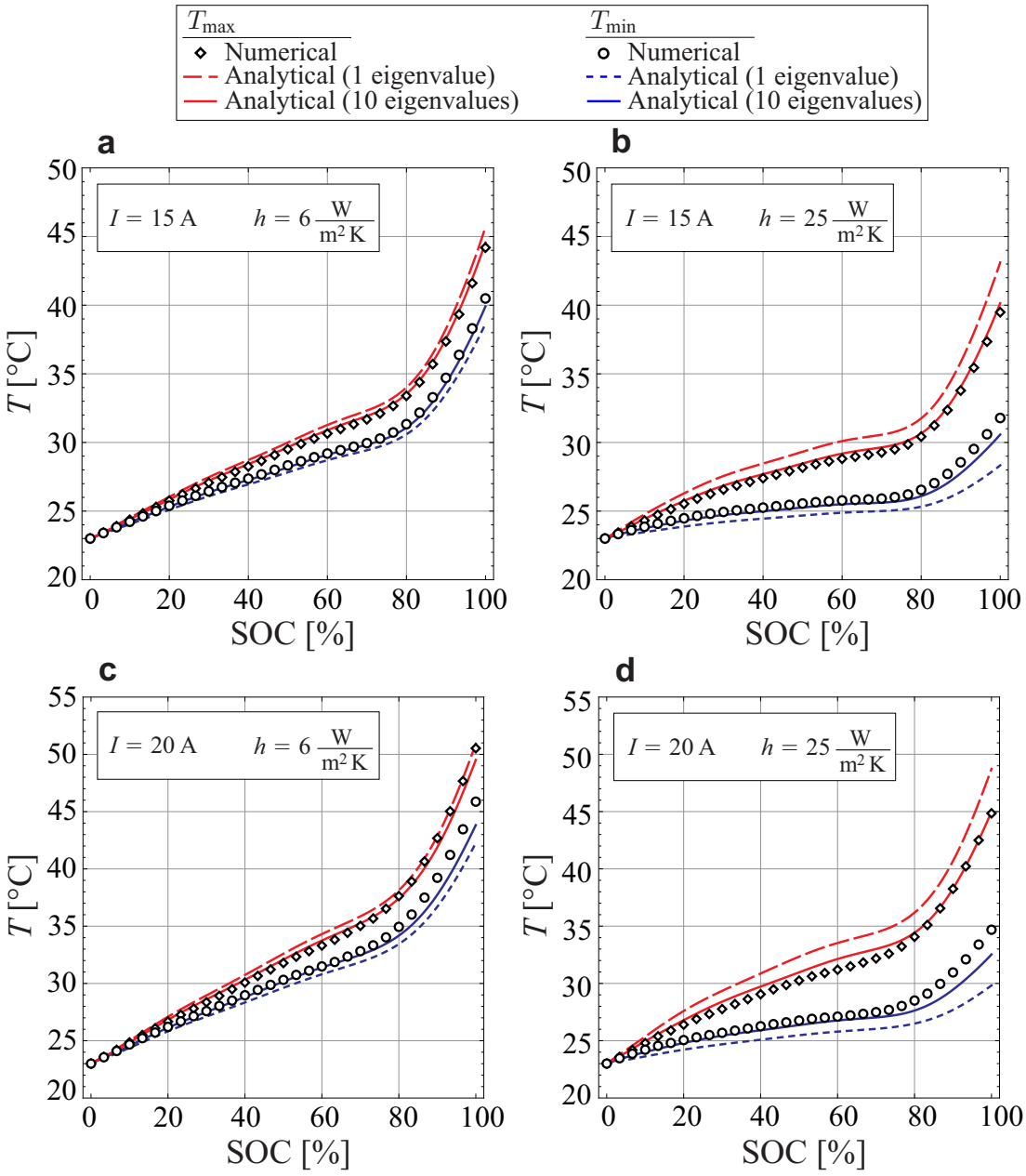

Figure 4.11: Temperature variation versus SOC is shown for 15 A charging current (plots a and b) and 20 A charging current (plots c and d). Maximum temperature at the battery center and minimum temperature at the battery corner for $h_{ij,\text{case}} = \{6, 25\}$ W m^{-2} K^{-1} are compared to numerical data (symbols). Analytical results with first term approximation (dashed lines) and series solution (solid lines) are shown.

4.4.5 Model validation with experimental data

Figure 4.12 compares the calculated (analytical and numerical) and measured temperature profiles along the centerline of the battery core, along x_1 and x_3 direction, for different charging times with a 15 A charging current under natural convection cooling, $h_{ij} = 6\ \mathrm{W\,m^{-2}\,K^{-1}}$. The experimental temperature data, borrowed from Ref. [99], was measured by K-type thermocouples with an accuracy of $\pm 1.5°\mathrm{C}$. The comparisons show that the analytical solution with the first term approximation is not very accurate, particularly towards the end of the charging process, i.e., $t = 114$ min. However, an excellent agreement between the analytical and the numerical results can be obtained when multiple eigenvalues (series solution) are used. Indeed, our calculations confirm that for the considered problem, four eigenvalues suffice to obtain an accurate analytical solution, and further increase in the number of eigenvalues will not improve the results significantly. Also, the comparison with experimental data reveals that the current splitting scheme and the corresponding heat generation model [cf. Eq. (4.31)] result in fair temperature predictions in the thermal models.

The inconsistency between the calculated and measured temperature values at the later times of the charging process are related to the dependency of heat generation on the temperature, which is neglected in our calculations, since the term $T\,(dV_{\mathrm{oc}}/dT)$ is assumed as a constant. Instead, when value of dV_{oc}/dT is known, from electro-chemical simulations [95, 96], and T in the formula for heat generation rate [cf. Eq.(4.31)] is treated as a variable, then, a better matching with the experimental is expected.

Furthermore, the temperature distribution inside the battery strongly depends on the thermal conductivities of the core. In our calculations, the thermal conductivity of the porous materials in the battery core were approximated by averaging, as given in Eq. (4.28). In reality, due to the pores distribution and their size, orthotropic thermal conductivities may vary in different locations. This fact must be addressed as another reason for the differences between the measured and calculated temperature values in Fig. 4.12.

4.4.6 Charging efficiency

The fundamental energy balance for the battery states that the total energy, E_{tot}, provided by the charger splits into electrochemical energy, E°, stored inside the battery and thermal energy, E_{th}, which is both consumed to increase the battery temperature, and dissipated to the surrounding via

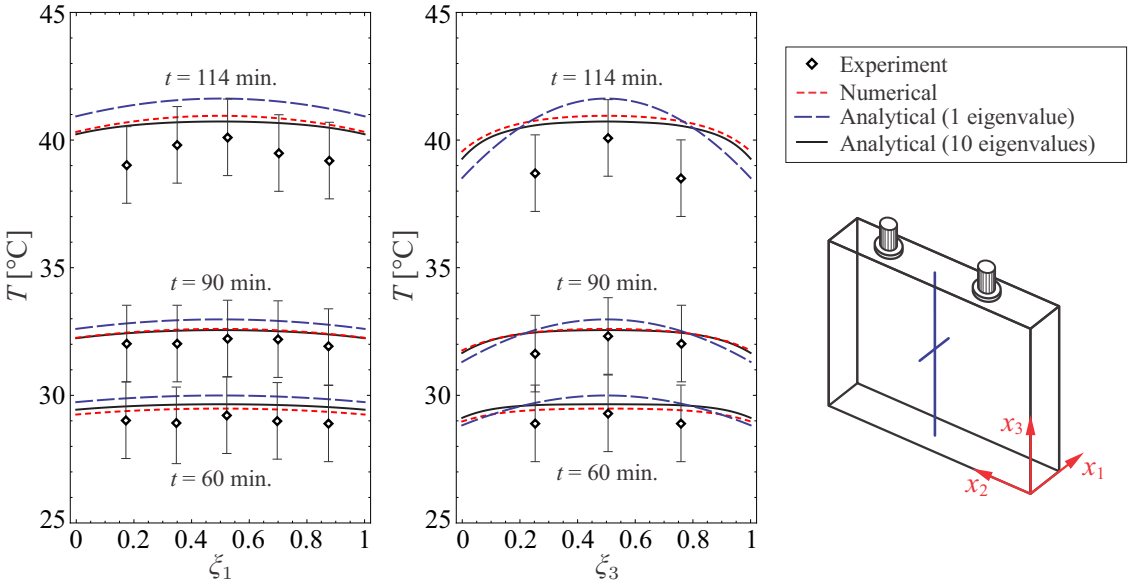

Figure 4.12: Calculated temperature profiles at centerlines of the battery core are compared to experimental temperature measurements (symbols) [99]. Numerical results are shown with dashed lines (red) whereas analytical temperature distributions are denoted by long-dashed lines (blue) for first term approximation and solid lines (black) for series solution. Temperature distributions are shown at different times during a charging process at 15 A, subjected to a natural convection cooling, $h_{ij,\text{case}} = 6\ \text{W m}^{-2}\,\text{K}^{-1}$ at all surfaces of the battery. Ambient and initial temperature of 23°C was assumed.

convection heat transfer. Accordingly, a charging efficiency, η, can be defined for the battery,

$$\eta = \frac{E^\circ}{E_{\text{tot}}} = 1 - \frac{E_{\text{th}}}{E_{\text{tot}}}, \tag{4.35a}$$

where,

$$E^\circ = E_{\text{tot}} - E_{\text{th}}, \qquad E_{\text{tot}} = I \int_t V(t)\,dt, \qquad E_{\text{th}} = \mathscr{V} \int_t \dot{g}(t)\,dt. \tag{4.35b}$$

Based on Eq. (4.35b), the total energy required for charging the battery at different constant currents can be calculated by integrating the voltage response of the cell, as shown in Fig. 4.9. Similarly, the thermal energy can be calculated by integrating the heat generation rate inside the cell, as shown in Fig. 4.10.

Variation of charging efficiency with respect to SOC is shown in Fig. 4.13. As expected, charging at the higher rate is less efficient as it yields the higher rate of heat generation [cf. Fig. 4.10]. Also, the results show that for the considered battery the charging efficiency drops dramatically for

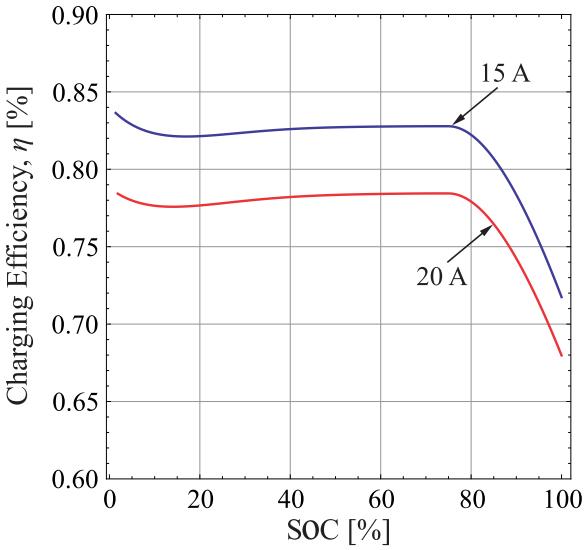

Figure 4.13: Variations of the charging efficiency with respect to charging rate and SOC.

SOC $> 75\,\%$, owing to the initiation of exothermic side reactions. For fast-charging processes at 15 A and 20 A, values of E_{tot}, E_{th}, and E° corresponding to SOC $= 100\%$ are listed in Table 4.4. In both cases, the electrochemical energy, E°, stored inside the battery is constant, which confirms the battery is equally charged in both charging processes. The results in Figs. 4.11 and 4.13 suggest to fast-charge the considered NiMH battery while SOC $< 75\%$, and employ a less aggressive charging profile for the rest of the charging process. This describes why NiMH batteries in hybrid-electric vehicles are preferred to operate in a charge-sustaining mode while the SOC of batteries is maintained below $\sim 75\,\%$.

Table 4.4: Values of total energy, thermal energy, electrochemical energy, and charging efficiency for charging processes at 15 A and 20 A.

Charging current	E_{tot} [J]	E_{th} [J]	E° [J]	η [%]
15 [A]	175 421	49 565	125 856	72
20 [A]	185 141	59 285	125 856	68

4.5 Conclusion

In summary, based on the method of integral-transformation, a closed-form analytical model is developed to describe temperature distribution in batteries with modest numerical effort. The proposed thermal model takes account for:

- multi-dimensional heat conduction,
- orthotropic thermal conductivities,
- time dependent and temperature dependent heat generation terms,

and therefore provide a useful tool for investigating the thermal behavior of batteries in various operating conditions.

The proposed model was employed to study the temperature rise in a pouch-type Li-ion cell during discharge processes, where transient heat generation rate was approximated from the electrical performance of the battery. The accuracy of the model was confirmed through comparison with the numerical data.

The results showed that for the considered battery, natural convection can prevent battery overheating during low and moderate discharge processes, when a room temperature (25 °C) was considered as the initial and ambient temperatures. For more aggressive discharge conditions, higher heat transfer rates at battery surface are required, e.g., forced-convection or liquid cooling. Certain conditions, under which a two-dimensional thermal analysis is applicable, are highlighted through definition of a surface-averaged Biot number. To demonstrate the versatility of the proposed analytical thermal model, the model was adapted to describe the evolution of the temperature field inside the core of prismatic NiMH battery during fast-charging processes with constant currents.

The proposed thermal model was alos employed to approximate the thermal response of a 30 A h NiMH cell during fast-charging processes at C/2-rate (15 A) and 2C/3-rate (20 A), where transient heat generation rates were approximated from the electrical performance of the battery.

The accuracy of the model was confirmed through comparison with both numerical and experimental data; thus, it can be considered as a robust tool for investigating the thermal behavior of batteries in various operating conditions.

The thermal model is used to define a new charging efficiency for batteries, i.e., the ratio of electrochemical energy stored inside the battery to the total energy used for charging the battery, which is an index for describing the percentage of energy wasted as heat.

Chapter 5

A Computationally-Effective Thermal Model for Spirally Wound Nickel-Metal Hydride Batteries

To demonstrate the versatility of the proposed analytical solution detailed in Chapter 2, a two-dimensional analytical model is developed to investigate the transient thermal behaviour of spirally wound batteries. To validate the model, the model is adapted to study the transient thermal behaviour of a cylindrical NiMH battery for which experimental data is available in the literature [98].

To the author best knowledge, multi-dimensional thermal models for cylindrical batteries are all based on numerical approaches [42, 97, 98, 102–108] and lack of a theoretical distributed model is apparent in the literature. To date, the only available analytical thermal model is Mahmud *et al*. [109] study, where a spatial-resolution lumped-capacitance model is formulated under high Biot number conditions and for model validation, a one-dimensional (radial direction), transient analytical solution is developed.

5.1 Model development

A 8 Ah cylindrical NiMH battery is considered to demonstrate the modeling steps and validate the results. For the considered battery, experimental data during rapid-charging processes with overcharging periods are reported in Ref. [98].

As illustrated in Fig. 5.1a, the radius and height of the battery are 16.5 mm and 61 mm, respectively. In the analysis we divide the battery into two regions: the core region, and the case region (can). The battery core ($R \times L = 16 \times 60$ mm), shown in Fig. 5.1b, includes a positive nickel electrodes, a negative metal hydride electrode, and a polypropylene separator sheet. All components of the core are porous and their pores are filled with a concentrated KOH solution (30 wt%) which acts as the electrolyte. At the positive and negative electrodes, $\beta-\mathrm{Ni(OH)_2}$ and $\mathrm{Mm\,Ni_{3.75}\,Co_{0.55}\,Al_{0.3}\,Mn_{0.4}}$ are used as active materials, respectively. All components of the battery core are spirally wound and packaged in a stainless steel container, i.e., the case region, with the thickness of 0.5 mm. Values of volume fraction, porosity, and thermal conductivity for the battery

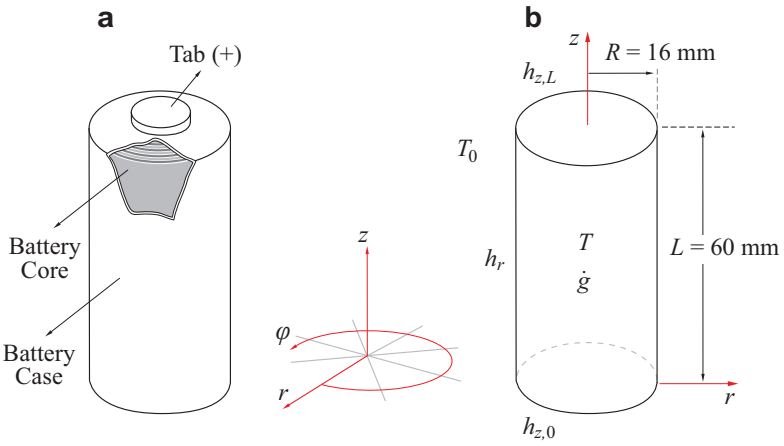

Figure 5.1: (a) Multi-layered structure of a cylindrical NiMH battery, (b) Two-dimensional schematic of the battery core in r-z plane with internal heat generation, $\dot{g}$, and convective heat dissipation at boundaries.

components are listed in Table 5.1, borrowed from Ref. [98]. The values of thermal conductivity for

Table 5.1: Volume fraction, porosity, and thermal conductivity of battery components [98].

Material/Layer	Volume fraction of battery core ν [%]	Porosity ε	Thermal conductivity k [W m^{-1} K^{-1}]
Porous negative electrode	29	0.25	1.16
Porous positive electrode	45	0.30	1.14
Porous separator sheet	27	0.74	0.22
Electrolyte	–	–	0.57
Case	–	–	16

dry electrodes and dry separator are given in Table 5.1. The thermal conductivities of the wet electrodes and separator, assuming the pores are fully filled with the electrolyte liquid, are approximated from Eq. (4.28)

As in the previous chapter, to avoid complexities associated with heat transfer in multi-layered structure of the battery core, the concept of equivalent thermal resistance network is employed to define effective thermal conductivities for the battery. Based on Fig. 5.1a, there are series thermal resistors in r-direction and parallel thermal resistors in z-directions. Therefore, by using the data from Table 5.1, through-plane (r-direction) and in-plane (z-direction) thermal conductivities can be evaluated as [98],

$$k_r = \left(\sum_i \frac{\nu_i}{k_i} \right)^{-1} = \left(\frac{\nu_\mathrm{p}}{k_\mathrm{p}} + \frac{\nu_\mathrm{s}}{k_\mathrm{s}} + \frac{\nu_\mathrm{n}}{k_\mathrm{n}} \right)^{-1} = 0.74 \, [\mathrm{W\,m^{-1}\,K^{-1}}] \tag{5.1a}$$

and

$$k_z = \sum_i \nu_i k_i = \nu_\mathrm{p} k_\mathrm{p} + \nu_\mathrm{s} k_\mathrm{s} + \nu_\mathrm{n} k_\mathrm{n} = 0.85 \, [\mathrm{W\,m^{-1}\,K^{-1}}] \tag{5.1b}$$

where ν_p, ν_s, and ν_n represent the volume fraction of the positive electrode, separator, and negative electrode, respectively. The thermal conductivity of positive electrode, k_p, negative electrode, k_n, and separator, k_s, in the presence of electrolyte liquid are obtained from Eq. (4.28).

By assuming that temperature has no variation in azimuthal direction (φ-direction), the transient temperature field inside the battery core can be described by the energy balance equation in cylindrical coordinates [98, 102, 106],

$$\rho c_p \frac{\partial T}{\partial t} = k_z \frac{\partial^2 T}{\partial z^2} + k_r \frac{1}{r} \frac{\partial}{\partial r} \left(r \frac{\partial T}{\partial r} \right) + \dot{g} \tag{5.2}$$

in which t is the time, while r and z represent the components of the position vector in cylindrical coordinate system. The functions $T(r,z,t)$ and $\dot{g}(r,z,t)$ denote the temperature field and volumetric heat generation rate inside the battery core, respectively (Fig. 5.1b). The density, ρ, specific heat, c_p, and orthotropic thermal conductivities, k_r and k_z, [cf. Eq. (5.1)], are the thermophysical parameters for the core region, for which the values are listed in Table 5.2.

Table 5.2: Thermophysical properties, entropic heat generation coefficients, and apparent DC resistance for the battery core [98].

Parameter	k_r [$\mathrm{W\,m^{-1}\,K^{-1}}$]	k_z [$\mathrm{W\,m^{-1}\,K^{-1}}$]	ρ [$\mathrm{kg\,m^{-3}}$]	c_p [$\mathrm{J\,kg^{-1}\,K^{-1}}$]	$dV_{\mathrm{oc,p}}/dT$ [$\mathrm{V\,K^{-1}}$]	$dV_{\mathrm{oc,n}}/dT$ [$\mathrm{V\,K^{-1}}$]	R_d [mΩ]
Values	0.74	0.85	3900	1882	-1.0×10^{-3}	-6.3×10^{-4}	3

Convective thermal boundary conditions at surfaces of the battery case are applied. Accordingly, boundary conditions for the battery core are,

$$-k_z \frac{\partial T}{\partial z} = \left[\frac{1}{h_{z,0}} + \frac{l_c}{k_c}\right]^{-1} (T - T_0) \quad \text{at} \quad z = 0 \tag{5.3a}$$

$$+k_z \frac{\partial T}{\partial z} = \left[\frac{1}{h_{z,L}} + \frac{l_c}{k_c}\right]^{-1} (T - T_0) \quad \text{at} \quad z = L \tag{5.3b}$$

$$-k_r \frac{\partial T}{\partial r} = 0 \quad \text{at} \quad r = 0 \tag{5.3c}$$

$$+k_r \frac{\partial T}{\partial r} = \left[\frac{1}{h_r} + \frac{l_c}{k_c}\right]^{-1} (T - T_0) \quad \text{at} \quad r = R \tag{5.3d}$$

where l_c and k_c denote the thickness and the thermal conductivity of the battery case, respectively. The environment temperature is represented by T_0. The convective heat transfer coefficients at the bottom, top, and lateral surface of the battery are denoted by $h_{z,0}$, $h_{z,L}$, and h_r, respectively.

The initial temperature of the battery is assumed the same as the environment temperature, T_0;

$$T = T_0 \quad \text{at} \quad t = 0 \tag{5.4}$$

As mentioned in Section 4.4, during regular charging, the primary charging reactions are dominant at the electrodes, and the overall reaction is,

$$\mathrm{Ni(OH)_2 + M \rightarrow NiO(OH) + MH} \qquad -14.65\,[\mathrm{kJ\,mol^{-1}}] \tag{5.5}$$

while during overcharging, the side reactions become dominant, i.e., the oxygen generated at the positive electrode reacts with hydrogen at the negative electrode to form water [cf. Eq. (5.6)] and release plenty of enthalpy reaction [110].

$$\mathrm{2H + \frac{1}{2}O_2 \rightarrow H_2O} \qquad -285.9\,[\mathrm{kJ\,mol^{-1}}] \tag{5.6}$$

Since heat generation rate in regular charging and overcharging processes are different, as discussed in Section 4.4.2, we calculate them differently with the following formulas [45, 98];

$$\dot{g} = \begin{cases} \dfrac{I}{\mathscr{V}} \left(V - V_{\mathrm{oc}} + T \dfrac{dV_{\mathrm{oc}}}{dT} \right) & \text{regular charging} \\ \\ \dfrac{1}{\mathscr{V}} \left(R_d I^2 + nF\Delta H \right) & \text{overcharging} \end{cases} \tag{5.7}$$

The constants $R_d = 3\,\mathrm{m\Omega}$ (see Table 5.2), $n = 0.5$, $F = 96487\,\mathrm{A\,s/mol}$, and $\Delta H = 285.9\,\mathrm{kJ/mol}$ respectively denote apparent DC resistance of the battery, electric charge number, the Faraday constant, and enthalpy of the recombination reaction [cf. Eq. (5.6)], respectively [98, 111].

During regular charging, the heat generation consists of irreversible heat $I(V-V_{\mathrm{oc}})/\mathscr{V}$ due to polarization and ohmic potential loss, reversible heat $IT\left(dV_{\mathrm{oc}}/dT\right)/\mathscr{V}$ due to the entropy change in electrochemical reactions. During overcharging period, the heat generation involves Joule heating $R_d I^2/\mathscr{V}$, and recombination reaction heat $nF\,\Delta H/\mathscr{V}$.

The battery temperature coefficient (entropic heat generation coefficient) dV_{oc}/dT can be presented as [98],

$$\frac{dV_{\mathrm{oc}}}{dT}=\frac{dV_{\mathrm{oc,p}}}{dT}-\frac{dV_{\mathrm{oc,n}}}{dT} \tag{5.8}$$

where the first term on the right hand-side represents the temperature coefficient of the positive electrode and the second term denotes the temperature coefficient of the negative electrode; values are listed in Table 5.2.

5.2 Analytical solution

To simplify the initial-boundary-value problem [cf. Eqs. (5.2)–(5.4)] and the corresponding auxiliary equations [cf. Eqs. (5.7) and (5.8)], we define a new variable,

$$\theta=T-T_0 \quad \text{thus} \quad d\theta=dT \tag{5.9}$$

and rewrite the governing equations in terms of new variable. This gives,

$$\rho c_p\frac{\partial\theta}{\partial t}=k_z\frac{\partial^2\theta}{\partial z^2}+k_r\frac{1}{r}\frac{\partial}{\partial r}\left(r\frac{\partial\theta}{\partial r}\right)+\dot{g} \tag{5.10a}$$

with

$$\dot{g}=\begin{cases}\dfrac{I}{\mathscr{V}}\left[V-V_{\mathrm{oc}}+(\theta+T_0)\dfrac{dV_{\mathrm{oc}}}{d\theta}\right] & \text{regular charging}\\[2ex] \dfrac{1}{\mathscr{V}}\left(R_dI^2+nF\,\Delta H\right) & \text{overcharging}\end{cases} \tag{5.10b}$$

for which the boundary conditions are,

$$-k_z\frac{\partial\theta}{\partial z}=\left[\frac{1}{h_{z,0}}+\frac{l_{\mathrm{c}}}{k_{\mathrm{c}}}\right]^{-1}\theta \quad \text{at} \quad z=0 \tag{5.11a}$$

$$+k_z\frac{\partial\theta}{\partial z}=\left[\frac{1}{h_{z,L}}+\frac{l_{\mathrm{c}}}{k_{\mathrm{c}}}\right]^{-1}\theta \quad \text{at} \quad z=L \tag{5.11b}$$

$$-k_r\frac{\partial\theta}{\partial r}=0 \quad \text{at} \quad r=0 \tag{5.11c}$$

$$+k_r\frac{\partial\theta}{\partial r}=\left[\frac{1}{h_r}+\frac{l_{\mathrm{c}}}{k_{\mathrm{c}}}\right]^{-1}\theta \quad \text{at} \quad r=R \tag{5.11d}$$

and the initial condition is;

$$\theta = 0 \quad \text{at} \quad t = 0 \tag{5.12}$$

Equation (5.10) describes the temperature rise, θ, inside the battery core with respect to the space and time, and is solved analytically using the method of integral-transformation, as demonstrated in the previous chapter. In this part, we aim to modify the solution introduced in Chapter 2, apply it to cylindrical-shaped batteries. The integral-transform technique removes the spatial dependency from the differential equation of heat conduction. In the Cartesian coordinate system, this integral-transform is called the Fourier transform, and in the cylindrical coordinate system it is called the Hankel transform [73].

5.2.1 Fourier transformation

The Fourier transform and the inversion formula for the temperature function $\theta(r,z,t)$ with respect to $z \in \{0,L\}$ are defined as [73];

$$\text{Transformation}: \quad \bar{\theta}(r,\alpha_n,t) = \int_0^L \Phi\left(\alpha_n,z'\right)\theta\left(r,z',t\right)dz' \tag{5.13a}$$

$$\text{Inversion}: \quad \theta(r,z,t) = \sum_{n=1}^{\infty} \Phi(\alpha_n,z)\,\bar{\theta}(r,\alpha_n,t) \tag{5.13b}$$

The function $\Phi(\alpha_n,z)$ is the transformation kernel (normalized eigenfunction) in z-direction,

$$\Phi(\alpha_n,z) = \frac{\phi(\alpha_n,z)}{\sqrt{N_z}} \tag{5.14}$$

and $\phi(\alpha_n,z)$ is the eigenfunction;

$$\phi(\alpha_n,z) = \alpha_n\cos(\alpha_n z) + H_{z,0}\sin(\alpha_n z) \tag{5.15}$$

The eigenfunction is solution of the following Sturm–Liouville system corresponding to Eqs. (5.10a), (5.11a), and (5.11b),

$$\frac{d^2\phi}{dz^2} + \alpha_n^2\phi = 0 \tag{5.16a}$$

$$-\frac{d\phi}{dz} + H_{z,0}\phi = 0 \quad \text{at} \quad z = 0 \tag{5.16b}$$

$$+\frac{d\phi}{dz} + H_{z,L}\phi = 0 \quad \text{at} \quad z = L \tag{5.16c}$$

where $H_{z,0} = h_{z,0}/k_z$ and $H_{z,L} = h_{z,L}/k_z$. In Eqs. (5.13)–(5.16), α_n indicates the n-th eigenvalue in z-direction. The eigenvalues are positive roots (infinite) of the following transcendental equation

[73];

$$\tan(L\alpha_n) = \frac{\alpha_n (H_{z,0} + H_{z,L})}{\alpha_n^2 - H_{z,0} H_{z,L}} \tag{5.17}$$

Eigenvalues normalization factor, N_z, which appears in Eq. (5.14) is obtained as [73];

$$N_z = \frac{1}{2}\left[\frac{H_{z,0}}{\alpha_n^2} + \frac{\alpha_n^2 + H_{z,0}^2}{\alpha_n^2}\left(L + \frac{H_{z,L}}{\alpha_n^2 + H_{z,L}^2}\right)\right] \tag{5.18}$$

The integral-transform of the initial-boundary-value problem [cf. Eqs. (5.10)–(5.12)], according to transformation (5.13a), yields the following PDE for $\bar{\theta}$;

$$\rho c_p \frac{\partial \bar{\theta}}{\partial t} = -k_z \alpha_n^2 \bar{\theta} + k_r \frac{1}{r}\frac{\partial}{\partial r}\left(r \frac{\partial \bar{\theta}}{\partial r}\right) + \bar{g} \tag{5.19a}$$

with

$$\bar{g} = \begin{cases} \dfrac{I}{\mathscr{V}} \displaystyle\int_0^L \Phi(\alpha_n, z)\left(V - V_{\text{oc}} + T_0 \frac{dV_{\text{oc}}}{d\theta}\right) dz + \frac{I}{\mathscr{V}} \bar{\theta} \frac{dV_{\text{oc}}}{d\theta} & \text{regular charging} \\ \dfrac{1}{\mathscr{V}} \displaystyle\int_0^L \Phi(\alpha_n, z)\left(R_d I^2 + nF\Delta H\right) dz & \text{overcharging} \end{cases} \tag{5.19b}$$

The transformed boundary conditions are,

$$-k_r \frac{\partial \bar{\theta}}{\partial r} = 0, \qquad \text{at} \quad r = 0 \tag{5.20a}$$

$$+k_r \frac{\partial \bar{\theta}}{\partial r} = \left[\frac{1}{h_r} + \frac{l_c}{k_c}\right]^{-1} \bar{\theta}, \quad \text{at} \quad r = R \tag{5.20b}$$

and the transformed initial condition is,

$$\bar{\theta} = 0, \quad \text{at} \quad t = 0 \tag{5.21}$$

where $\bar{\theta} \equiv \bar{\theta}(r, \alpha_n, t)$, and quantities with a bar refer to transformed quantities as given in Eq. (5.13a). Due to the Fourier transformation, in Eq. (5.19) the derivative term with respect to z is transformed to an algebraic term, thus, boundary conditions in z-direction are not required.

5.2.2 Henkel transformation

Equations (5.19)–(5.21) include a differential operator with respect to the radial direction $r \in \{0, R\}$ which can be transformed to algebraic terms by means of Henkel transform. The Henkel transform and its corresponding inversion formula are [73];

$$\text{Transformation}: \qquad \bar{\bar{\theta}}(\beta_m, \alpha_n, t) = \int_0^R r' \Psi(\beta_m, r') \bar{\theta}(r', \alpha_n, t)\, dr' \tag{5.22a}$$

$$\text{Inversion}: \qquad \bar{\theta}(r, \alpha_n, t) = \sum_{m=1}^{\infty} \Psi(\beta_m, r)\, \bar{\bar{\theta}}(\beta_m, \alpha_n, t) \tag{5.22b}$$

Here, the quantities with two bars are transferred by Eq. (5.13a) and Eq. (5.22a); first bar denotes the Fourier transform and the second one Henkel transform.

The function $\Psi(\beta_m, z)$ is the transformation kernel (normalized eigenfunction) in r-direction;

$$\Psi(\beta_m, r) = \frac{\psi(\beta_m, r)}{\sqrt{N_r}} \tag{5.23}$$

and $\psi(\beta_m, r)$ is the eigenfunction,

$$\psi(\beta_m, r) = J_0(\beta_m r) \tag{5.24}$$

The eigenfunction is solution of the following homogenous eigenvalue problem in r-direction [73],

$$\frac{d}{dr}\left(r\frac{d\psi}{dr}\right) + \beta_m^2 r\,\psi = 0 \tag{5.25a}$$

$$-\frac{d\psi}{dr} = 0 \quad \text{at} \quad r = 0 \tag{5.25b}$$

$$+\frac{d\psi}{dr} + H_r\psi = 0 \quad \text{at} \quad r = R \tag{5.25c}$$

in which $H_r = h_r/k_r$. In Eqs. (5.22)–(5.25), β_m denotes the m-th eigenvalue in r-direction. The eigenvalues are positive roots of the following transcendental equation [73],

$$\beta_m \left.\frac{dJ_0(r)}{dr}\right|_{\beta_m R} = -H_r J_0(\beta_m R) \tag{5.26}$$

in which J_0 is the Bessel function of the first kind. Eigenvalues normalization factor N_r [cf. Eq. (5.23)] is evaluated as;

$$N_r = \frac{R^2}{2}\left[1 + \frac{H_r^2}{\beta_m^2}\right] J_0^2(\beta_m R) \tag{5.27}$$

The integral transform of Eqs. (5.19)–(5.21), according to the transformation (5.22a), yields the following ODE for $\bar{\bar{\theta}}$;

$$\rho c_p \frac{d\bar{\bar{\theta}}}{dt} = -\Delta_{m,n}\bar{\bar{\theta}} + \bar{\bar{g}} \tag{5.28a}$$

with

$$\Delta_{m,n} = \begin{cases} k_z\alpha_n^2 + k_r\beta_m^2 + \dfrac{I}{\mathscr{V}}\dfrac{dV_{\text{oc}}}{d\theta} & \text{charging} \\ \\ k_z\alpha_n^2 + k_r\beta_m^2 & \text{overcharging} \end{cases} \tag{5.28b}$$

and

$$\bar{\bar{g}} = \begin{cases} \dfrac{I}{\mathscr{V}}\displaystyle\int_0^R\int_0^L r\,\Psi(\beta_m, r)\,\Phi(\alpha_n, z)\left(V - V_{\text{oc}} + T_0\frac{dV_{\text{oc}}}{d\theta}\right)dz\,dr & \text{regular charging} \\ \\ \dfrac{1}{\mathscr{V}}\displaystyle\int_0^R\int_0^L r\,\Psi(\beta_m, r)\,\Phi(\alpha_n, z)\left(R_d I^2 + nF\,\Delta H\right)dz\,dr & \text{overcharging} \end{cases} \tag{5.28c}$$

The required initial condition for the ODE is,

$$\bar{\bar{\theta}} = 0 \quad \text{at} \quad t = 0 \tag{5.28d}$$

where $\bar{\bar{\theta}} \equiv \bar{\bar{\theta}}\,(\beta_m, \alpha_n, t)$.

5.2.3 Inversion of the transformed temperature function

Using the Fourier and the Henkel transforms, the original PDE of heat conduction [cf. Eq. (5.2)] is converted to an inhomogeneous first-order ODE [cf. Eq. (5.28a)] for the double transformed temperature function $\bar{\bar{\theta}}\,(\beta_m, \alpha_n, t)$, subject to a prescribed initial condition as given by Eq. (5.28d). An exact solution for Eq. (5.28a) is straightforward to be obtained, that is,

$$\bar{\bar{\theta}}\,(\lambda_m, \lambda_n, t) = \exp\left(-\frac{\Delta_{m,n}}{\rho c_p}\, t\right)\left[\int_t \frac{\bar{\bar{g}}\,(t)}{\rho c_p} \exp\left(\frac{\Delta_{m,n}}{\rho c_p}\, t\right) dt + \mathscr{C}\right] \tag{5.29}$$

for which the corresponding integrating constant, $\mathscr{C}$, must be evaluated from the given initial condition, $\bar{\bar{\theta}}\,(\beta_m, \alpha_n, 0) = 0$.

When the above solution is inverted successively by means of inversion formulas, i.e., Eqs. (5.13b) and (5.22b), a series form solution for the original problem can be obtained as;

$$\theta\,(r, z, t) = \sum_{m=1}^{\infty} \sum_{n=1}^{\infty} \Psi\,(\beta_m, r)\, \Phi\,(\alpha_n, z)\, \bar{\bar{\theta}}\,(\beta_m, \alpha_n, t) \tag{5.30}$$

5.3 Results and discussions

In this section, the thermal behavior of the sample NiMH battery during fast-charging process is investigated by the proposed analytical approach. The required calculations, as explained in section 5.2, are programmed symbolically in Mathematica 9.0© [112] to obtain a generic solution for temperature field inside the battery core. Solutions for the temperature distribution inside the battery, as given in Eq. (6.34), are obtained and compared to the experimental data from Ref. [98], and numerical results.

5.3.1 Model validation with experimental data

The voltage response of the considered NiMH battery during charging processes at 8 A, 18 A, and 32 A is reported in Ref. [98], and shown with symbols in Fig. 5.2. Note that, since the capacity

of the battery is 8 Ah, the charging time at 8 A, 16 A, and 32 A correspond to 3600, 1800, and 900 seconds, respectively. A sixth-order polynomial is fitted to each constant current charging process as presented with lines in Fig. 5.2. These polynomials are used to evaluate the irreversible heat generation $I(V - V_{oc})/\mathscr{V}$ term, in Eq. (5.7). Figure 5.3 compares the measured surface average

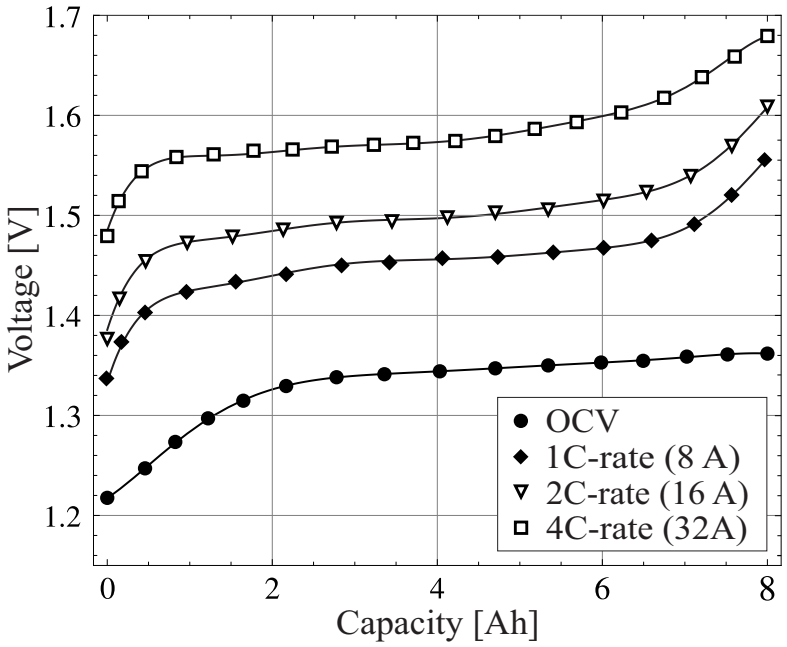

Figure 5.2: Variations of the battery voltage versus capacity (Ah) are shown during charging processes. Symbols indicate the data from Ref. [98], for open-circuit voltage (black circles), 8 A charging current (black diamonds), 16 A charging current (white triangles), and 32 A charging current (white squares). Solid lines represent sixth-order polynomial fits to the actual data.

temperature profiles of the battery core during charge at 1 C, 2 C, and 4 C constant current, borrowed from Ref. [98], with the ones obtained from the analytical model, at varying charging times under forced-convection cooling at all battery surfaces, $h_{z,0} = h_{z,L} = h_r = 25\,\mathrm{W\,m^{-2}\,K^{-1}}$. The sharp increase in the temperature corresponds to the overcharging period when the recombination reaction heat is involved [cf. Eq. (5.7)]. From the temperature trend, one can conclude that the total heat generation rate increases slowly during charging period and jumps quickly thereafter. When the cell is being charged, the reversible and irreversible (due to primary reactions) contribute to the total heat generation rate while the Joule heating is negligible [113]. When the cell is being overcharged, the heat generation rate increases dramatically because the enthalpy potential of recombination reaction are comparably large [cf.Eqs. (5.5) and (5.6)]. Initially, the recombination reaction is negligible, and

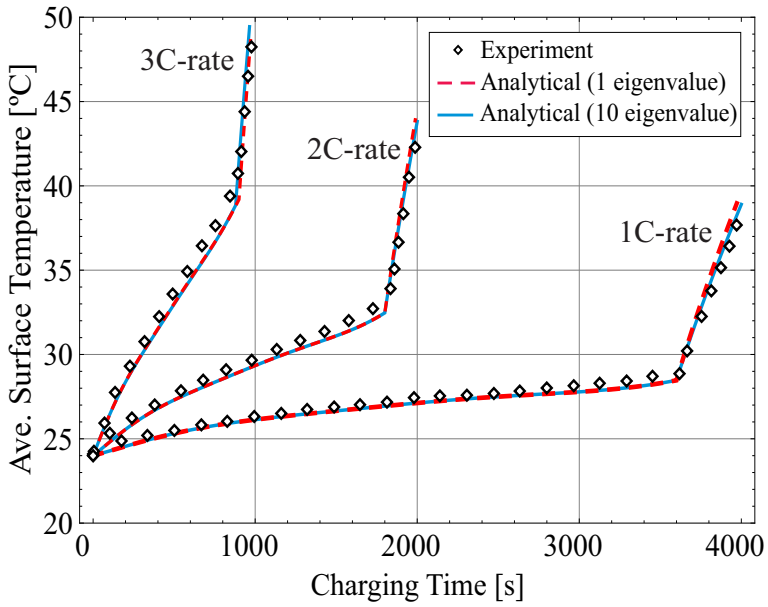

Figure 5.3: Calculated average surface temperature profiles of the battery core during charge at 1 C, 2 C, and 4 C constant current are compared to experimental temperature measurements (symbols) [98]. Analytical temperature distributions are denoted by dashed-line (red) for first term approximation and solid lines (blue) for series solution. A forced-convection cooling is considered at all surfaces of the battery, $h_{z,0} = h_{z,L} = h_r = 25\,\mathrm{W\,m^{-2}\,K^{-1}}$, and the ambient and initial temperature of 24 °C is assumed.

all the current applied to the cell is used to convert the active materials from discharge to charge state. When charge input exceeds 100 % of nominal cell capacity, it is obvious that the primary reaction current decreases, while the total current remain the same, consequently, the recombination reaction and relative heat generation rate become significant [113]. Figure 5.3 shows an excellent agreement between the analytical results and experimental measurements. The comparison shows that even the first term approximation (one eigenvalue) is accurate enough to predict the average surface temperature of the battery and further increase in the number of eigenvalues will not have any significant impact on the results accuracy.

The inconsistency between the measured and calculated temperature values later in the overcharging processes, is related to the fact that the rate of heat generation during overcharging period is overestimated in Eq. (5.7); because only part of generated oxygen at the positive electrode is reduced at the negative electrode [98]. Moreover, in the proposed analytical model, the battery thermal capacity, c_p, is assumed to be independent of temperature, and the thermal conductivity of the

porous materials is approximated by averaging, as given in Eq. (4.28) which in reality, due to the pores distribution and their size, the thermal conductivities may vary in different locations.

5.3.2 Model validation with numerical data

Variation of the maximum temperature, $T_{\max}$, at the center of the battery and the minimum temperature, $T_{\min}$, at the rim of the battery as a function charging time are shown in Fig. 5.4. A convective heat transfer with small and moderate heat transfer coefficients is assumed at all surfaces of the battery case, $h_{z,0} = h_{z,L} = h_r = \{6, 25\}\,\mathrm{W\,m^{-2}\,K^{-1}}$; and both ambient and initial conditions are set to $T_0 = 24\,^{\circ}\mathrm{C}$. The temperatures $T_{\max}$ and $T_{\min}$ calculated numerically with a finite element package (COMSOL Multiphysics, Version 4.3b), shown with symbols, are applied to validate the results obtained from proposed analytical model, shown with lines. In the numerical calculation, the relative tolerance was set to 10^{-6}. Since a pure diffusion model without any discontinuity is considered in this study, the numerical solution is not grid-dependent and takes seconds to two minutes as charge rate decreases.

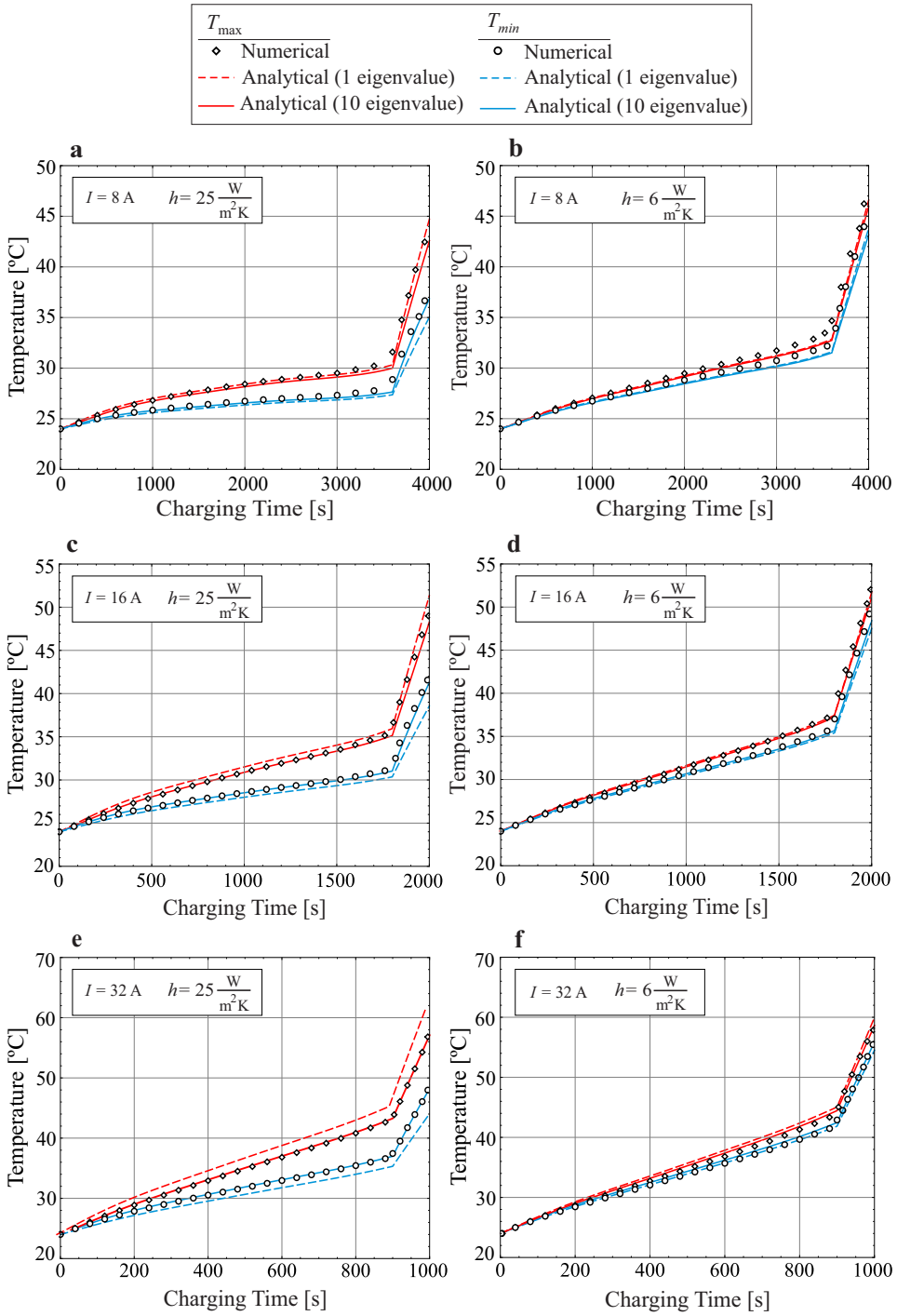

Figure 5.4: Temperature variation versus time is shown for different charge rates. Maximum temperature at the battery center (red lines) and minimum temperature at the battery rim (blue lines) are compared to numerical data for maximum and minimum temperature (symbols). In plots (a)-(f), thermal response of the battery during 8 A, 16 A, and 32 A charge current is shown for small and moderate heat transfer coefficients considered at all surfaces $h_{z,0} = h_{z,L} = h_r = \{6, 25\}\,\mathrm{W\,m^{-2}\,K^{-1}}$. The dashed lines represent the analytical results with first term approximation and solid lines indicate the series solution results.

The battery thermal responses at 8 A charging are plotted in Figs. 5.4a and b, whereas Figs. 5.4c and d represent the same information for 16 A charging current, and Figs. 5.4e and f correspond to the same data at 32 A charging current. Two sets of the analytical results are presented for $T_{\max}$ and $T_{\min}$, in which the dashed lines denote the analytical solution with the first eigenvalue in each direction only, i.e., the first term approximation, and the solid lines show the analytical solution with 10 eigenvalues, i.e., series solution. The comparisons show a fair agreement between the analytical and numerical results. From Fig. 5.4, one can conclude that the proposed analytical model is able to provide an acceptable accuracy with minimum computational effort which takes only a fraction of seconds. In other word, the main advantage of the developed analytical model, is that only the first eigenvalue in each direction is sufficient to predict the thermal behavior of the battery under different conditions in terms of charging current and convective cooling (natural or forced-convection).

5.3.3 Effect of convective cooling on temperature distribution

In Fig. 5.5, two-dimensional temperature profile at the end of charging at 32 A is shown. Plot (a) presents the temperature distribution when a forced convection is applied at all surfaces of the battery case, $h_{z,0} = h_{z,L} = h_r = 25\,\mathrm{W\,m^{-2}\,K^{-1}}$, while plot (b) present the temperature distribution when all the surfaces are faced to a natural-convection, $h_{z,0} = h_{z,L} = h_r = 6\,\mathrm{W\,m^{-2}\,K^{-1}}$. Plot (c) belongs to the case in which a forced-convection is assumed on top and lateral boundaries, $h_{z,L} = h_r = 25\,\mathrm{W\,m^{-2}\,K^{-1}}$, and a natural-convection on bottom boundary, $h_{z,0} = 6\,\mathrm{W\,m^{-2}\,K^{-1}}$, whereas plot (d) corresponds to the case in which a forced-convection is only used at the top boundary, $h_{z,L} = 25\,\mathrm{W\,m^{-2}\,K^{-1}}$, and natural-convection on the other boundaries, $h_{z,0} = h_r = 6\,\mathrm{W\,m^{-2}\,K^{-1}}$. The latter cases are defined to examine the effects of non-uniform boundary conditions on the temperature distribution. By comparing plots (a) with (b), we can conclude that although the battery temperature is markedly lower under forced-convection than natural-convection, when the charging process is under natural-convection the temperature gradient is not as pronounced as that under forced-convection, note the difference between minimum and maximum values of temperature. However, a more uniformed temperature distribution and a high heat dissipation rate are predicted in plot (c) when forced-convection is applied at the top and lateral surfaces of the battery case. Furthermore, plot (d) shows that applying forced-convection only at the top boundary can not be sufficient to dissipate the generated heat.

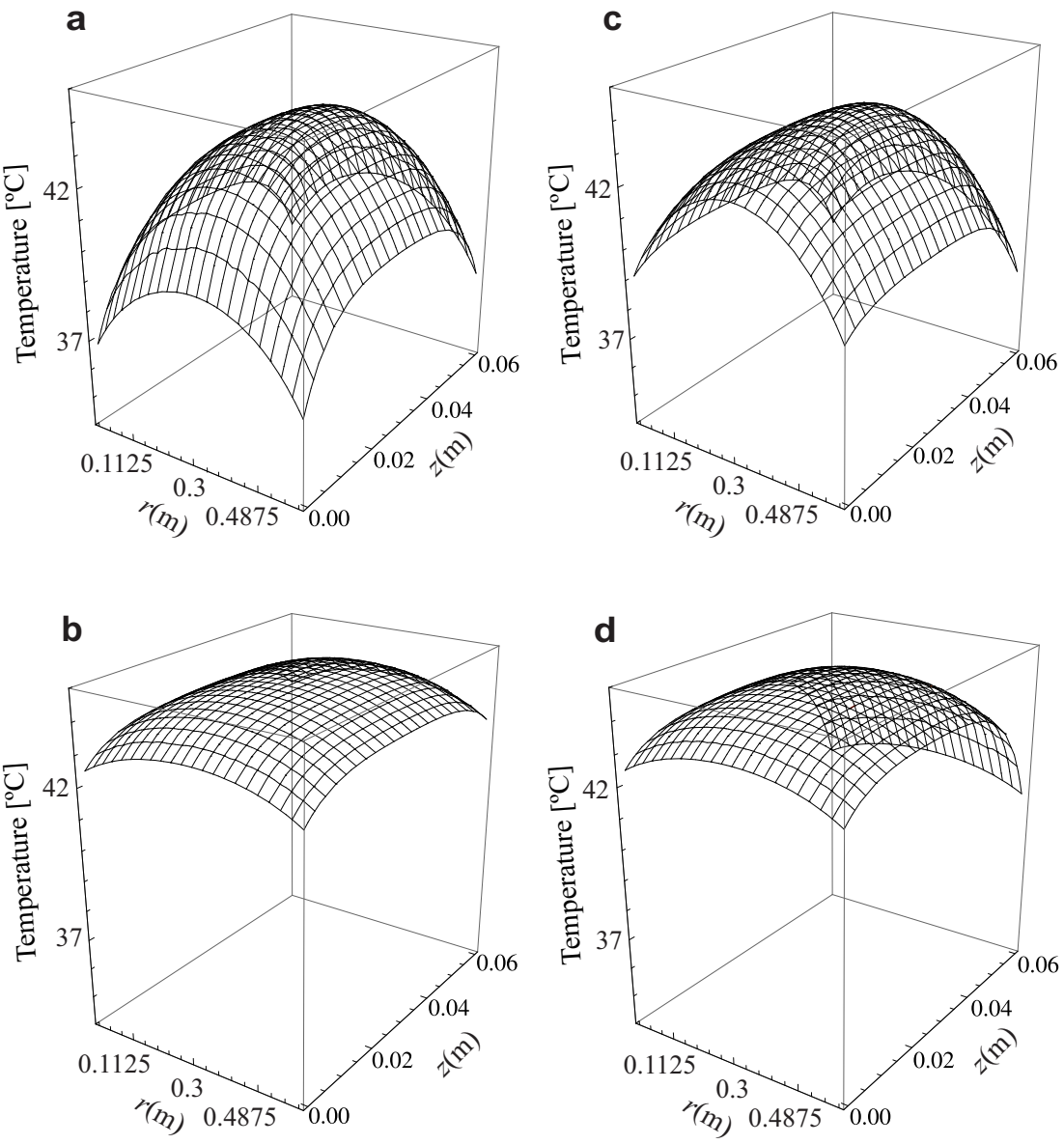

Figure 5.5: Two-dimensional temperature profile at the end of 32 A charge process is plotted for a) forced-convection at all surfaces $h_{z,0} = h_{z,L} = h_r = 25\,\mathrm{W\,m^{-2}\,K^{-1}}$, b) natural-convection at all surfaces $h_{z,0} = h_{z,L} = h_r = 6\,\mathrm{W\,m^{-2}\,K^{-1}}$, c) forced-convection at top and lateral surfaces $h_{z,L} = h_r = 25\,\mathrm{W\,m^{-2}\,K^{-1}}$ and natural-convection at the bottom surface $h_{z,0} = 6\,\mathrm{W\,m^{-2}\,K^{-1}}$, and d) forced-convection at the top surface $h_{z,L} = 25\,\mathrm{W\,m^{-2}\,K^{-1}}$ and natural-convection at other surfaces $h_{z,0} = h_r = 6\,\mathrm{W\,m^{-2}\,K^{-1}}$. Ambient and initial temperature of 24 °C is assumed.

5.4 Conclusion

The integral-transform technique introduced in the previous chapter was adapted to investigate the the temperature distribution in spirally wound batteries.

The developed model was employed to study the temperature rise in a 8 A h cylindrical NiMH cell during fast-charging processes with an overcharging periods at 1 C (8 A), 2C (16 A), and 4C (32 A) rates, where the transient heat generation during charging period was approximated from the electrical performance of the battery. The accuracy of the model was validated by comparing with experimental and numerical data. The comparisons confirmed that even the first term of the series solution suffices to accurately describe the two-dimensional temperature distribution inside the battery core with the modest computational effort. Hence, the proposed model can be considered as a robust tool for studying the thermal behavior of the spirally wound batteries in various operating conditions.

From the overcharge modeling, a sharp rise in the battery temperature was reported which is as a result of recombination heat; therefore, in fast-charging NiMH batteries, it is recommended to avoid overcharging. Furthermore, the results obtained from the proposed model demonstrated that, the heat dissipation can be improved by applying a forced-convection cooling at all battery surfaces, however it can increase the temperature gradient. The modeling of non-uniform boundary conditions suggested that a natural-convection at the bottom surface and forced-convection at the other surfaces of the battery, can result in a more uniform temperature and a high rate of heat dissipation.

To conclude, it is essential to point out that the major limitation of the developed thermal model is the necessity of linear boundary conditions. This limit that is defined by Sturm-Liouville theory, implies that the heat transfer coefficient, h, must be constant on the surface. In reality, when the batteries are horizontally arranged in the battery pack, the convective heat transfer coefficient, h, varies over battery surfaces, because the cooling fluid follows the curvature of the battery and this complicated flow pattern influences the heat transfer coefficient. Thus, the heat transfer coefficient will vary along the circumference of the battery (in φ-direction).

Chapter 6

Distributed Analytical Electro-Thermal Model for Pouch-Type Lithium-Ion Batteries

In this chapter, an analytic multi-physics model for pouch-type Li-ion batteries is presented, which to the best of authors knowledge, no analytical model has been introduced in this regard. In present model, both electrical and thermal processes occurring in the battery are considered to resolve their interplay on heat generation and battery thermal behavior. Voltage response of the sample Li-ion battery during galvanostatic discharge processes is measured to obtain the concentration-independent polarization expression introduced in previous section. Using the separation of variables method, a closed-form electrical model is proposed. Joule heating on each electrode evaluated from analytical description of the potential and current density fields, is used as a local heat source in a two-dimensional thermal model. The distributed thermal model is solved analytically with the method of integral transform. The analytical results are successfully validated through comparisons with experimental and numerical data.

6.1 Formulation of the problem

Figure 6.1a schematically shows the core of a pouch-type lithium-ion battery, corresponding to Fig. 3.1, that is constructed of several cell assemblies, also known as electrode assemblies. In Fig. 6.1b, a single cell assembly is depicted. For better illustration, different layers in the cell

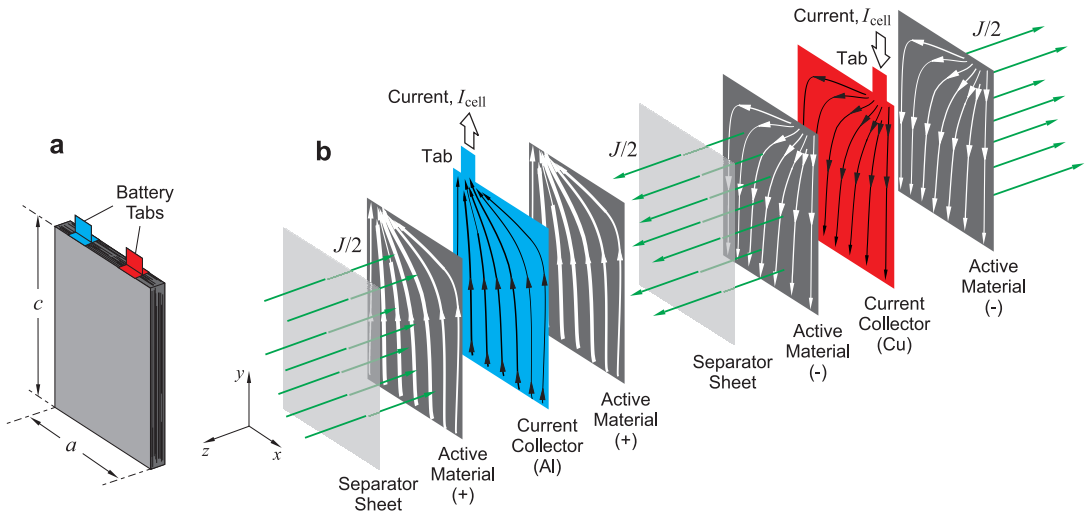

Figure 6.1: a) Core (electrode-separator stack) of a pouch-type lithium-ion battery is shown. b) Schematic of a single cell assembly in the battery is shown. The battery core is constructed by repeating the cell assembly. Different layers of the cell are separated for the sake of presentation. The arrows in z-direction correspond to transfer current, the transport of Li^+ from the negative electrode to the positive electrode during a discharge process. The arrows in x-y plane represent current streamlines on electrodes.

assembly are shown separated while in the actual battery these layers are compressed; see Fig. 6.1b. Each cell assembly includes a negative electrode, two layers of separator sheets, and a positive electrode.

Arrows in Fig. 6.1 b present current streamlines during discharge processes. The through-plane straight arrows represent the transport of Li^+ between the electrodes, i.e., transfer current. The in-plane arrows in x-y plane represent the transport of charges (e^-), i.e., the electrical current, on the electrode layers. The direction of transfer and electric currents is reversed for a charging process. As shown in the Fig. 6.1b, electrical constriction occur at the tabs of positive and negative electrodes. For the sake of convenience, the transfer current on both sides of each electrode can be considered to occur on one side of the electrodes. This approach is common in the literature.

6.1.1 Electrical model

A dimensional analysis can be performed to show that owing to the small thickness of layers in the cell assembly, compared to their dimensions in x- and y-directions, the distribution of potential in the electrodes is two-dimensional in x-y plane [114]. Accordingly, the governing differential

equation for the charge balance in each electrodes reads

$$-\nabla \cdot \mathbf{i}_j + \frac{\mathbf{J} \cdot \mathbf{n}_j}{\delta_{\text{elec},j}} = 0 \quad (j = p, n) \tag{6.1}$$

where $\mathbf{i}_j = \{i_x, i_y, 0\}_j$ is the in-plane current density vector on each electrode (A m^{-2}). The subscript j corresponds to domains of the positive electrode Ω_p and the negative electrode Ω_n. The reaction current density vector on the electrodes is $\mathbf{J} = \{J_x, J_y, J\}$ in (A m^{-2}), where J_x and J_y are side reactions and are considered to be negligible. The through-plane component of the reaction current, J, referred to as transfer current, corresponds to the intercalation of lithium ions in active materials on both sides of the electrodes. The electrode thickness in z-direction is $\delta_{\text{elec},j}$ in (m), and $\mathbf{n}_j$ is the unit normal vector on each electrode surface pointing outward; $\mathbf{n}_p = \{0, 0, -1\}$ and $\mathbf{n}_n = \{0, 0, +1\}$.

According to the Ohm's law, components of $\mathbf{i}_j$ are related to the potential distribution via

$$i_{x,j} = -\sigma_{\text{eff},j} \frac{\partial V_j}{\partial x} \quad \text{and} \quad i_{y,j} = -\sigma_{\text{eff},j} \frac{\partial V_j}{\partial y} \quad (j = p, n) \tag{6.2}$$

where x and y indicate the spatial position (m), and $V_j = V_j(x, y)$ is the two-dimensional potential distribution in the electrode (V).

The quantity $\sigma_{\text{eff},j}$ is the effective electrical conductivity (S m^{-1}), that for each electrode is

$$\sigma_{\text{eff},j} = \frac{1}{\delta_{\text{elec},j}} \left(\delta_{\text{cc},j} \, \sigma_{\text{cc},j} + 2\delta_{\text{am},j} \, \sigma_{\text{am},j} \right) \quad (j = p, n) \tag{6.3a}$$

where

$$\delta_{\text{elec},j} = \delta_{\text{cc},j} + 2\delta_{\text{am},j} \quad (j = p, n) \tag{6.3b}$$

and $\delta_{\text{cc},j}$ and $\delta_{\text{am},j}$ are thicknesses of current collector and active material layers, respectively. Electrical conductivity of the current collector and the active material are denoted by $\sigma_{\text{cc},j}$ and $\sigma_{\text{am},j}$.

As depicted in Fig. 6.2, each electrode can be considered as a rectangular domain in x-y plane of width a and height c. The through-plane current enters (or exits) the domain through its surface in x-y plane, whereas the in-plane current is allowed to exit (or enter) the domain through the tab constriction of width b on the boundary at $y = c$. The distance between the centre of the tab and y-axis is denoted by e_j. With reference to Fig. 6.2, the relevant boundary conditions for Eq. (6.1) at

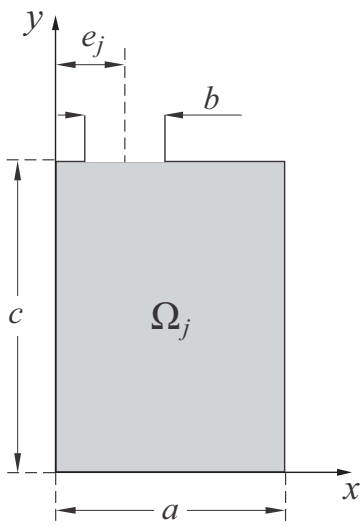

Figure 6.2: Two-dimensional schematic of electrodes in x-y plane. Width and height of electrodes and width of the electrode tab are the same for both positive and negative electrodes. The distance of the tab centre from y-axis, denoted by e_j, differs between the electrodes.

the positive domain are

$$-\sigma_{\text{eff},p}\frac{\partial V_p}{\partial x} = 0 \quad \text{at} \quad x = 0 \tag{6.4a}$$

$$-\sigma_{\text{eff},p}\frac{\partial V_p}{\partial x} = 0 \quad \text{at} \quad x = a \tag{6.4b}$$

$$-\sigma_{\text{eff},p}\frac{\partial V_p}{\partial y} = 0 \quad \text{at} \quad y = 0 \tag{6.4c}$$

$$-\sigma_{\text{eff},p}\frac{\partial V_p}{\partial y} = i_{\text{tab},p} \quad \text{at} \quad e_p - \frac{b}{2} < x < e_p + \frac{b}{2}, \quad y = c \tag{6.4d}$$

$$-\sigma_{\text{eff},p}\frac{\partial V_p}{\partial y} = 0 \quad \text{at} \quad e_p + \frac{b}{2} < x < e_p - \frac{b}{2}, \quad y = c \tag{6.4e}$$

Similarly, for the negative domain

$$-\sigma_{\text{eff},n}\frac{\partial V_n}{\partial x} = 0 \quad \text{at} \quad x = 0 \tag{6.5a}$$

$$-\sigma_{\text{eff},n}\frac{\partial V_n}{\partial x} = 0 \quad \text{at} \quad x = a \tag{6.5b}$$

$$-\sigma_{\text{eff},n}\frac{\partial V_n}{\partial y} = 0 \quad \text{at} \quad y = 0 \tag{6.5c}$$

$$V_n = 0 \quad \text{at} \quad e_n - \frac{b}{2} < x < e_n + \frac{b}{2}, \quad y = c \tag{6.5d}$$

$$-\sigma_{\text{eff},n}\frac{\partial V_n}{\partial y} = 0 \quad \text{at} \quad e_n + \frac{b}{2} < x < e_n - \frac{b}{2}, \quad y = c \tag{6.5e}$$

The above boundary conditions imply that no current passes through boundaries of Ω_p and Ω_n except for the tab boundaries. In Eq. (6.4d), $i_{\text{tab},p}$ is the in-plane current density (A m^{-2}) at the tab of positive electrode

$$i_{\text{tab},p} = \frac{I_{\text{cell}}}{b\,\delta_{\text{elec},p}} \tag{6.6}$$

where I_{cell} is the applied discharge current (A) for a single cell (electrode) assembly, and $b\,\delta_{\text{elec},p}$ is the cross-sectional area of the positive tab. In Eq. (6.5d), potential at the tab boundary of the negative electrode is set to zero in order to provide a reference for voltage distribution [115].

6.1.2 Two-dimensional thermal model

In the electrical model it was assumed that potential distribution is independent of z-direction. This assumption can be extended to the thermal model as well; since thickness of electrodes in z-direction is very small compared to their dimensions in x- and y-directions, heat will conduct quickly across the thin direction and the temperature will become, to a good approximation, uniform across z-direction [116]. Also, in Section 4.3 where the thermal performance in the cross-section of the Li-ion battery is investigated, the results show that the non-uniformity in through-plane direction would not be significant when the thickness of cell is small comparing to other dimensions. Accordingly, the three-dimensional energy balance equation defined in Eq. 5.2 can be modified as;

$$\rho c_p \frac{\partial T}{\partial t} = \kappa_{\text{eff}} \frac{\partial^2 T}{\partial x_1^2} + \kappa_{\text{eff}} \frac{\partial^2 T}{\partial x_2^2} + \dot{g}, \tag{6.7}$$

κ_{eff}, the in-plane thermal conductivity of the cell assembly calculated from

$$\kappa_{\text{eff}} = \frac{1}{\delta_{\text{cell}}} \left(\delta_{\text{cc},p}\,\kappa_{\text{cc},p} + \delta_{\text{cc},n}\,\kappa_{\text{cc},n} + 2\delta_{\text{am},p}\,\kappa_{\text{am},p} + 2\delta_{\text{am},n}\,\kappa_{\text{am},n} + 2\delta_{\text{ss}}\,\kappa_{\text{ss}}\right) \tag{6.8a}$$

where

$$\delta_{\text{cell}} = \delta_{\text{cc},p} + \delta_{\text{cc},n} + 2\delta_{\text{am},p} + 2\delta_{\text{am},n} + 2\delta_{\text{ss}} \tag{6.8b}$$

with δ_{ss} as the thickness of separator sheet. Thermal conductivities of current collector foils, active materials, and separator sheet are denoted by κ_{cc}, κ_{am}, and κ_{ss}, respectively, and their values are listed in Table 3.2.

The net rate of volumetric heating inside the battery is the difference between heat generation and heat dissipation rates

$$\dot{g} = \nu_{\text{ec}}\,\dot{g}_{\text{ec}} + \nu_{\text{elec},p}\,\dot{g}_{\text{ohm},p} + \nu_{\text{elec},n}\,\dot{g}_{\text{ohm},n} - \frac{q_{\text{diss}}}{\delta_{\text{cell}}} \tag{6.9}$$

where $\dot{g}_{\mathrm{ec}}$ and $\dot{g}_{\mathrm{ohm},j}$ are the electrochemical and ohmic heat generation rates per unit volume. The coefficients ν_{ec} and $\nu_{\mathrm{elec},j}$ are volume ratios for electrochemical and ohmic heat generation rates [114]

$$\nu_{\mathrm{ec}} = \frac{\mathscr{V}_{\mathrm{ec}}}{\mathscr{V}_{\mathrm{cell}}} = \frac{2\delta_{\mathrm{am},p} + 2\delta_{\mathrm{am},n} + 2\delta_{\mathrm{ss}}}{\delta_{\mathrm{cell}}}$$

$$\nu_{\mathrm{elec},j} = \frac{\mathscr{V}_{\mathrm{elec},j}}{\mathscr{V}_{\mathrm{cell}}} = \frac{2\delta_{\mathrm{am},j} + 2\delta_{\mathrm{cc},j}}{\delta_{\mathrm{cell}}} \quad (j = p,n)$$

The quantities $\mathscr{V}_{\mathrm{cell}}$, $\mathscr{V}_{\mathrm{elec},j}$, and $\mathscr{V}_{\mathrm{ec}}$ denote the total volume of the cell assembly, volume of each electrode, and volume of the cell which participates in electrochemical reactions.

The electrochemical heat in each electrode is calculated from Bernardi equation, Eq. (4.4). Likewise Section 4.3, we assume $\mathrm{d}V_{\mathrm{oc}}/\mathrm{d}T$ is constant and its value is considered 0.0002 ($\mathrm{V\,K^{-1}}$) [8, 44].

For each electrode, the ohmic (Joulean) heat generation rate reads

$$\dot{g}_{\mathrm{ohm},j} = \frac{1}{\sigma_{\mathrm{eff},j}}(i_{x,j}^2 + i_{y,j}^2) \quad (j = p,n) \tag{6.10}$$

where i_x and i_y are the components of in-plane current density on each electrode obtained from the electrical model; see Eq. (6.2).

The last term in Eq. (6.9) takes account for the volumetric heat dissipation to the ambient from x-y plane. The heat dissipation flux q_{diss} is calculated from Newton's law of cooling

$$q_{\mathrm{diss}} = 2\,h_{\mathrm{eff}}\,(T_{\mathrm{s}} - T_0) \tag{6.11}$$

where T_0 is the constant ambient temperature, T_{s} is the surface temperate, and h_{eff} is the effective heat transfer coefficient ($\mathrm{W\,m^{-2}\,K^{-1}}$) at the surface of the cell (both front and back surfaces in x-y plane).

The thermal boundary conditions for the energy balance equation [cf. Eq. (6.7)] are

$$-\kappa_{\mathrm{eff}}\frac{\partial T}{\partial x} = \left[\frac{\delta_{\mathrm{case}}}{\kappa_{\mathrm{case}}} + \frac{1}{h_{x,0}}\right]^{-1}(T - T_0) \quad \text{at} \quad x = 0 \tag{6.12a}$$

$$+\kappa_{\mathrm{eff}}\frac{\partial T}{\partial x} = \left[\frac{\delta_{\mathrm{case}}}{\kappa_{\mathrm{case}}} + \frac{1}{h_{x,a}}\right]^{-1}(T - T_0) \quad \text{at} \quad x = a \tag{6.12b}$$

$$-\kappa_{\mathrm{eff}}\frac{\partial T}{\partial y} = \left[\frac{\delta_{\mathrm{case}}}{\kappa_{\mathrm{case}}} + \frac{1}{h_{y,0}}\right]^{-1}(T - T_0) \quad \text{at} \quad y = 0 \tag{6.12c}$$

$$+\kappa_{\mathrm{eff}}\frac{\partial T}{\partial y} = \left[\frac{\delta_{\mathrm{case}}}{\kappa_{\mathrm{case}}} + \frac{1}{h_{y,c}}\right]^{-1}(T - T_0) \quad \text{at} \quad y = c \tag{6.12d}$$

where δ_{case} and κ_{case} are the thickness and the thermal conductivity of the battery case; see Table 3.2. The convective heat transfer coefficients are denoted by h ($\mathrm{W\,m^{-2}\,K^{-1}}$) with relevant subscripts

which indicate the location of the boundary. The initial temperature of the battery is assumed to be the ambient temperature.

$$T = T_0 \quad \text{at} \quad t = 0 \tag{6.13}$$

6.2 Polarization expression

Distribution of the transfer current density J, which appears in the electrical model [cf. Eq. (6.1)], is dictated by the local rate of electrochemical reactions in electrodes. For an accurate description of J a distributed electrochemical model [24, 114] is preferred. In this study, instead of using an electrochemical model, a mathematical model [71, 117] is employed to predict the time dependent distribution of J in the experimental battery during constant-current discharge processes. The model uses a concentration-independent polarization expressions to describe the local overpotential between the electrodes. Some parameters in the polarization expression must be evaluated from experimental data. The procedure explained below can be applied to obtain polarization expressions for both charge and discharge processes. For charge processes, experimental data for charging are required. In this study, only discharge mode is considered.

Experimental observations [71] and electrochemical simulations [32] of galvanostatic discharge processes confirm that at a fixed depth-of-discharge (DOD), the battery voltage exhibits an approximately linear dependency on current density. Accordingly, a linear polarization expression can be assumed as [71, 115, 117]

$$J(x,y) = Y_{\text{ec}} \left[V_p(x,y) - V_n(x,y) - V_{\text{oc}} \right] \tag{6.14}$$

where, Y_{ec} is the electrochemical conductance (i.e., the conductance of separator and electrolyte) per unit area of the cell (S m^{-2}), and $V_p - V_n$ corresponds to the potential difference between two points on the positive and negative electrodes with the same coordinates in x-y plane. By convention, J assumes positive and negative values for charge and discharge processes, respectively.

The current of the cell assembly I_{cell} and the current of battery I_{batt} are related to the transfer current density J via

$$I_{\text{cell}} = \int_0^a \int_0^c J(x,y)\, dy\, dx \quad \text{and} \quad I_{\text{batt}} = I_{\text{cell}} N \tag{6.15}$$

The number of cell assemblies inside the battery core [cf. Fig. 6.1a] is denoted by N. For the considered battery $N = 18$.

In the mathematical model, both Y_{ec} and V_{oc} are considered to solely depend on DOD, and their dependency is expressed in a polynomial form

$$Y_{ec} = \sum_{l=0}^{L} \mathscr{C}_l \, \mathrm{DOD}^l \tag{6.16}$$

$$V_{oc} = \sum_{m=0}^{M} \mathscr{D}_m \, \mathrm{DOD}^m \tag{6.17}$$

where $\mathscr{C}_l$ and $\mathscr{D}_m$ are the constants to be determined from experimental voltage data during constant-current discharge processes.

DOD is defined as the fraction of cell capacity Q_{cell} (Ah), released during a discharge process. Given an initial DOD at $t = 0$ and assuming 100% coulombic efficiency, DOD (in %) can be calculated related to discharge time t (s) via

$$\mathrm{DOD}(t) = \mathrm{DOD}(0) + \frac{1}{3600\, Q_{cell}} \int_0^t |I_{cell}(t)| \, dt \tag{6.18}$$

where $Q_{cell} = Q_{batt}/N$ and the constant 3600 has the unit of second/hour.

To find coefficients $\mathscr{C}_l$ and $\mathscr{D}_m$, experimental data must be used to evaluate the battery voltage, V_{batt}, at different DOD values during discharge processes at different currents. In Fig. 6.3, battery voltage variations are plotted against $\bar{J} = I_{cell}/(a\,c)$, which is the mean value for transfer current J. As shown in the figure, at a constant DOD, variations of the battery voltage versus transfer current density, shown by symbols, can be approximated by a linear function (lines). In account for Eq. (6.14), Y_{ec} is the inverse of the line slope and V_{oc} is the intercept [71]. Plots in Fig. 6.4a and b depict the dependency of V_{oc} and Y_{ec} on DOD, obtained from measurements presented in Chapter 3 [cf. Fig. 3.8] and the above-mentioned procedure. Solid lines present sixth-order polynomial fits to the calculated values (symbols).

To account for temperature effects in the polarization expression, dependency of the electrochemical conductance and open-circuit potential on temperature must be considered. According to Arrhenius equation which gives the relationship between the electrochemical reaction rate constant and the temperature, a temperature dependent Y_{ec} can be defined [58, 118]

$$Y_{ec} = Y_{ec,ref} \, \mathrm{Exp}\left[\mathscr{C}_T \left(\frac{1}{T_0} - \frac{1}{T_{ref}}\right)\right] \tag{6.19}$$

Furthermore, Nernst equation which gives the relationship between the equilibrium potential and the temperature can be used to describe the Seebeck effect on V_{oc} [58, 118]

$$V_{oc} = V_{oc,ref} + \mathscr{D}_T \, (T_0 - T_{ref}) \tag{6.20}$$

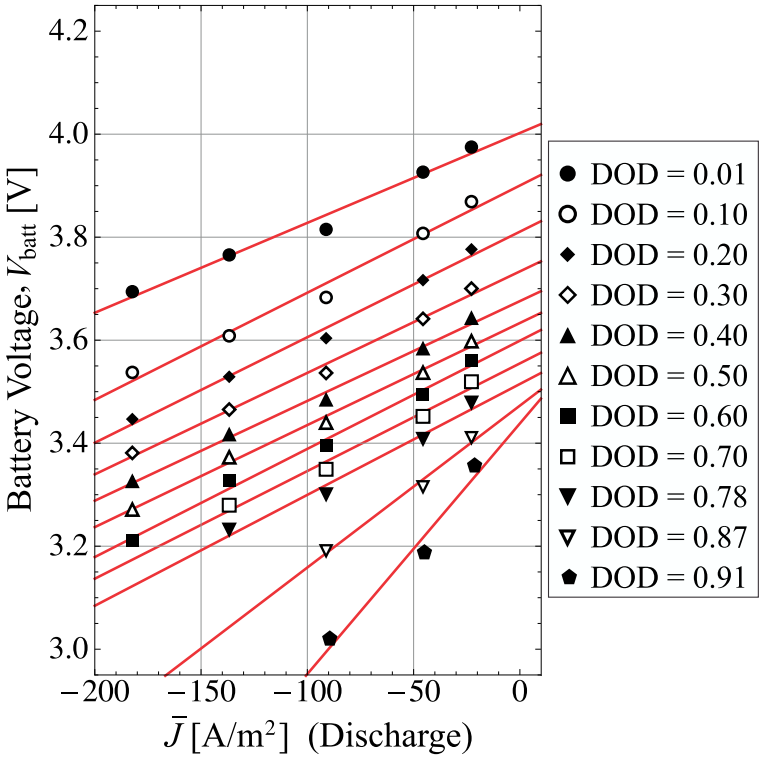

Figure 6.3: The linear dependency of battery voltage and transfer current density at constant values of DOD.

The coefficients $\mathscr{C}_T$ and $\mathscr{D}_T$ are constants that must be determined from experiment [58, 118] to fit the temperature dependence of Y_{ec} and V_{oc}. The subscript 'ref' denotes values at a reference temperature T_{ref}. In this study, $T_{ref} = T_0$ is considered.

6.3 Numerical analysis

Equations in Sections 6.1 and 6.2, which govern the electro-thermal performance of the cell, form a nonlinear system and must be solved numerically. A finite element PDE solver, COMSOL MULTIPHYSICS (Version 4.3a), is used to simultaneously solve the governing equations over two separated domains, Ω_p and Ω_n, to obtain: i) the transient fields of potential on each electrode, ii) variations of transfer current density between the electrodes, and iii) temperature distribution in the cell assembly.

Once the potential distribution on positive and negative electrodes is calculated numerically, averaged potential over the positive tab at different DOD values yields the voltage response of the

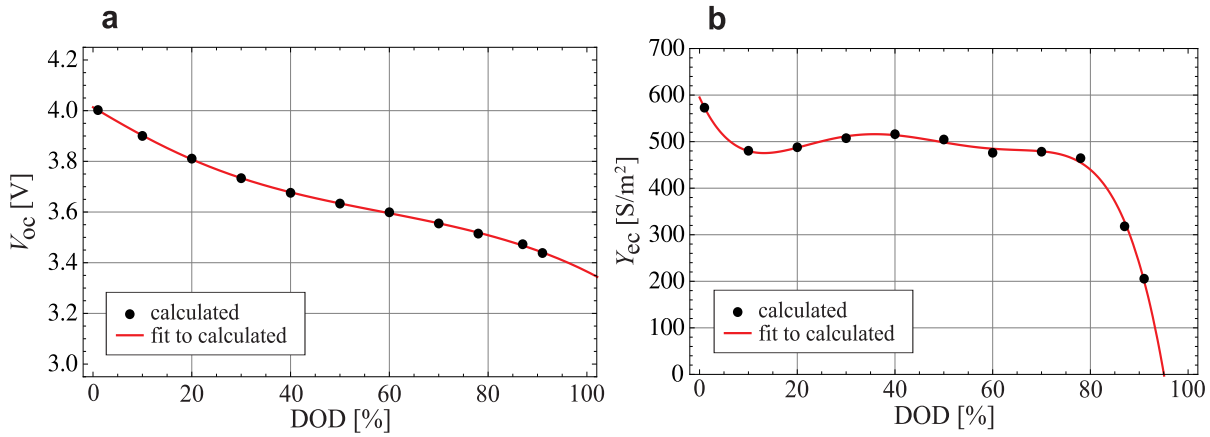

Figure 6.4: a) The dependency of open-circuit potential V_{oc} on DOD. b) The dependency of electrochemical conductance Y_{ec} on DOD.

battery

$$V_{batt} = V_{tab,p} - V_{tab,n} = \frac{1}{b}\int_{e_p-\frac{b}{2}}^{e_p+\frac{b}{2}} V_p(x,c)\,dx \tag{6.21}$$

where b is the width of the tab.

In Fig. 6.5, voltage response of the battery at different discharge rates, calculated from Eq. (6.21), is compared to experimental voltage values, i.e., data in Fig. 3.8. The comparison shows a satisfactory agreement between the calculated and measured voltage of the battery, even at the nonlinear portion of discharge curves. Note that since cell assemblies inside the battery core are connected in parallel, $V_{batt} = V_{cell}$. Our numerical analysis shows that at the beginning of a discharge the transfer

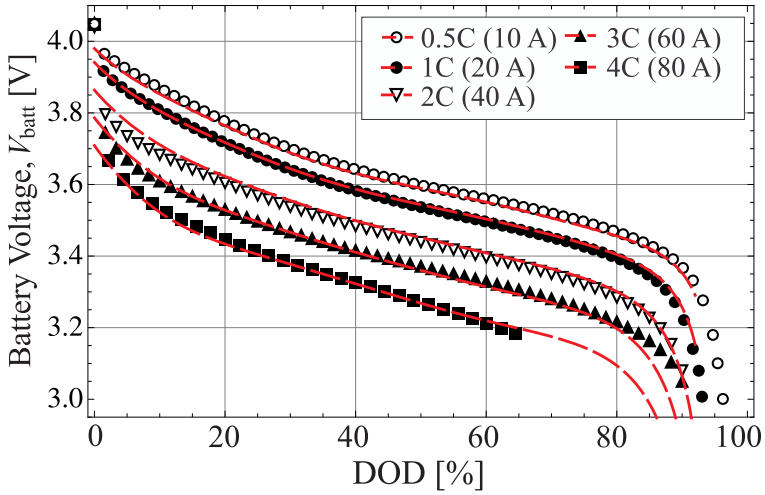

Figure 6.5: Variation of battery voltage versus depth-of-discharge (DOD) for different discharge currents are shown. Symbols correspond to measured values and lines represent numerically calculated values.

current density J is concentrated near the tabs. At mid-way through the discharge the distribution of J becomes quite uniform, but still remains slightly higher in the vicinity of tabs. However, near the end of discharge when active materials are depleted near the tabs, the transfer current is forced away from the tabs towards the bottom of electrodes where active materials are less utilized. We observed this trend at all discharge rates.

To investigate the distribution of transfer current during discharge processes, its maximum and minimum values are reported relative to the mean value and normalized by the mean value, i.e., $(J-\bar{J})/\bar{J}$. Variation of $(J_{\min}-\bar{J})/\bar{J}$ and $(J_{\max}-\bar{J})/\bar{J}$ with respect to DOD at different discharge rates (2 C, 3 C, and 4 C) are calculated from numerical model and plotted in Fig. 6.6. The plots confirm that maximum deviation of J with respect to $\bar{J}$ is about 6 %. This observation suggest that a uniform transfer current can be assumed during discharge processes. This is the key assumption in development of the analytical electro-thermal model in the following sections.

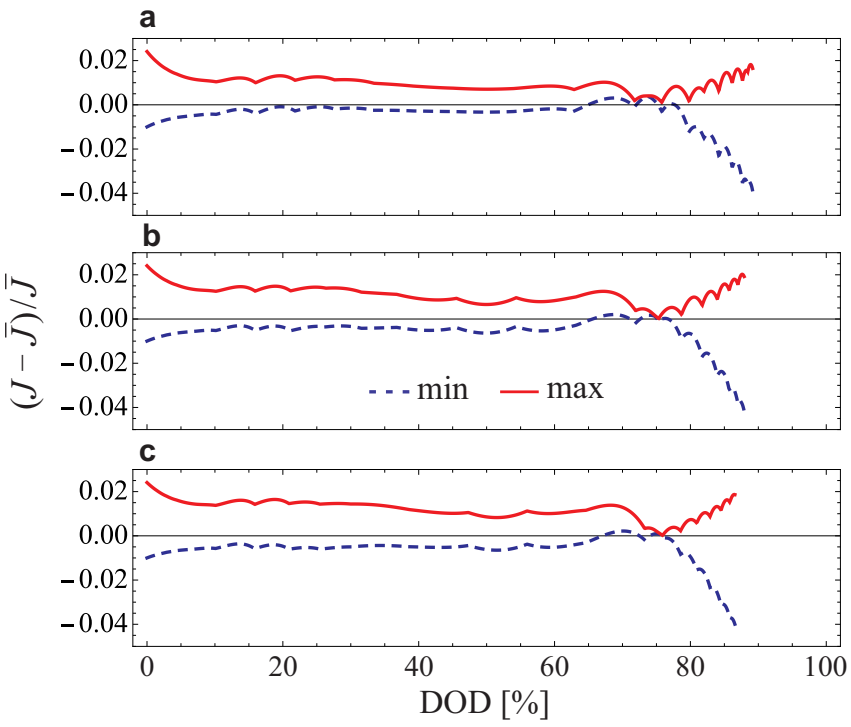

Figure 6.6: Minimum and maximum deviations of transfer current J with respect to the mean value $\bar{J}$ are shown during discharge processes at 2C-rate (plot a), 3C-rate (plot b), and 4C-rate (plot c).

6.4 Analytical solutions

In this section, closed-form analytical solutions for electrical problem (Section 6.1.1) and thermal problem (Section 6.1.2) are developed. We shall solve the electrical problem first to find the distribution of in-plane current density vector $\mathbf{i}_j$ on electrodes. Nonetheless, in order to approach the problem analytically, a uniform transfer current density J must be assumed.

Results from the numerical analysis show that transfer current is not uniformly distributed; however, its variations is not drastic—less then 6% during most of the discharge process, as shown in Fig. 6.6. Accordingly, a uniform transfer current density is superimposed in our analysis which allows to develop a theoretical electro-thermal analysis. A similar assumption is proposed by Doyle and Newman [119] for development of an analytical electrochemical model. Note that uniformity of transfer current is a desired feature for Li-ion batteries; it means that active materials are evenly utilized and battery degradation rate is minimized.

6.4.1 Analytical solution for potential and current density distributions

We define a new variable to transform the governing Poisson equation, Eq. (6.1), and the corresponding boundary conditions, Eqs. (6.4e) and (6.5e), into a Laplace equation, for which an analytical solution is accessible with the method of separation of variables. Let us introduce w, that relates V to $\bar{\mathbf{J}}.\mathbf{n}$ via

$$V_j(x,y) = w_j(x,y) - \frac{1}{2}\frac{\bar{\mathbf{J}}.\mathbf{n}_j}{\delta_{\text{elec},j}\sigma_{\text{eff},j}}y^2 \qquad (j=p,n) \tag{6.22}$$

Substituting $V_j(x,y)$ from Eq. (6.22) into Eq. (6.1) and boundary conditions (6.4e) and (6.5e) yields the following homogenous equation

$$\frac{\partial^2 w_j}{\partial x^2} + \frac{\partial^2 w_j}{\partial y^2} = 0 \qquad (j=p,n) \tag{6.23}$$

with transformed boundary conditions for both electrodes ($j=p,n$)

$$\frac{\partial w_j}{\partial x} = 0, \quad \text{at} \quad x = 0, \tag{6.24a}$$

$$\frac{\partial w_j}{\partial x} = 0, \quad \text{at} \quad x = a, \tag{6.24b}$$

$$\frac{\partial w_j}{\partial y} = 0, \quad \text{at} \quad y = 0, \tag{6.24c}$$

$$\frac{\partial w_j}{\partial y} = \frac{\left(\bar{\mathbf{J}}.\mathbf{n}\right) c}{\delta_{\text{elec},j}\, \sigma_{\text{eff},j}} \left(1 - \frac{a}{b}\right), \quad \text{at} \quad e_j - \frac{b}{2} < x < e_j + \frac{b}{2}, \;\; y = c, \tag{6.24d}$$

$$\frac{\partial w_j}{\partial y} = \frac{\left(\bar{\mathbf{J}}.\mathbf{n}_j\right) c}{\delta_{\text{elec},j}\, \sigma_{\text{eff},j}}, \quad \text{at} \quad e_j + \frac{b}{2} < x < e_j - \frac{b}{2}, \;\; y = c \tag{6.24e}$$

Note that in derivation of Eq. (6.24d) for the positive electrode, the cell discharge current I_{cell} is replaced with $(\bar{\mathbf{J}}.\mathbf{n})\, ac$, with reference to Eq. (6.15). Also, for the negative electrode an equivalent second-type (Neumann) boundary condition is introduced instead of the original first-type (Dirichlet) boundary condition, because the method of separation of variables with mixed boundary conditions cannot be applied on a Laplace equation. For this reason a reference potential of zero cannot be prescribed in the analytical approach. Indeed, in the transformed system, the through-plane current density is eliminated from the source term of the original Poisson equation and its effects are reflected on the transformed boundary conditions.

Using the method of separation of variables,the general solution for Eq.(6.22) can be given as

$$w_j(x,y) = \sum_{k=1}^{\infty} A_{k,j} \cos(\alpha_k x) \cosh(\alpha_k y) \qquad (j = p,n) \tag{6.25}$$

in which the summation is taken over all discrete spectrum of eigenvalues $\alpha_k = k\pi/a$. The terms $\cos(\alpha_k x)$ and $\cosh(_k y)$ are the eigenfunctions, and $A_{k,j}$ is the coefficient to be determined for each domain $(j = p,n)$ from boundary conditions at $y = c$, i.e.

$$\sum_{k=1}^{\infty} A_{k,j} \cos(\alpha_k x) \sinh(\alpha_k y) = \begin{cases} \dfrac{\bar{\mathbf{J}}.\mathbf{n}_j\, c}{\delta_{\text{elec},j}\, \sigma_{\text{eff},j}} \left(1 - \dfrac{a}{b}\right) & \text{at} \quad e_j - \dfrac{b}{2} < x < e_j + \dfrac{b}{2} \\ \dfrac{\bar{\mathbf{J}}.\mathbf{n}_j\, c}{\delta_{\text{elec},j}\, \sigma_{\text{eff},j}} & \text{at} \quad e_j + \dfrac{b}{2} < x < e_j - \dfrac{b}{2} \end{cases} \tag{6.26}$$

The unknown coefficient $A_{k,j}$ must be obtained from the orthogonality condition for eigenfunctions [73, 74]

$$\int A_{k,j}\, \alpha_k \cos(\alpha_k x) \cos(\alpha_l x) \sinh(\alpha_k c) dx = 0 \quad \text{for} \quad k \neq l \tag{6.27}$$

Thus, multiplying both sides of Eq. (6.26) with $cos\alpha_l x$ and subsequent integrating yields the following relation for $l = k$

$$\int A_{k,j}\,\alpha_k \cos^2(\alpha_k x)\,\sinh(\alpha_k c)dx = \frac{\bar{\mathbf{J}}.\mathbf{n}_j\,c}{\delta_{\text{elec},j}\,\sigma_{\text{eff},j}} \left[\int_0^{e_j-\frac{b}{2}} \cos(\alpha_k x)dx + \left(1-\frac{a}{b}\right)\int_{e_j-\frac{b}{2}}^{e_j+\frac{b}{2}} \cos(\alpha_k x)dx + \int_a^{e_j+\frac{b}{2}} \cos(\alpha_k x)dx\right] \quad (6.28)$$

from which $A_{k,j}$ is evaluated as

$$A_{k,j} = \frac{4\left(\bar{\mathbf{J}}.\mathbf{n}_j\right)\,c\,\left[b\,\sin(\alpha_k a) - 2\,a\cos(\alpha_k e_j)\sin(\alpha_k b/2)\right]}{\delta_{\text{cell},j}\sigma_{\text{eff},j}\,b\,\alpha_k\,\sinh(\alpha_k c)\,[2\,\alpha_k a + \sin(2\,\alpha_k a)]} \quad (6.29)$$

Finally, the solution for potential follows from Eq. (6.22)

$$V_j(x,y) = \sum_{k=1}^{\infty} A_{k,j}\cos(\alpha_k x)\cosh(\alpha_k y) - \frac{1}{2}\frac{\bar{\mathbf{J}}.\mathbf{n}_j}{\delta_{\text{elec},j}\,\sigma_{\text{eff},j}}y^2 \quad (6.30)$$

Once the potential distribution is known, the in-plane current distribution can be obtained from Eq. (6.2).

6.4.2 Analytical solution for temperature distribution

Equation (6.7) that describes the transient two-dimensional temperature distribution inside the battery core is solved analytically using the method of integral-transformation as detailed in Chapter 4 for three-dimensional energy equation. Using the polarization expression in Eq. (6.14), one can rewrite the overpotential term in Eq. (4.4) as

$$V_p - V_n - V_{\text{oc}} = \frac{\bar{J}}{Y_{\text{ec}}} \quad (6.31)$$

Accordingly, the electrochemical heat generation in Eq. (4.4) recasts to

$$\dot{g}_{\text{ec}} = \frac{I_{\text{cell}}}{\mathscr{V}_{\text{cell}}}\left[\frac{\bar{J}}{Y_{\text{ec}}} + T\frac{dV_{\text{oc}}}{dT}\right] \quad (6.32)$$

For the sake of convenience in formulation of the integral-transformation technique we define a new temperature function $\theta(x,y,t) = T(x,y,t) - T_0$. The respective double integral-transformation and the inversion formula for $\theta(x,y,t)$ in a two-dimensional domain with $x \in [0,a]$ and $y \in [0,c]$ are

$$\bar{\bar{\theta}}(\beta_m,\gamma_n,t) = \int_{x'=0}^{a}\int_{y'=0}^{c} \Phi\left(\beta_m,x'\right)\cdot\Psi\left(\gamma_n,y'\right)\cdot\theta\left(x',y',t\right)\cdot dx'\cdot dy' \quad (6.33a)$$

$$\theta(x,y,t) = \sum_{m=1}^{\infty}\sum_{n=1}^{\infty}\Phi(\beta_m,x)\cdot\Psi(\gamma_n,y)\cdot\bar{\bar{\theta}}(\beta_m,\gamma_n,t) \quad (6.33b)$$

where the functions $\Phi(\beta_m, x)$ and $\Psi(\gamma_n, y)$ are the transformation kernels (normalized eigenfunctions); β_m and γ_n denote infinite lists of eigenvalues in x- and y-directions, respectively.

For convective cooling boundary conditions, the eigenvalues are calculated from transcendental equation [cf. Eq. (4.15)], and the kernels are estimated from Eqs. (4.13) and (4.16).

By applying the method of integral transform, partial differential equation of energy can be transformed into an ordinary differential equation with the following analytical solution

$$T(x,y,t) = T_0 + \sum_{m=1}^{\infty}\sum_{n=1}^{\infty} \Phi(\beta_m, y)\cdot\Psi(\gamma_n, x)\cdot\exp\left(-\frac{\Delta_{m,n}}{\rho c_p}t\right)\left[\int_t \frac{\bar{\bar{g}}(t)}{\rho c_p}\exp\left(\frac{\Delta_{m,n}}{\rho c_p}t\right)dt + C\right] \quad (6.34)$$

where

$$\Delta_{m,n} = \nu_{ec}\frac{I_{cell}}{\mathscr{V}_{cell}}\frac{dV_{oc}}{dT} + \kappa_{eff}\left(\lambda_n^2 + \lambda_m^2\right) - 2h \quad (6.35)$$

$$\bar{\bar{g}} = \int_0^c\int_0^a \Phi(\beta_m, x)\cdot\Psi(\gamma_n, y)\cdot\left[\nu_{ec}\frac{I_{cell}}{\mathscr{V}_{cell}}\left(\frac{\bar{J}}{Y_{ec}} + T_0\frac{dV_{oc}}{dT}\right) + \nu_{elec,p}\,\dot{g}_{ohm,p} + \nu_{elec,n}\,\dot{g}_{ohm,n}\right]dx\,dy \quad (6.36)$$

and the corresponding integrating constant C must be evaluated from the given initial condition, Eq. (6.13).

6.5 Results and discussion

The analytical solutions, presented in Section 6.4, are programmed symbolically in MATHEMATICA (Version 9.0) to obtain a generic solution for the temperature filed. Both analytical and numerical computations are performed on a single processor PC, with a 64-bit quad-core CPU (Core i7) and 10GB of RAM.

6.5.1 Potential and current density distributions

As mentioned in section (6.4), the analytical model does not allow a zero reference potential to be applied on the electrode boundary at the tabs. The absence of a reference potential in the analytical solution yields a positive potential on the negative electrode (with maximum at the tab) and a negative potential on the positive electrode (with minimum at the tab). However, the analytic solution allows one to easily find the maximum potential on the negative electrode, V_n^{max}, and shift the potential distribution on both electrodes such that a reference potential of zero is set at the tab

of negative electrode. The shifted potential distributions read

$$\tilde{V}_n(x,y) = V_n(x,y) - V_n^{\max} \tag{6.37}$$

and

$$\tilde{V}_p(x,y) = \tilde{V}_n(x,y) + V_{\text{oc}} - (\bar{\mathbf{J}}.\mathbf{n}_p)/Y_{ec} \tag{6.38}$$

where Y_{ec} and V_{oc} are functionn of DOD. Note that the solution in Eq. (6.37) only accounts for the potential variation on the negative electrodes due to in-plane electrical resistivity, but the potential solution in Eq. (6.38) takes account for both in-plane electrical resistivity and the through-plane electo-chemical resistivity. The battery voltage with respect to DOD can be evaluated as

$$V_{\text{batt}} = \frac{1}{b}\int_{e_p-\frac{b}{2}}^{e_p+\frac{b}{2}} \tilde{V}_p(x,c)dx \tag{6.39}$$

In Fig. 6.7b potential distributions on positive and negative electrodes, obtained from the analytical model, are shown at $t = 60$s (DOD=5%) during a 3C-rate discharge process. The results show satisfactory agreement with the numerical data shown in Fig. 6.7b.

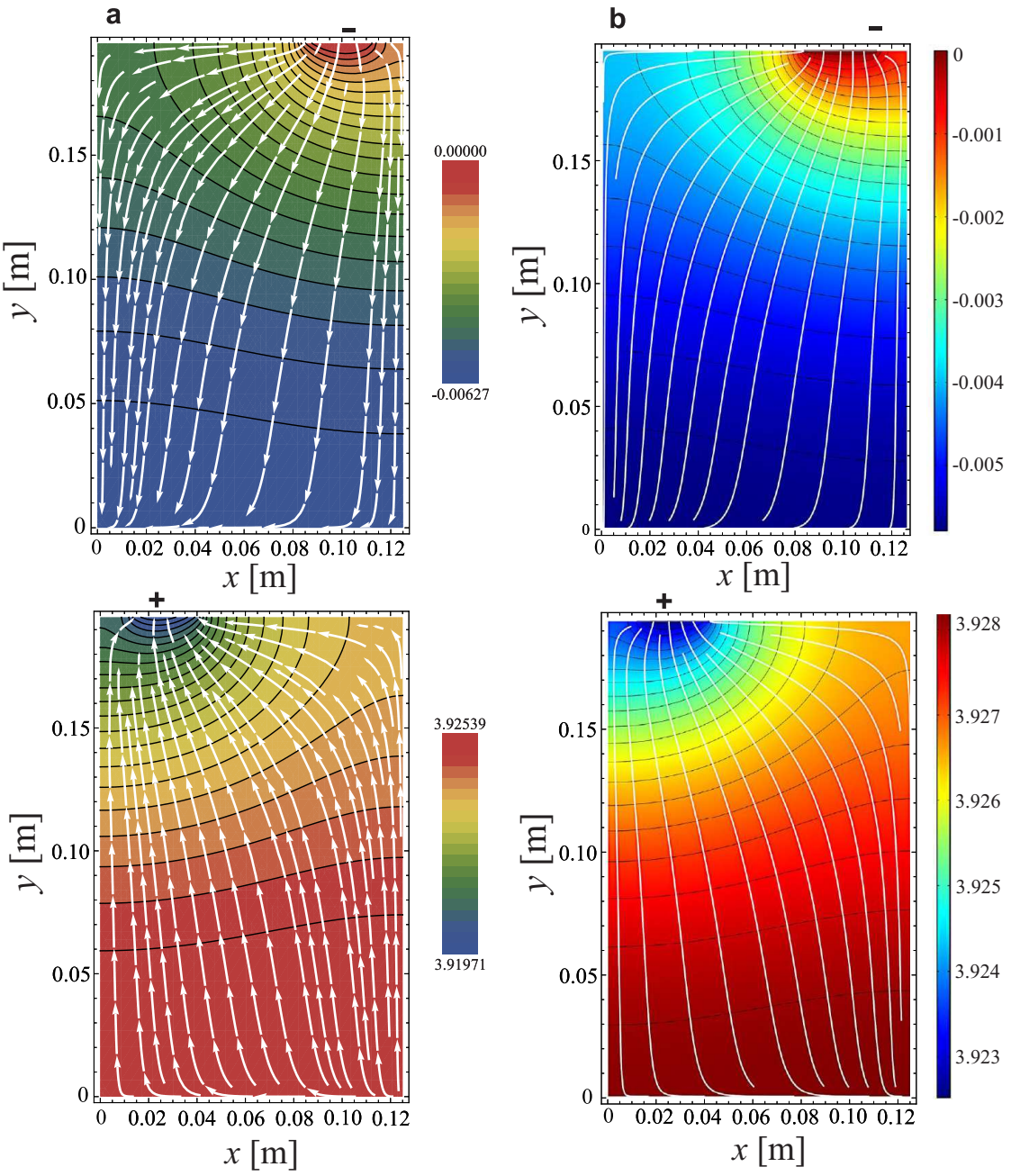

Figure 6.7: The potential distribution on negative electrode and positive electrode, obtained from a) the numerical analysis model and b) proposed analytical, is shown during a 3C-rate discharge process at DOD = 5 %.

The minor difference between the magnitude of potential distribution in analytical and numerical models corresponds to the assumption of a uniform reaction current $\bar{\mathbf{J}}$ in the analytical model instead of a distributed reaction current $J(x,y)$, and also the differences in setting the reference electrode in analytical and numerical approaches.

Figure 6.8a and b compare the magnitude of in-plane current density distribution on negative and positive electrodes obtained analytically (from Eq. (6.40)) and numerically. The results show fair agreement, however, in contrast to the numerical model, in the analytical model since tab boundary conditions are the same [cf. Eq (.6.24d)] the current distribution at the vicinity of the tabs turn out to be similar.

$$|i|_j = \sqrt{i_{x,j}^2 + i_{y,j}^2} \quad (j = p, n) \tag{6.40}$$

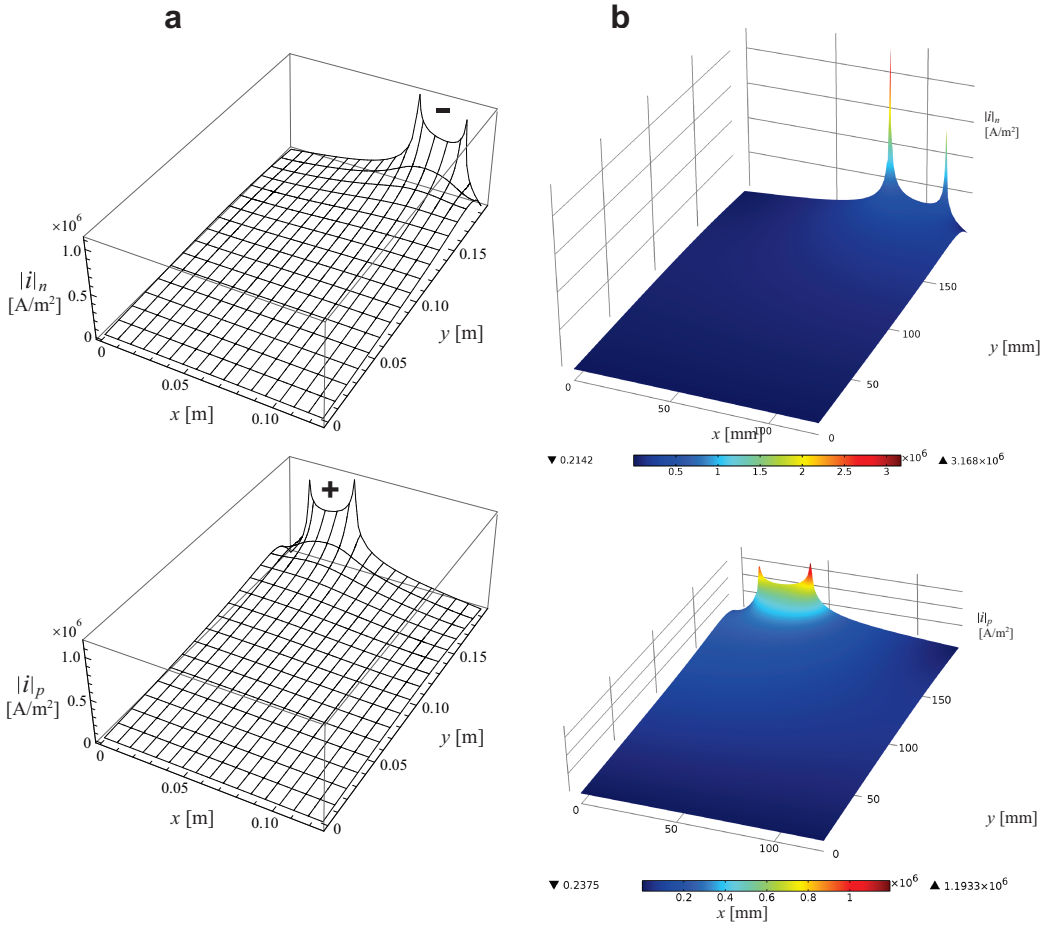

Figure 6.8: The magnitude of in-plane current density distribution on negative and positive electrodes obtained from a) the proposed analytical model and b) numerical analysis, is shown during 3C-rate discharge process at DOD=5%.

6.5.2 Temperature distributions

In this section, the proposed analytical approach is employed to investigate the thermal behavior of the Li-ion cell, and the results, i.e. solution of Eq. (6.34), are compared with experimental temperature measurements and numerical data.

To explain the spatial and temporal temperature behaviour in the battery, we compare the evolution of temperature between three different locations during 1 C, 2 C, and 3 C-discharge processes. Results together with the positions of three monitoring points are depicted in Fig. 6.9.

A small convective heat transfer coefficient, $h = 5\ \mathrm{W\,m^{-2}\,K^{-1}}$, is considered at the surfaces and boundaries of the battery; both ambient and initial conditions are set to $T_0 = 22^{\circ}\mathrm{C}$. Temperature of the corresponding locations measured through experimental study (symbols) and calculated by numerical model (dashed-lines) are used to validate the results of the proposed analytical model (lines). Overall, the analytical results are in well consistency with the data acquired from the experiments and numerical simulations.

The results in Fig. 6.9 indicate the occurrence of the maximum temperature at the location 1 which is due to Joule heating caused by the constriction of the current flow at the vicinity of the tab as it is confirmed in Fig. 6.10 presenting the summation of the polarization and ohmic heat generation rates.

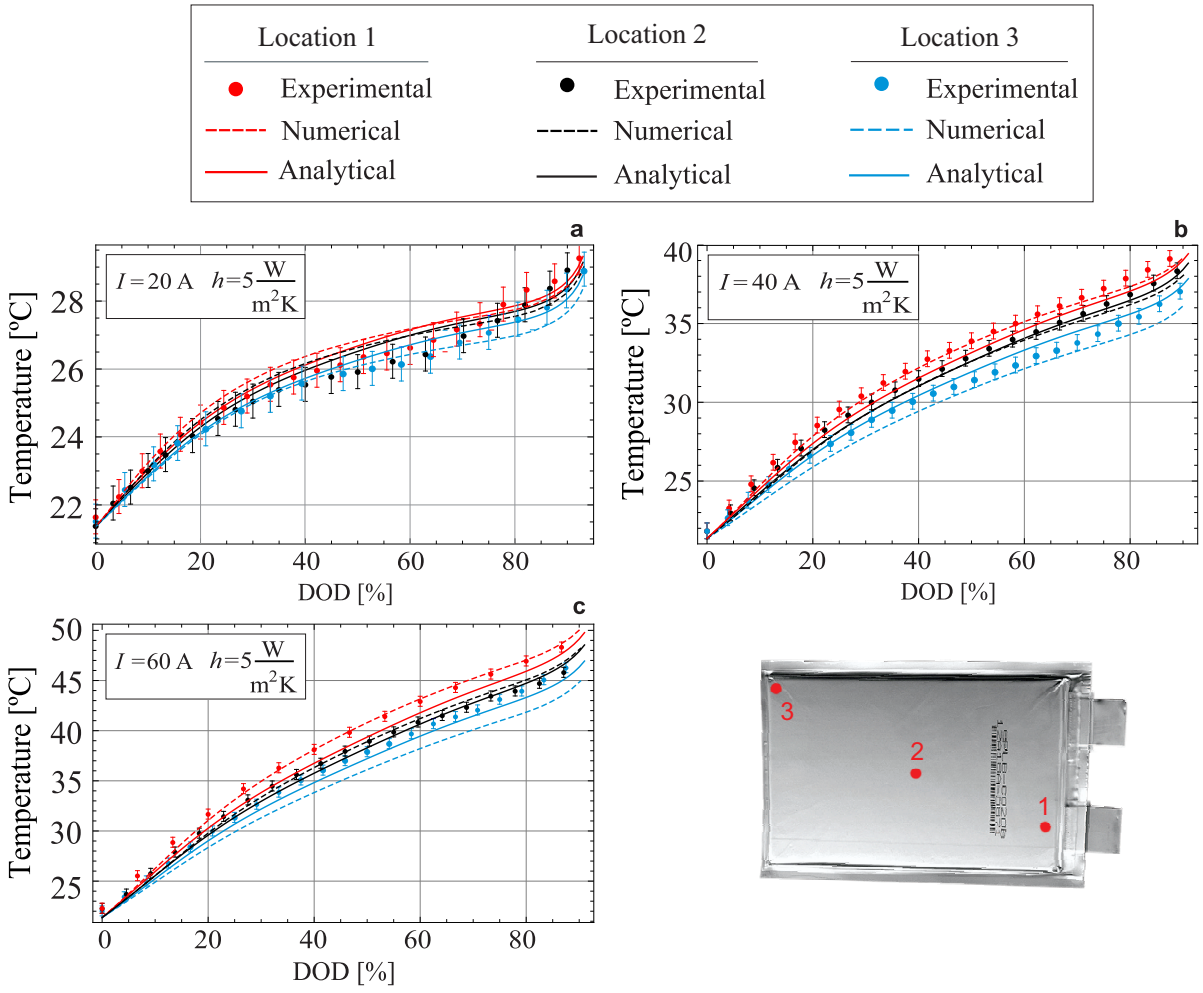

Figure 6.9: Temperature variation versus DOD is shown for different discharge currents. The maximum temperature at the vicinity of the positive electrode's tab (red lines), the centre temperature (black lines), and the minimum temperature at the bottom of the battery (blue lines) are compared with the ones obtained from numerical (dashed lines) and experimental (symbols) studies. A natural convection ($h = 5\ \mathrm{W\,m^{-2}K^{-1}}$) is applied at the surfaces and boundaries of the battery and both ambient and initial temperatures are set to 22°C.

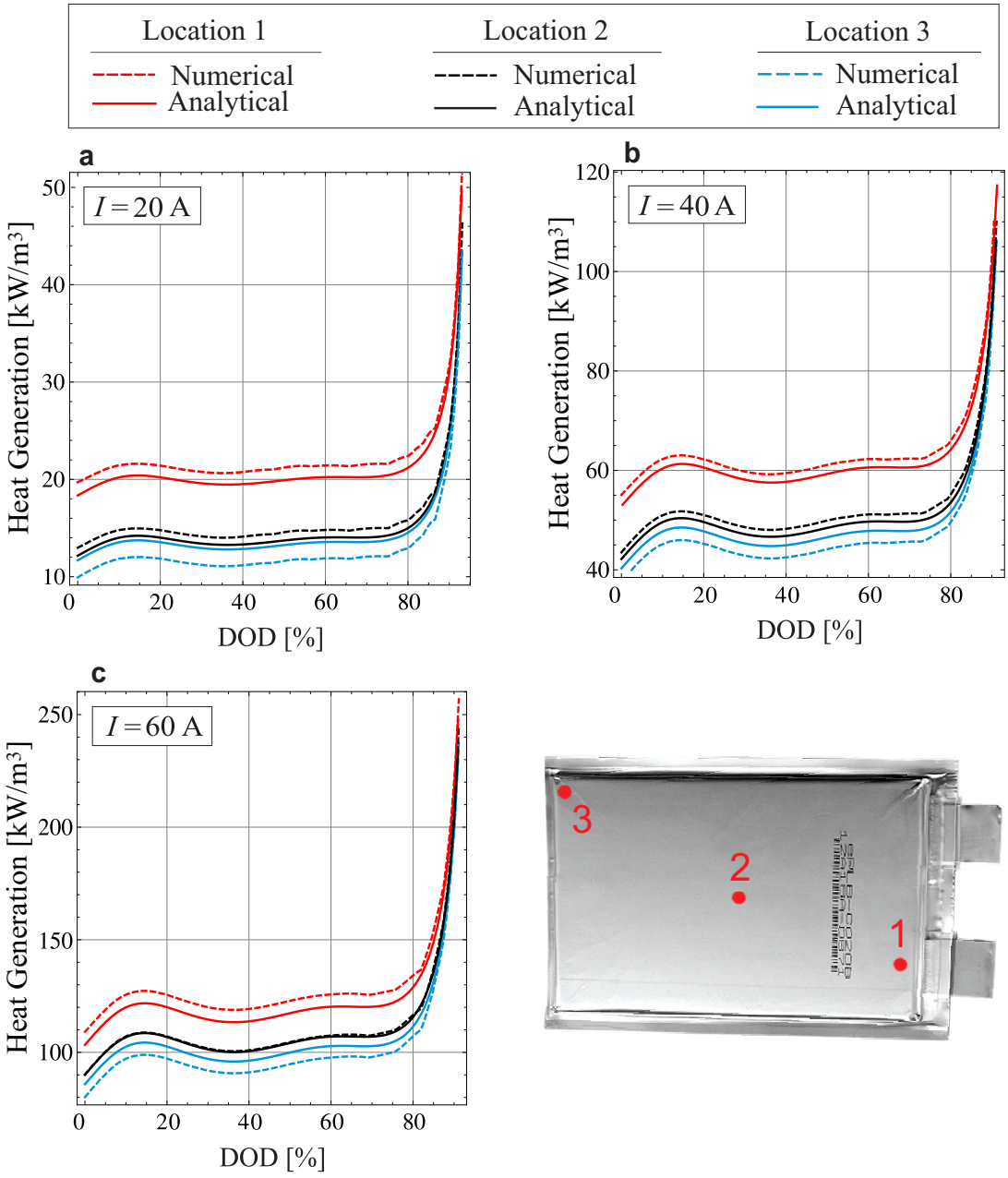

Figure 6.10: Summation of polarization and ohmic heat generation rates versus DOD for different discharge currents calculated at three different locations. The dashed lines represent the numerical data and the solid lines show the ones obtained from Eqs. (6.31) and (6.10).

The spatial variation of the volumetric heat generation rate in the electrode-domain at the end of 1 C, 2 C, and 3 C-discharge processes are plotted in Fig. 6.11. This quantity over the electrode domain volume includes heat from cell overpotential and ohmic losses obtained from Eqs. (6.31) and (6.10). In Fig. 6.11 the highest heat generation rates are established close to the tabs where the electrical current in the electrodes converges to or diverges from the tabs of the cell resulting a higher rate of heat generation owning to higher currents. In consequence, higher temperature for higher heat generation rate can further energize the local transfer reaction which promotes a non-uniform discharge reaction over the cell. Although the ohmic heat from electrical heating in the electrode contributes a relatively small amount, just 8-18% of the total heat generation in the considered battery, depending on the internal electrical path design of a cell, this heat is highly localized which causes spatial non-uniformity in the total heat generation as is shown in Fig. 6.11.

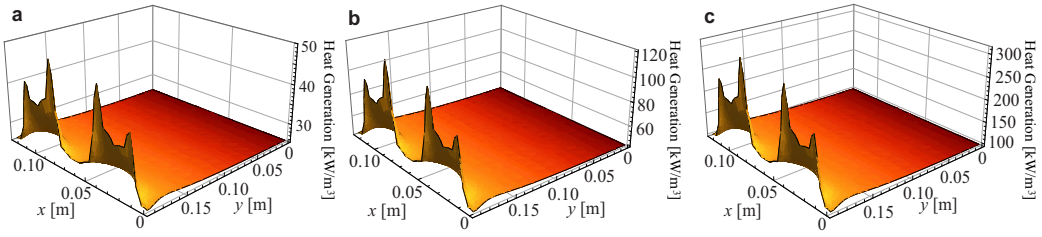

Figure 6.11: Contour of volumetric heat generation rate (irreversible and ohmic heating) in the cell at the end of a) 1C-discharge process, b) 2C-discharge process, and c) 3C-discharge process.

Figure. 6.11 also shows that the heat generation rate in the positive electrode tab is higher than that of the negative electrode tab the reason is that the current collector of positive electrode which is made by the aluminum foil has larger electrical resistivity than the current collector of negative electrode which is made by copper foil, and thus more Joule heat is generated on the positive electrode than on the negative electrode [41].

6.6 Conclusion

In this chapter, a new mathematical procedure was performed to accurately predict the ohmic heating and transient temperature behavior of the battery during galvanostatic processes. The following steps were taken to develop and validate the present model:

- a large lithium-ion battery pouch (20 Ah) was characterized experimentally to obtain its polarization expression,

- transient behavior of the battery during constant current discharge processes was simulated numerically to study the distributions of the reaction current density in the electrode assembly,
- based on the constant current density assumption, the governing equations of the electrical model for positive and negative fields were decoupled, an analytical solution was proposed to approximate the ohmic heat generation in the electrode domains. The assumption required for development of the analytical model was justified by an independent full numerical simulation of the problem,
- a compact series form solution for ohmic heating in the battery was obtained and then coupled to the transient thermal model through heat source term,
- the electro-thermal model was solved analytically using method of integral transformation,
- developed model was validated through comparison with the numerical and experimental studies.

It should be emphasized that a uniform transfer current density was assumed in the presented analytical model which is valid for DOD$<90\%$ confirmed by numerical studies.

The validated model was applied to study the transient thermal response of the battery during standard constant current discharge tests. The results showed that the maximum temperature in the battery arises at the vicinity of the tabs, where the ohmic heat is established as a result of the convergence/divergence of the current streamlines. It was confirmed that ohmic heating in the electrode contributes a relatively small portion (8-18%) of the total heat generation in the considered battery; nonetheless, this highly localized heat can cause spatial non-uniformity in total heat generation and consequently in temperature profile. To conclude, it is important to affirm that the proposed analytical model can be used to study the effect of electrode configurations on the heat generation and temperature profiles.

Chapter 7

Numerical Electro-Thermal Model for Lithium-Ion Batteries

The analytical models proposed in the previous chapters can accurately predict the electro-thermal performance of batteries across constant-current processes. However, the models can not accurately simulate the dynamic response of batteries to transiently changing load profiles. The polarization expression [cf. Eq. (6.14)] used to describe the voltage response of the battery is only a function of DOD and has no time dependent relaxation term. This limitation is addressed in this chapter, where the polarization expression is extended to an equivalent circuit model that enables simulations of the voltage and temperature profiles of the battery across more dynamic profiles.

7.1 Model development

The ECM is a simplified electro-chemical model that can simulate the $I-V$ characteristics of the battery with modest computational effort. Detailed electro-chemical models often require significant memory and computation, which are not desirable for actual BTMS and BMS in electrified vehicles. ECMs, as lumped models, utilize the electrical circuit elements such as voltage source, resistor, and parallel resistance-capacitor (RC) pairs to represent the voltage behaviour of the battery. The number of RC networks in the equivalent circuit is an important factor that determines the accuracy and complexity of the model. The sufficient number of RC branches in the ECM can be defined from the transient response of the cell voltage during the relaxation phase when the pulse

current is removed. Normally, the experimental data is fitted to a few equivalent circuits with different number of RC branches and the circuit that can provide the best match to the experimental data is often selected. The parameters of the ECM are a function of T and SOC and should be identified from a set of characterization tests conducted at different operating conditions. Several characterization test profiles simulate the discharge behaviour of the battery and overlook the charge profile [51–53, 55, 66]. The HPPC profile, as discussed in Chapter 3, is the one that incorporates both discharge and charge pulses [54, 72] to derive the internal resistance and polarization resistances of the cell as a function of SOC with sufficient resolution to reliably establish cell voltage response time constants during discharge, rest, and charge (regen) operating regimes. In this study, the voltage curves obtained from HPPC tests, performed in Chapter 3, are used to characterize the ECM parameters.

7.1.1 ECM parameter estimation

Following Ref. [53], first the number of RC-networks in the model is determined by fitting the model to the transient response of the cell voltage during the relaxation phase when the pulse current is removed. The data is separately fitted to three different models: 1) one RC-network pair (first-order ECM), 2) two pairs of RC-networks (second-order ECM), and 3) three pairs of RC-networks (third-order ECM), the results are presented in Fig. 7.1. The R-squared values for fitted model with one, two, and three pairs of RC networks are 0.907, 0.9912, and 0.995, respectively. The results show that one RC network pair can not produce a satisfactory match to the experimental data. Whereas, the second-order ECM can fit the experimental data with a R-squared value comparable with that of third-order model but with a lower computational cost. Hence, as a compromise between the accuracy and complexity, the model with two pairs of RC networks is selected; the schematic of the considered model is presented in Fig. 7.2. As shown in Fig. 7.2, the model consists of six components: V_{oc}, internal resistance, R_0 and two parallel RC networks each consists of one resistance (R_1, R_2) and capacitance (C_1, C_2), each representing a different aspect of the battery. V_{oc} is the battery open circuit voltage and R_0 is the ohmic or internal resistance of the cell responsible for the immediate voltage drop or rise when the battery is being discharged or charged. Two parallel pairs of RC consisting of R_1, R_2, C_1 and C_2, are responsible for the transient response of the battery. R_1 and C_1 describe the fast dynamics of the battery, depicting the reaction kinetics and the surface effects on the electrodes. Essentially, R_1 is the charge transfer resistance and C_1 represents the

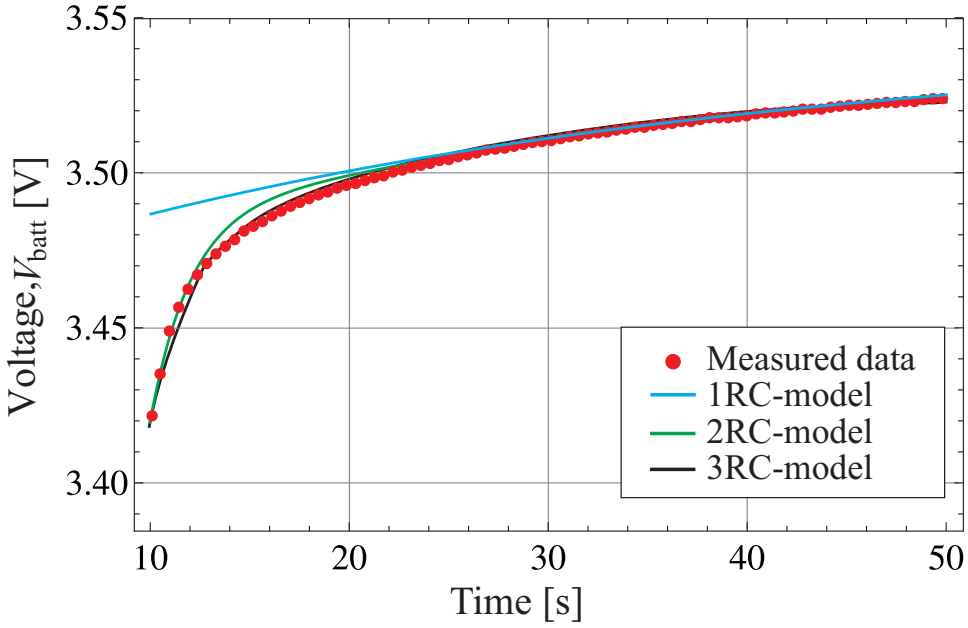

Figure 7.1: Fitting the measured voltage (symbols) during relaxation phase (when HPPC pulse is removed) to first-order (blue line), second-order (green line), and third-order (black line) ECM, to determine the optimum number of RC pairs that can accurately describe the voltage behaviour of the experimental battery with the modest computational effort.

electrochemical double layer capacitance. R_2 and C_2 represent the slower dynamics of the battery, in the order of hours and are more representative of the diffusion processes in the electrolyte and active material.

The electrical behavior of the presented circuit can be formulated as;

$$\phi_{\text{batt}} = V_{\text{oc}} - \phi_0 - \phi_1 - \phi_2 \tag{7.1}$$

where

$$\begin{cases} V_{\text{oc}} = \text{f}(\text{SOC}) \\ \\ \text{SOC} = \text{SOC}_0 - \frac{1}{Q_{\text{cell}}} \cdot \int_0^t I(t) \cdot dt \end{cases} \tag{7.2}$$

From Kirchhoffs law, the three voltage loss terms (ϕ_0, ϕ_1, ϕ_2) read as:

$$\phi_0 = I \cdot R_0 \tag{7.3a}$$

$$\frac{\phi_1}{R_1} + C_1 \frac{\text{d}\phi_1}{\text{d}t} = I_1 \tag{7.3b}$$

$$\frac{\phi_2}{R_2} + C_2 \frac{\text{d}\phi_2}{\text{d}t} = I_2 \tag{7.3c}$$

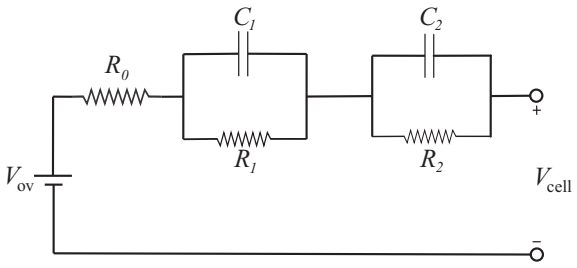

Figure 7.2: Schematic of ECM with two RC-pairs representing the considered Li-ion cell.

Note that ϕ_0 is a function of internal resistance (R_0) whereas ϕ_1 and ϕ_2 are functions of both resistance and capacitance, which account for voltage relaxation effect during dynamic operation of a battery.

The model parameters should be defined from a set of experimental data collected at different T and SOC. The parameter estimation involves two main steps: *i*) cycling the battery with a standard charactrization test (HPPC profile in this study) at different operating temperatures, see Fig. 3.10 *ii*) extracting the parameters from the collected experiments at each temperature and SOC; the details of the procedure are provided in the following paragraphs. The main goal of the parameter estimation process is to find best possible parameter values to make the model match the experimental data. By iteratively comparing the simulation result against experiment data, the model parameters for the specific operating condition can be found as an optimal fit. The procedure is based on an Excel function named LINEST that uses the regressive equations derived from Eq. 7.3 as:

$$\phi_{\text{batt}} = \phi_{\text{oc}} - R_0 I - R_1 I_1 - R_2 I_2 \tag{7.4a}$$

$$\begin{aligned} I_1 = \left[1 - \frac{[1-\exp(-\Delta t/\Delta\tau_1)]}{(\Delta t/\tau_1)}\right] I_i + \left[\frac{[1-\exp(-\Delta\tau_1)]}{(\Delta t/\tau_1)} - \exp(-\Delta t/\Delta\tau_1)\right] I_{i-1} \\ + \exp(-\Delta t/\Delta\tau_1)\, I_{1,i-1} \end{aligned} \tag{7.4b}$$

$$\begin{aligned} I_2 = \left[1 - \frac{[1-\exp(-\Delta t/\Delta\tau_2)]}{(\Delta t/\tau_2)}\right] I_i + \left[\frac{[1-\exp(-\Delta\tau_2)]}{(\Delta t/\tau_2)} - \exp(-\Delta t/\Delta\tau_2)\right] I_{i-1} \\ + \exp(-\Delta t/\Delta\tau_2)\, I_{1,i-1} \end{aligned} \tag{7.4c}$$

where i represents the index for each time step. The fitting process should be performed at each SOC and T. Figure. 7.3 shows a sample of fitting procedure performed at 50% SOC and 0 °C. As reported in Fig. 7.3b, the match between the fitted and measured voltage is excellent with a maximum relative difference (%) between the fitted and measured voltage of 1%.

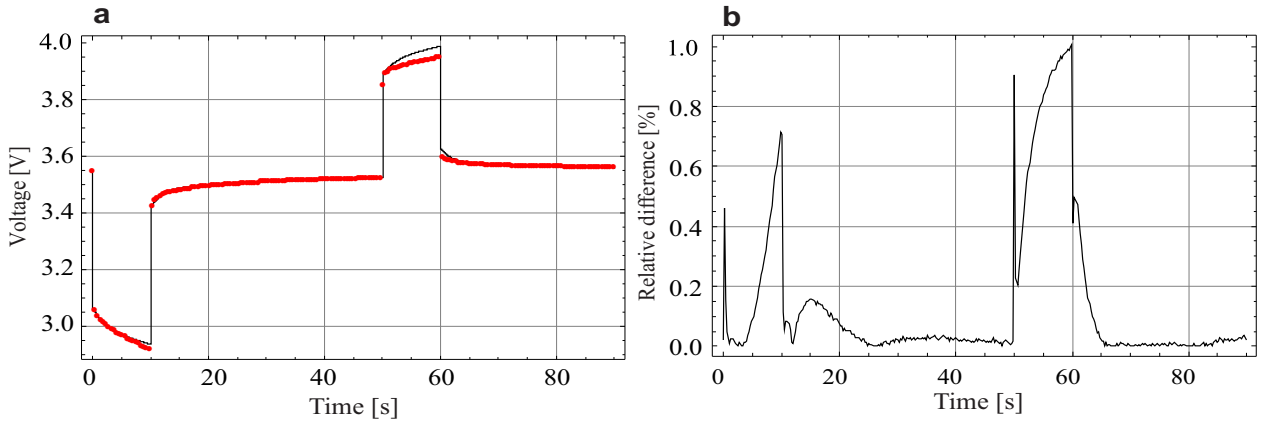

Figure 7.3: Results of the parameter estimation process performed at 50% of SOC and 0 °C. a) Plotted the fitted voltage against the measured voltage and b) the relative difference (%) between the measured and fitted data.

The results of the parameter estimation procedure are plotted in Figure 7.4, which shows the estimated parameters as function of SOC and T.

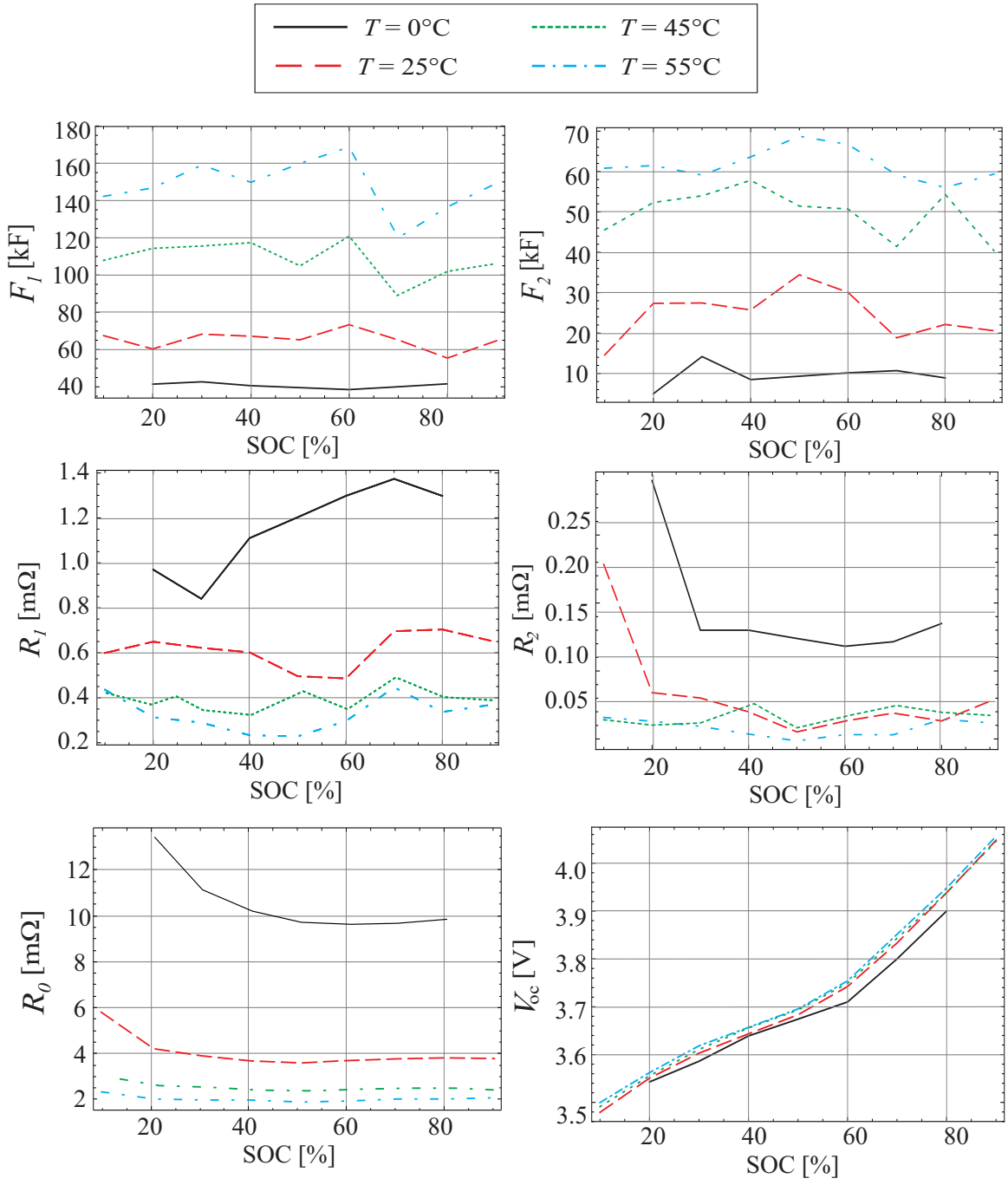

Figure 7.4: Estimated ECM parameters as function of SOC at 0 (black solid line), 25 (green dashed line), 45 (red dashed line), and 55 °C (blue dashed line).

Since SOC and temperature are continuously changing, the model parameters should be updates at each time step by interpolation. A two-dimensional interpolation method is used to fit ECM parameters that are functions of both temperature and SOC.

For comparison, in Fig. 7.5, the cell voltage calculated from Eq (7.1) is plotted against the measured voltage during HPPC cycle at 25 °C. The result implies that by using the estimated parameters provided in Fig. 7.4, the model can capture the battery voltage behaviour across the HPPC profile with a fair accuracy.

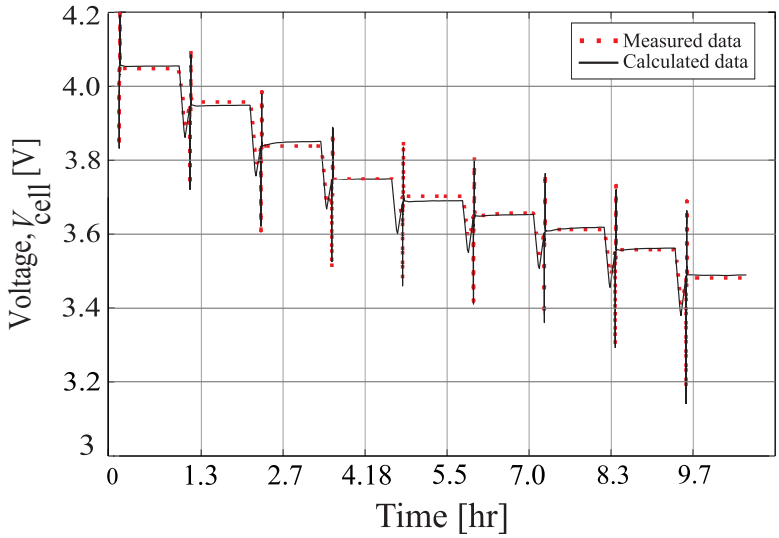

Figure 7.5: Experimental (red dashed line) and simulated (black solid line) voltage response of the battery to HPPC profile at 25 °C.

7.1.2 Electro-thermal model

The schematic of the calculation domains (positive and negative electrode) is presented in Fig. 6.2. The geometry and the mesh in COMSOL MULTIPHYSICS (Version 5.0a) software which is used to solve the governing equations defined on the positive and negative domains. Following Ref. [55], the developed ECM as a zero-dimensional model, is applied to each grid element of the geometry to obtain a distributed behaviour for the current and voltage of the cell. To incorporate all of the small ECMs together, the governing equations for the charge balance, see Eqs. (6.1) and (6.2), are solved in the cell domains. Note that the corresponding boundary conditions detailed in Eqs. (6.4) and (6.5) are still applicable.

In electrode domains where electrochemical reaction occurs ($J \neq 0$), local cell voltage, $\phi_{\text{batt}}(x,y)$ from Eq. (7.3), is the same as the potential difference calculated from the charge balance equations

[cf. Eqs. (6.1) and (6.2)] [55];

$$\phi_{\text{batt}}(x,y) = V_{\text{oc}}(x,y) - \phi_0(x,y) - \phi_1(x,y) - \phi_2(x,y) = V_p(x,y) - V_n(x,y) \tag{7.5}$$

From Eq. (7.5), ϕ_0 can be defined as:

$$\phi_0(x,y) = V_{\text{oc}}(x,y) - (V_p(x,y) - V_n(x,y)) - \phi_1(x,y) - \phi_2(x,y) \tag{7.6}$$

The reaction current density, J, calculated from the polarization expression [cf. Eq. (6.14)] in Chapter 6 can be estimated from Eq. (7.3a) to simulate the $I-V$ characteristics of the battery at transiently changing load profile as opposed to polarization expression that is limited to the galvanostatic processes. Therefore, J can be expressed as:

$$J = \frac{\phi_0}{R_0\, a\, c} \tag{7.7}$$

The transient thermal behaviour of the battery can still be described by the two-dimensional energy equation, Eq. (6.7), and the corresponding boundary and initial conditions, Eqs. (6.12) and (6.13), presented in Chapter 6. Likewise, Eq. (6.9) is used to estimate the net rate of volumetric heat, $\dot{g}$, generated in the battery core.

7.1.3 Results and discussion

The Equations that govern the electro-thermal performance of the cell and simulate the $I-V$ characteristics of the battery, [cf. Eq. (7.3)], form a system of nonlinear equations that can not be solved analytically. Hence, COMSOL MULTIPHYSICS (Version 5.0a), is used to simultaneously solve the governing equations over two separated domains, Ω_p and Ω_n, and to predict the unsteady temperature profile of the Li-ion cell for a given electric load, ambient temperature, and thermal boundary conditions. Experimental validation of the developed multi-physics model at various C-rates (1 C, 2 C, 3 C, 4 C) and temperatures (-10, 0, 25, 40, 55 °C) is presented in Fig. 7.6. Because of the excessive temperature rise (above the safety limit) in the battery during 4 C-rate discharge conducted at 55 °C, the voltage measurement is terminated before completion of the process. The experimental discharge curves agree well with those obtained from the modeling at different environmental temperatures. However, the simulated result starts to deviate from the measured data for the discharge rates above 3 C. This is because it is difficult to handle mass transport limiting phenomena with standard ECM; additional variables such as a Warburg circuit can help to resolve this problem [55], however, this exceeds the scope of this study.

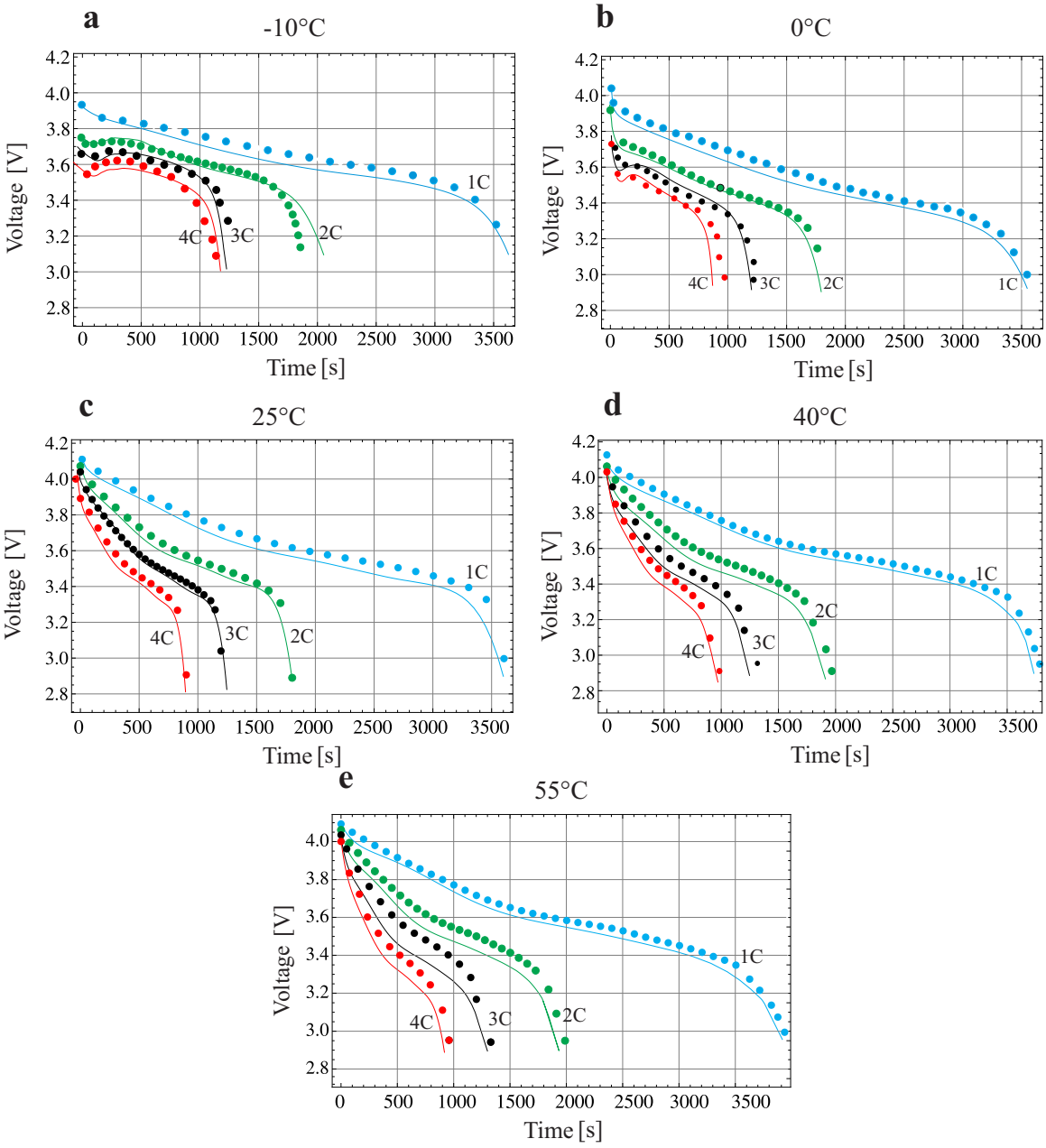

Figure 7.6: The variation of battery voltage versus time for discharge rates of 1 C, 2 C, 3 C, and 4 C at a)−10 °C, b) 0 °C, c) 25 °C, d) 40 °C, e) 55 °C. Symbols correspond to measured values and lines represent calculated values.

The discharge curves in Fig. 7.6 show that the discharge capacity of the cell drops significantly as the temperature decreases below 0 °C. At low temperature the activation energy needed for chemical reactions to occur is higher. The intercalation and deintercalation mechanism at the electrodes need more energy, therefore fewer lithium ions can participate in the active cell process. This leads to a temporary capacity loss. Moreover, low intercalation and deintercalation means a lower cell voltage, which influences the deliverable power from the battery. Nonetheless, the above-mentioned effects are temporary; when the temperature is restored the to desirable level, the capacity and power capabilities are recovered [120].

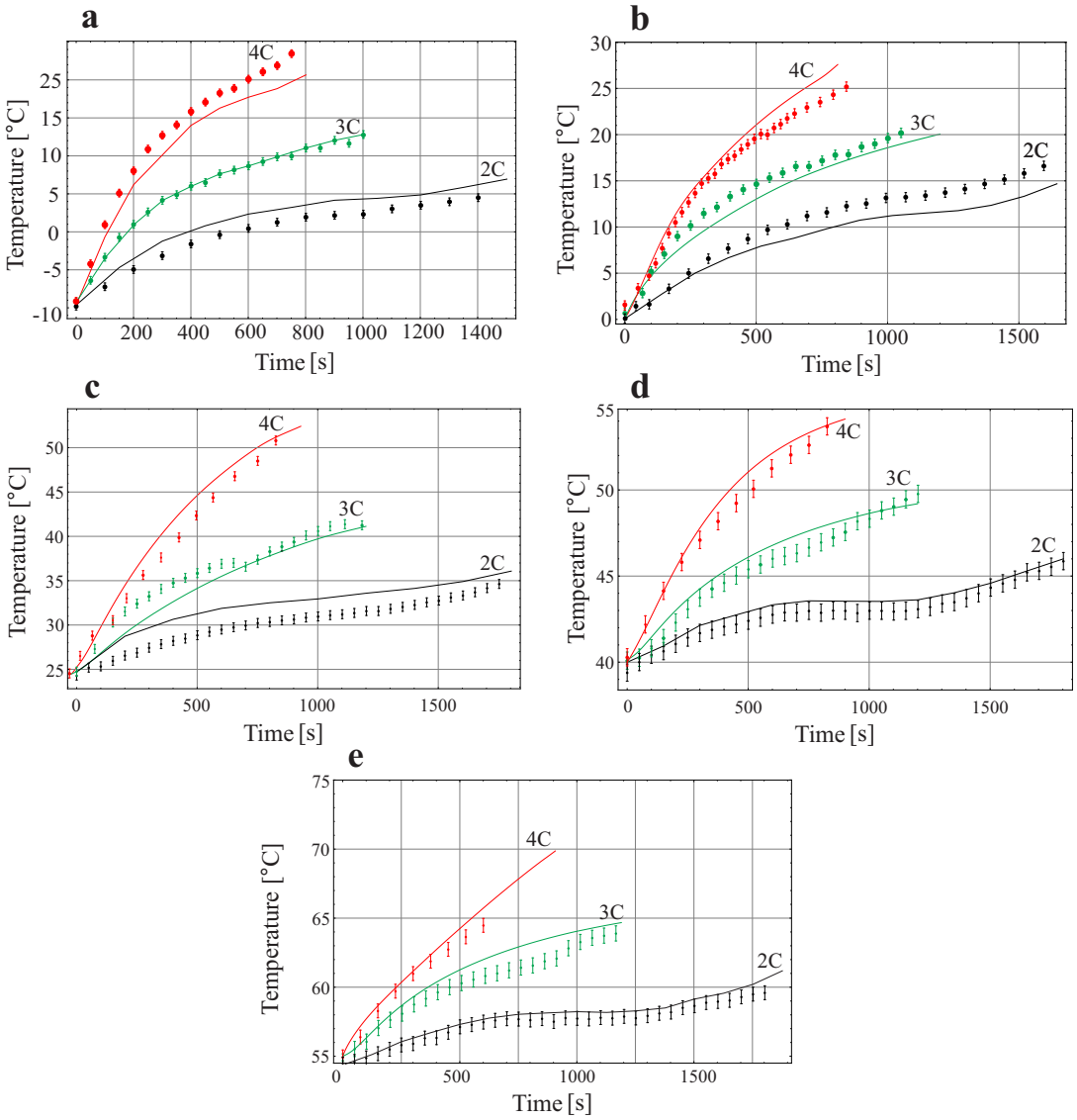

Figure 7.7: The average surface temperature of the battery across different discharge currents of 1 C, 2 C, and 3 C at a)−10 °C, b) 0 °C, c) 25 °C, d) 40 °C, e) 55 °C. Symbols correspond to measured values and lines represent calculated values.

The surface average temperature of the battery as a function of discharge time at different discharge rates is plotted in Figure 7.7. Plots a-e are intended to assess the temperature effect, where cell is discharged at 2 C, 3 C, and 4 C rates in an environment of $-10\,^{\circ}\mathrm{C}$, $0\,^{\circ}\mathrm{C}$, $25\,^{\circ}\mathrm{C}$, $40\,^{\circ}\mathrm{C}$, $55\,^{\circ}\mathrm{C}$. In this study the ambient of $-10\,^{\circ}\mathrm{C}$ is considered as the representative subzero temperature for automotive applications, at which the battery is still capable of delivering reasonable performance. The agreement between the model and experiment is acceptable, except for a slight under-prediction on temperature near the end of the process for 0 and $-10\,^{\circ}\mathrm{C}$ cases. There is a hypothesis that the discrepancy between the predicted and measured data is caused by extremely high sensitivity of cell performance at subfreezing temperatures to operating conditions. Since the cell voltage is lowered with decrease of temperature [see Fig. 7.6], especially at subzero temperatures, cell temperature rise is more marked at a lower ambient temperature due to the higher cell resistance and larger voltage loss [121].

The sensitivity of the discharge performance of the cell at subzero ambient to the heat transfer conditions is investigated in Fig. 7.8, in which the voltage and temperature profiles of the cell simulated at different convective cooling conditions, are plotted against time. Four heat transfer conditions including: adiabatic ($h = 0\ \mathrm{W\,m^{-2}\,K^{-1}}$), $h = 10\ \mathrm{W\,m^{-2}\,K^{-1}}$, $h = 50\ \mathrm{W\,m^{-2}\,K^{-1}}$, and $h = 100\ \mathrm{W\,m^{-2}\,K^{-1}}$ are considered at the ambient of $-10\,^{\circ}\mathrm{C}$. Figure. 7.8 shows that by decreasing the convective cooling coefficient, approaching to adiabatic conditions, the cell capacity increases (10%). The low heat transfer coefficient at $-10\,^{\circ}\mathrm{C}$, implies large cell resistance, and stronger electro-chemical and thermal interaction that leads to a higher temperature rise, and larger performance boost, which is more noticeable near adiabatic conditions (where h approaches zero). In other words, when the cell is operated at sub ambient temperature, the lower the heat transfer coefficient, h, the higher the discharge capacity can be delivered as a result of a faster temperature rise. It can be concluded that an efficient BTMS is necessary to regulate the batteries cooling or heating conditions according to climate conditions. The New European Driving Cycle (NEDC) as a combination of various charge and discharge rates, is used to demonstrate the capability of the model in simulating the dynamic response of the cell to transiently changing load profiles. Figure 7.9 shows a comparison between the experimental test data (dashed lines) and the electro-thermal model prediction (solid lines). The time variation of the current, SOC, average voltage, and average surface temperature are plotted in Fig. 7.9 a, b, c, and d, respectively. The overall electrical and thermal performance obtained from the modeling and experiential studies, are in a fair agreement. At the end of the cycle, the maximum applied discharge current of 4 C, causes a sharp increase in the cell

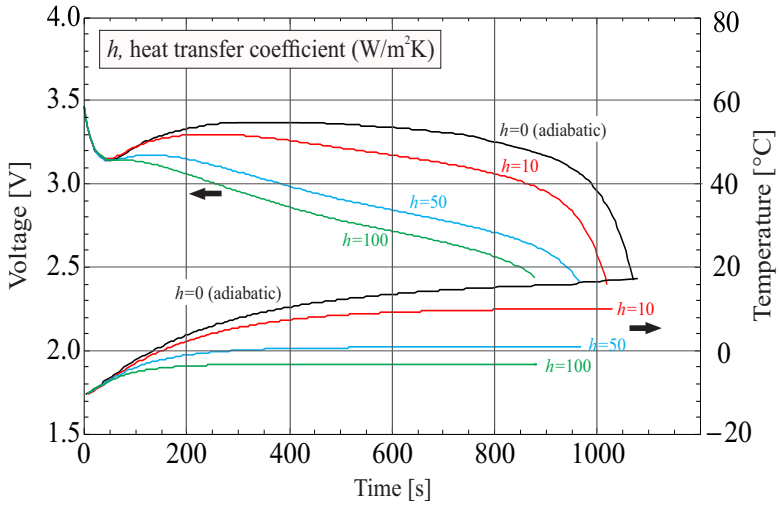

Figure 7.8: Effect of heat transfer coefficient on the temperature and voltage profiles of the cell operates at 3 C discharge process and $-10\,^{\circ}\mathrm{C}$. The battery performance is simulated at four different heat transfer conditions, including: adiabatic ($h = 0\,\mathrm{W\,m^{-2}\,K^{-1}}$), $h = 10\,\mathrm{W\,m^{-2}\,K^{-1}}$, $h = 50\,\mathrm{W\,m^{-2}\,K^{-1}}$, and $h = 100\,\mathrm{W\,m^{-2}\,K^{-1}}$.

temperature, by more than 4°C, and an immediate voltage drop within approximately, 16 s. As predicted in Fig. 7.9 b, during the whole cycle, the capacity of the battery is depleted 20 %, from 100 to 80 % of SOC.

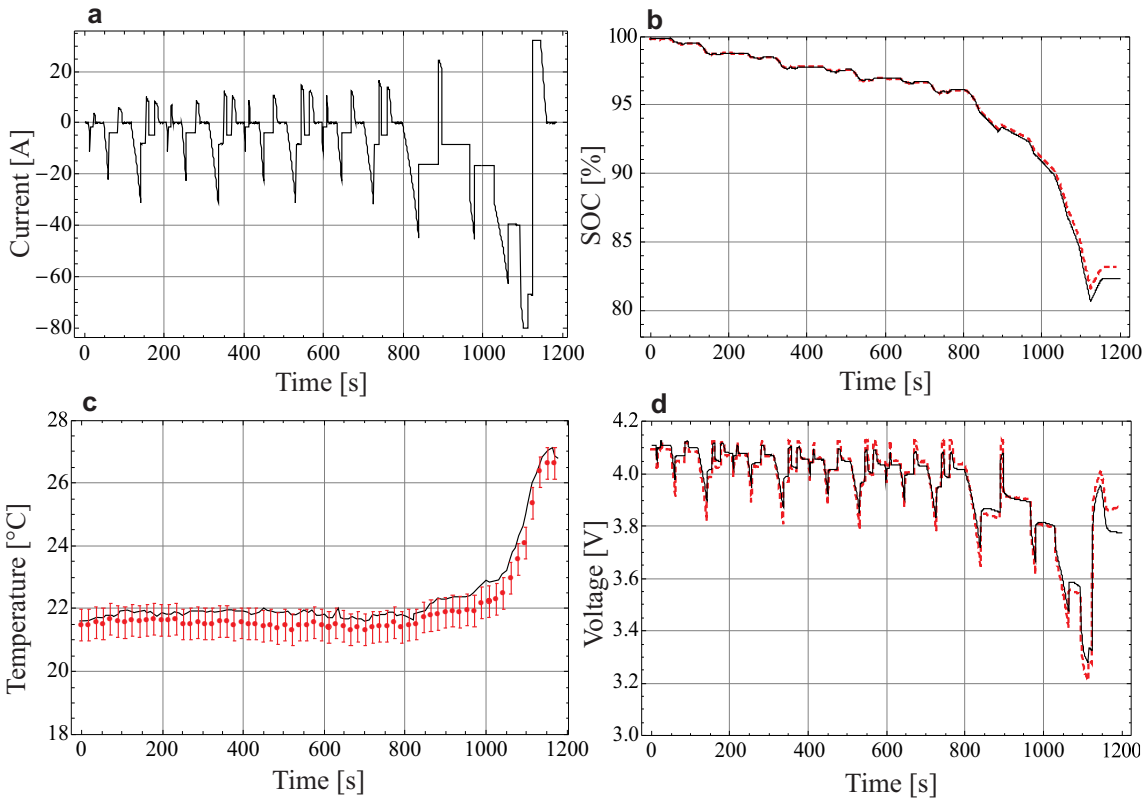

Figure 7.9: Comparison of electro-thermal model prediction (solid lines) with experimental results (dashed lines) conducted at ambient of 21 °C with a convective cooling of 15 W m^{-2} K^{-1}. a) Current (A), b) state-of-charge (%), c) average surface temperature (°C), and d) average voltage (V).

7.2 Conclusion

In this chapter, a numerical multi-physics model was developed that can accurately predict the ohmic heating and transient temperature and voltage behavior of the battery. The model is based on second-order ECM and it is capable of simulating various cell operation modes with good accuracy. The following steps were taken to develop and validate the present model:

- a series of characterization tests (HPPC) was conducted at different environmental temperature,

- using the experimental data, the ECM parameters were determined as a function of temperature and SOC,

- to consider the effect of temperature and SOC on the cell performance, ECM parameters were interpolated by two-dimensional interpolation method,
- the linear polarization expression applied in Chapter 6 was replaced by ECM which enabled us to simulate the voltage response of the cell to transiently changing profiles,
- the ECM was coupled with the electro-thermal model detailed in Chapter 6 to estimate the reaction current density as well as including the effect of temperature on the ECM parameters,
- developed model was validated through comparison with the experimental studies.

The validated model was applied to study the transient thermal response of the battery during standard constant current discharge tests conducted at different environmental temperature (from sub-zero to warm ambient conditions). The results showed that the discharge capacity of the cell drops significantly as the temperature decreases below 0 °C. It means less lithium ions can participate in the active cell process that can lead to a temporary capacity loss. Moreover, at a lower ambient temperature, cell temperature rise was more marked due to the higher the cell resistance and larger voltage loss. The analysis proved that sub ambient temperature, the lower the heat transfer coefficient, h, the higher discharge capacity that can be delivered as a result of a faster temperature rise. It means that an effective BTMS is necessary to regulate the batteries cooling or heating conditions according to climate conditions. To show the capability of the developed model in simulating the dynamic behaviour of the battery, the voltage and temperature response of the cell to New European Driving Cycle was simulated and validated by the experimental data.

Chapter 8

Summary and Future Work

8.1 Summary of thesis

Li-ion batteries are today considered the prime solution as energy storage system for EV/HEVs, due to their high specific energy and power. Since their performance, life and reliability are quite dependent on the operating temperature, great interest has been devoted to thermal models to fully understand the thermal characteristics in the batteries across various operating conditions. The focus of this thesis is to develop a complete range of modeling approaches from full numerical to analytical models as a fast simulation tool for predicting the temperature distribution inside the pouch-type batteries. The presented modeling strategy is divided into two main parts: *i*) analytical solutions, and *ii*) numerical simulations.

In the first part of the study, a series of analytical models is proposed to describe distributions of potential and current density in the electrodes along with the temperature filed in Li-ion batteries during standard galvanostatic processes. First, a three-dimensional analytical solution is developed for temperature profile inside the Li-ion batteries. The solution is used to describe the special and temporal temperature evolution inside a pouch-type Li-ion cell subjected to the convective cooling at its surfaces. The results are successfully verified with the result of an independent numerical simulation. To demonstrate the versatility of the proposed model, the solution is adapted to study the thermal behavior of the prismatic and cylindrical-type NiMH batteries during fast charging processes. Afterward, to resolve the interplay of electrical and thermal processes on the heat generation and thermal processes, a closed-form model is developed for the electrical field inside the battery electrodes. The solution is coupled to the transient thermal model through the heat source term

(Joulean heat). The results of the proposed multi-physics model are validated through comparison with the experimental and numerical studies for standard constant current discharge tests. The model results show that the maximum temperature in the battery arises at the vicinity of the tabs, where the ohmic heat is established as a result of the convergence/divergence of the current streamlines.

In the second part of the study, an equivalent circuit model is developed to simulate the current-voltage characteristics of the battery during transiently changing load profiles. The model that is calibrated by a set of characterization tests collected over a wide range of temperature, then coupled with a numerical electro-thermal model. The validated ECM-based model is capable of predicting the time variation of the surface temperature, voltage, and state of charge (SOC) of the battery during different driving cycles and environmental temperatures.

The list of contributions resulted from the present study is listed below;

- A Distributed analytical electro-thermal model for pouch-type lithium-ion batteries [122],
- Theoretical analysis of potential and current distributions in planar electrodes of lithium-ion batteries [123],
- A computationally-effective thermal model for spirally wound nickel-metal hydride batteries [124],
- Analytical assessment of the thermal behavior of nickel-metal hydride batteries during fast charging [125],
- Electrical constriction resistance in current collectors of large-scale lithium-ion batteries [126],
- Transient three-dimensional thermal model for batteries with thin electrodes [127].

8.2 Future work

Improvements and expansion of the proposed models in this thesis can be made. The empirical equations for the ECM parameters were determined as function of SOC and temperature while the effect of the operating current was neglected that may not be suitable for high power applications. To include this effect, more experiments are necessary to be conducted. In addition, the effect of

the degradation on the battery performance can be studied by adding the available empirical SOH models to the present ECM model. Also, the ECM model can be applied to develop a BMS for the battery pack for monitoring the SOC and SOH.

The developed electro-thermal models have the potential to be adapted to other types of the battery, in terms of chemistry and geometry, for example they can be applied to study the performance of NiMH and cylindrical-shaped batteries across different operating conditions.

Finally, there are many research possibilities on pack level's thermal modeling. Little research has been conducted on pack level, since testing such high power and high capacity battery packs require expensive testing equipment. The models in this study can be extended to a sophisticated large-scale battery pack model, where the non uniformity of the cell temperature and the heating influence of neighbouring cells can be simulated. The model can also provide an insight to the BTMS design by simulating the temperature response of the cell and battery pack to different heating and cooling strategies, including both active and passive systems. Once an efficient BTMS is simulated, the system can be built and its performance across variety of operating conditions can be tested by using the facilities available in *LAEC*.

Bibliography

[1] S. Al Hallaj, H. Maleki, and J.R. Hong, J.S.and Selman. Thermal modeling and design considerations of lithium-ion batteries. *Journal of Power Sources*, 83:1 – 8, 1999. 19, 65

[2] S. Al-Hallaj and J.R. Selman. Thermal modeling of secondary lithium batteries for electric vehicle/hybrid electric vehicle applications. *Journal of Power Sources*, 110:341 – 348, 2002. 4

[3] P.L. Antonucci and V. Antonucci. Electrochemical energy storage, energy storage in the emerging era of smart grids. *InTech*, 2011. 2

[4] Scrosati B. Recent advances in lithium ion battery materials. *Electrochimica Acta*, 45:2461 – 2466, 2000.

[5] N. Baba, H. Yoshida, M. Nagaoka, C. Okuda, and S. Kawauchi. Numerical simulation of thermal behavior of lithium-ion secondary batteries using the enhanced single particle model. *Journal of Power Sources*, 252:214 – 228, 2014.

[6] P.S. Badwal, S.S. Giddey, C Munnings, A. Bhatt, and A.F Hollenkamp. Emerging electrochemical energy conversion and storage technologies. *Frontiers in Chemistry*, 2:2296 – 2646, 2014. 3, 5

[7] D.R. Baker and M.W. Verbrugge. Temperature and current distribution in thin film batteries. *Journal of The Electrochemical Society*, 146:2413 – 2424, 1999. 85

[8] T.M. Bandhauer, S. Garimella, and T.F. Fuller. A critical review of thermal issues in lithium-ion batteries. *Journal of The Electrochemical Society*, 158:R1 – R25, 2011. 6, 18, 20, 44

[9] T.M. Bandhauer, S. Garimella, and T.F. Fuller. Temperature-dependent electrochemical heat generation in a commercial lithium-ion battery. *Journal of Power Sources*, 247:618 – 628, 2014. 6

[10] D. Bernardi, E. Pawlikowski, and J. Newman. A general energy balance for battery systems. *Journal of The Electrochemical Society*, 132:5 – 12, 1985. 19, 68

[11] D. Bernardi, E. Pawlikowski, and J. Newman. A general energy balance for battery systems. *Journal of The Electrochemical Society*, 132:5 – 12, 1985. 40

[12] D. Berndt. *Maintenance-free batteries: lead-acid, nickel/cadmium, nickel/hydride: a handbook of battery technology*. Research Studies Press, New York, 1993. 52

[13] G.G. Botte, B.A. Johnson, and R.E. White. Influence of some design variables on the thermal behavior of a lithium-ion cell. *Journal of The Electrochemical Society*, 146:914 – 923, 1999. 43

[14] L. Cai, Y. Dai, M. Nicholson, R.E. White, K. Jagannathan, and G. Bhatia. Life modeling of a lithium ion cell with a spinel-based cathode. *Journal of Power Sources*, 221:191 – 200, 2013.

[15] H.S. Carslaw and J.C. Jaeger. *Conduction of heat in solids*. Clarendon Press, Oxford, 2 edition, 1959. 40, 93

[16] S. Chacko and Y.M. Chung. Thermal modelling of li-ion polymer battery for electric vehicle drive cycles. *Journal of Power Sources*, 213:296 – 303, 2012. 88, 89

[17] S.C. Chen, C.C. Wan, and Y.Y. Wang. Thermal analysis of lithium-ion batteries. *Journal of Power Sources*, 140:111 – 124, 2005. xiv, 19, 20, 21, 28, 43, 44, 45, 86

[18] Y. Chen and J.W. Evans. Heat transfer phenomena in lithium/polymer electrolyte batteries for electric vehicle application. *Journal of The Electrochemical Society*, 140:1833 – 1838, 1993. 4, 19, 20, 21, 44, 86

[19] Y. Chen and J.W. Evans. Three dimensional thermal modeling of lithium polymer batteries under galvanostatic discharge and dynamic power profile. *Journal of The Electrochemical Society*, 141:2947 – 2955, 1994. 20, 44

[20] Y. Chen and J.W. Evans. Thermal analysis of lithium-ion batteries. *Journal of The Electrochemical Society*, 143:2708 – 2712, 1996. 20, 21, 44

[21] Y.H. Chiang, W.Y. Sean, and J.C. Ke. Online estimation of internal resistance and open-circuit voltage of lithium-ion batteries in electric vehicles. *Journal of Power Sources*, 196:3921 – 3932, 2011.

[22] S. Cho, H. Jeong, C. Han, S. Jin, J.H. Lim, and J. Oh. State-of-charge estimation for lithium-ion batteries under various operating conditions using an equivalent circuit model. *Computers & Chemical Engineering*, 41:1 – 9, 2012. 22, 105

[23] H. Dai, X. Wei, Z. Sun, J. Wang, and W. Gu. Online cell soc estimation of li-ion battery packs using a dual time-scale kalman filtering for ev applications. *Applied Energy*, 95:227 – 237, 2012.

[24] T.S. Dao, C.P. Vyasarayani, and J. McPhee. Simplification and order reduction of lithium-ion battery model based on porous-electrode theory. *Journal of Power Sources*, 198:329 – 337, 2012.

[25] S.K. Das, S. Lau, and L.A. Archer. Sodium-oxygen batteries: a new class of metal-air batteries. *Journal of Materials Chemistry A*, 2:12623 – 12629, 2014. 5

[26] P. De Vidts and R.E. White. Mathematical modeling of a nickel-cadmium cell: Proton diffusion in the nickel electrode. *Journal of Electrochemical Society*, 142:1509 – 1519, 1995.

[27] P. De Vidts and R.E. White. Governing equations for transport in porous electrodes. *Journal of The Electrochemical Society*, 144:1343 – 1353, 1997.

[28] M. Doyle, T.F. Fuller, and J. Newman. Modeling of galvanostatic charge and discharge of the lithium/polymer/insertion cell. *Journal of The Electrochemical Society*, 140:1526 – 1533, 1993. 19, 43

[29] M. Doyle and J. Newman. Analysis of capacityrate data for lithium batteries using simplified models of the discharge process. *Journal of Applied Electrochemistry*, 27:846 – 856, 1997. 92

[30] M. Doyle, J. Newman, A.S. Gozdz, C.N. Schmutz, and J.M. Tarascon. Comparison of modeling predictions with experimental data from plastic lithium ion cells. *Journal of The Electrochemical Society*, 143:1890 – 1903, 1996. 19

[31] M. Dubarry and Liaw B.Y. Development of a universal modeling tool for rechargeable lithium batteries. *Journal of Power Sources*, 174:856 – 860, 2007.

[32] M. Dubarry, N. Vuillaume, and B.Y. Liaw. From single cell model to battery pack simulation for li-ion batteries. *Journal of Power Sources*, 186:500 – 507, 2009. 22

[33] B.L. Ellis and L.F. Nazar. Sodium and sodium-ion energy storage batteries. *Current Opinion in Solid State and Materials Science*, 16:168 – 177, 2012.

[34] S. Elul, Y. Cohen, and D. Aurbach. The influence of geometry in 2d simulation on the charge/discharge processes in li-ion batteries. *Journal of Electroanalytical Chemistry*, 682:53 – 65, 2012.

[35] T.I. Evans and R.E. White. A thermal analysis of a spirally wound battery using a simple mathematical model. *Journal of The Electrochemical Society*, 136:2145 – 2152, 1989. 67

[36] D. Fan and R.E. White. Mathematical modeling of a nickel-cadmium battery: Effects of intercalation and oxygen reactions. *Journal of Electrochemical Society*, 138:2952 – 2960, 1991.

[37] K. Fang, D. Mu, S. Chen, B. Wu, and F. Wu. A prediction model based on artificial neural network for surface temperature simulation of nickel-metal hydride battery during charging. *Journal of Power Sources*, 208:378 – 382, 2012. 68

[38] K.Z. Fang, D.B. Mu, and S. Chen. Thermal behavior of nickel-metal hydride battery during charging at a wide range of ambient temperatures. *Journal of Thermal Analysis and Calorimetry*, 105:383 – 388, 2011. 52, 57

[39] W. Fang, O.J. Kwon, and C.Y. Wang. Electrochemical-thermal modeling of automotive li-ion batteries and experimental validation using a three-electrode cell. *International Journal of Energy Research*, 34:107 – 115, 2010. 6

[40] T.F. Fuller, M. Doyle, and J. Newman. Simulation and optimization of the dual lithium ion insertion cell. *Journal of The Electrochemical Society*, 141:1 – 10, 1994.

[41] L. Gaines and R. Cuenca. Costs of lithium-ion batteries for vehicles. *Argonne National Lab., IL*, 2000.

[42] R.E. Gerver and J.P. Meyers. Three-dimensional modeling of electrochemical performance and heat generation of lithium-ion batteries in tabbed planar configurations. *Journal of The Electrochemical Society*, 158:A835 – A843, 2011. 18, 23, 87

[43] G. Girishkumar, B. McCloskey, A. C. Luntz, S. Swanson, and W. Wilcke. Lithiumair battery: Promise and challenges. *The Journal of Physical Chemistry Letters*, 1:2193 – 2203, 2010. 5

[44] Anode Global Lithium Ion Battery Market (Cathode and Electrolytic solution). - industry analysis, size, share, growth, trends, and forecast 2013 - 2019. *Transparency Market Research, Albany NY United States*, 2013. 10

[45] P.M. Gomadam, J.W. Weidner, R.A. Dougal, and R.E. White. Mathematical modeling of lithium-ion and nickel battery systems. *Journal of Power Sources*, 110:267 – 284, 2002. 61

[46] P.M. Gomadam, R.E. White, and J.W. Weidner. Modeling heat conduction in spiral geometries. *Journal of The Electrochemical Society*, 150:A1339 – A1345, 2003.

[47] J.B. Goodenough. Electrochemical energy storage in a sustainable modern society. *Energy Environ. Sci.*, 7:14 – 18, 2014. 1

[48] H. Gu. Mathematical analysis of a zn/niooh cell. *Journal of The Electrochemical Society*, 130:1459 – 1464, 1983. 23, 24, 87, 88

[49] W. B. Gu and C. Y. Wang. Thermal-electrochemical modeling of battery systems. *Journal of The Electrochemical Society*, 147:2910 – 2922, 2000. 74, 75

[50] W.B. Gu, C.Y. Wang, S.M. Li, M.M. Geng, and B.Y. Liaw. Modeling discharge and charge characteristics of nickelmetal hydride batteries. *Electrochimica Acta*, 44:4525 – 4541, 1999. 52

[51] X.Y. Guang and B.Y. Liaw. Fast charging nickel-metal hydride traction batteries. *Journal of Power Sources*, 101:158 – 166, 2001. 52

[52] M. Guo and R.E. White. A distributed thermal model for a li-ion electrode plate pair. *Journal of Power Sources*, 221:334 – 344, 2013. 82, 86, 87

[53] M. Guo and R.E. White. A distributed thermal model for a li-ion electrode plate pair. *Journal of Power Sources*, 221:334 – 344, 2013.

[54] T.D. Hatchard, D.D. MacNeil, A. Basu, and J.R. Dahn. Thermal model of cylindrical and prismatic lithium-ion cells. *Journal of The Electrochemical Society*, 148:A755 – A761, 2001. 65

[55] H. He, R. Xiong, and J. Fan. Evaluation of lithium-ion battery equivalent circuit models for state of charge estimation by an experimental approach. *Energies*, 4:582 – 598, 2011. 22

[56] H. He, R. Xiong, H. Guo, and S. Li. Comparison study on the battery models used for the energy management of batteries in electric vehicles. *Energy Conversion and Management*, 64:113 – 121, 2012.

[57] H. He, X. Zhang, R. Xiong, Y. Xu, and H. Guo. Online model-based estimation of state-of-charge and open-circuit voltage of lithium-ion batteries in electric vehicles. *Energy*, 39:310 – 318, 2012.

[58] X. Hu, S. Li, and H. Peng. A comparative study of equivalent circuit models for li-ion batteries. *Journal of Power Sources*, 198:359 – 367, 2012. 22

[59] Y. Hu, S. Yurkovich, Y. Guezennec, and B.J. Yurkovich. A technique for dynamic battery model identification in automotive applications using linear parameter varying structures. *Control Engineering Practice*, 17:1190 – 1201, 2009. 22

[60] Y. Hu, S. Yurkovich, Y. Guezennec, and B.J. Yurkovich. Electro-thermal battery model identification for automotive applications. *Journal of Power Sources*, 196:449 – 457, 2011. 20, 22

[61] The Idaho National Laboratory is a U.S. Department of Energy National Laboratory, Idaho Operations Office: Idaho Falls, ID, USA; 2010. *Battery Test Manual For Plug-In Hybrid Electric Vehicles*, 2008. xiv, 35, 105

[62] F.P. Incropera, D.P. DeWitt, T.L. Bergman, and A.S. Lavine. *Fundamentals of Heat and Mass Transfer*. John Wiley & Sons, New York, 6 edition, 2007. 49

[63] Y. Inui, Y. Kobayashi, Y. Watanabe, Y. Watase, and Y. Kitamura. Simulation of temperature distribution in cylindrical and prismatic lithium ion secondary batteries. *Energy Conversion and Management*, 48:2103 – 2109, 2007. 65, 67

[64] D.H. Jeon and S.M. Baek. Thermal modeling of cylindrical lithium ion battery during discharge cycle. *Energy Conversion and Management*, 52:2973 – 2981, 2011.

[65] Y. Ji, Y. Zhang, and C.Y. Wang. Li-ion cell operation at low temperatures. *Journal of The Electrochemical Society*, 160:A636 – A649, 2013. 115

[66] E.E. Kalu and R.E. White. Thermal analysis of spirally wound li/bcx and li/socl2 cells. *Journal of The Electrochemical Society*, 140:23 – 31, 1993.

[67] G.H. Kim, A. Pesaran, and R. Spotnitz. A three-dimensional thermal abuse model for lithium-ion cells. *Journal of Power Sources*, 170:476 – 489, 2007.

[68] G.H. Kim, K. Smith, K.J. Lee, S. Santhanagopalan, and A. Pesaran. Multi-domain modeling of lithium-ion batteries encompassing multi-physics in varied length scales. *Journal of The Electrochemical Society*, 158:A955 – A969, 2011. 6, 87

[69] J. Kim, T.V. Nguyen, and R.E. White. Thermal mathematical modeling of a multicell common pressure vessel nickel hydrogen battery. *Journal of The Electrochemical Society*, 139:2781 – 2787, 1992. 54

[70] U.S. Kim, C.B. Shin, and C.S. Kim. Effect of electrode configuration on the thermal behavior of a lithium-polymer battery. *Journal of Power Sources*, 180:909 – 916, 2008. xiv, 19, 21, 24, 28, 102

[71] U.S. Kim, C.B. Shin, and C.S. Kim. Modeling for the scale-up of a lithium-ion polymer battery. *Journal of Power Sources*, 189:841 – 846, 2009. 21, 24, 44

[72] U.S. Kim, J. Yi, C.B. Shin, T. Han, and S. Park. Modelling the thermal behaviour of a lithium-ion battery during charge. *Journal of Power Sources*, 196:5115 – 5121, 2011. 21, 24

[73] R. Knödler. Thermal properties of sodium-sulphur cells. *Journal of Applied Electrochemical*, 14:39–46, 1984. 56

[74] K.H. Kwon, C.B. Shin, T.H. Kang, and C.S. Kim. A two-dimensional modeling of a lithium-polymer battery. *Journal of Power Sources*, 163:151 – 157, 2006. xiv, 19, 24, 28

[75] L. Lam. A practical circuit based model for state of health estimation of li-ion battery cells in electric vehicles. Master's thesis, Electrical Sustainable Energy, 2011.

[76] L. Lam, P. Bauer, and E. Kelder. A practical circuit-based model for li-ion battery cells in electric vehicle applications. In *Telecommunications Energy Conference (INTELEC), 2011 IEEE 33rd International*, pages 1 – 9, 2011. 113

[77] J. Lee, K.W. Choi, N.P. Yao, and C.C. Christianson. Three dimensional thermal modeling of electric vehicle batteries. *Journal of The Electrochemical Society*, 133:1286 – 1291, 1986. 20, 21, 44

[78] K.H. Lee, E.H. Song, J.Y. Lee, B.H. Jung, and H.S. Lim. Mechanism of gas build-up in a li-ion cell at elevated temperature. *Journal of Power Sources*, 132:201 – 205, 2004. 6

[79] K.J. Lee, K. Smith, and G.H. Pesaran, A.and Kim. Three dimensional thermal-, electrical-, and electrochemical-coupled model for cylindrical wound large format lithium-ion batteries. *Journal of Power Sources*, 241:20 – 32, 2013.

[80] C. Léger, C. Tessier, M. Ménétrier, C. Denage, and C. Delmas. Investigation of the second discharge plateau of the β(III)-NiOOH / β(II)-Ni(OH)$_2$ system. *Journal of Electrochemical Society*, 146:924 – 932, 1999.

[81] D. Li, K. Yang, S. Chen, and F. Wu. Thermal behavior of overcharged nickel/metal hydride batteries. *Journal of Power Sources*, 184:622 – 626, 2008. 52, 55, 57, 65

[82] X. Li, M. Xiao, and S.Y. Choe. Reduced order model (rom) of a pouch type lithium polymer battery based on electrochemical thermal principles for real time applications. *Electrochimica Acta*, 97:66 – 78, 2013. 19

[83] X. Lin, H.E. Perez, S. Mohan, J.B. Siegel, A.G. Stefanopoulou, Y. Ding, and M.P. Castanier. A lumped-parameter electro-thermal model for cylindrical batteries. *Journal of Power Sources*, 257:1 – 11, 2014. 21, 23, 105

[84] David Linden and Thomas B. Reddy. *Handbook of batteries*. McGraw-Hill, New York, third edition edition, 2011. 6, 16

[85] Gregory L.P. Extended kalman filtering for battery management systems of lipb-based hev battery packs: Part 2. modeling and identification. *Journal of Power Sources*, 134:262 – 276, 2004. 22

[86] R. Mahamud and C. Park. Spatial-resolution, lumped-capacitance thermal model for cylindrical li-ion batteries under high biot number conditions. *Applied Mathematical Modelling*, 37:2787 – 2801, 2013. 65

[87] .G. Miranda and C.W. Hong. Integrated modeling for the cyclic behavior of high power li-ion batteries under extended operating conditions. *Applied Energy*, 111:681 – 689, 2013. 21, 22, 23

[88] S. Motupally, C.C. Streinz, and J.W. Weidner. Proton diffusion in nickel hydroxide: Prediction of active material utilization. *Vidts*, 145:29 – 34, 1998.

[89] P. Liu M.W. Verbrugge. Electrochemical characterization of high-power lithium ion batteries using triangular voltage and current excitation sources. *Journal of Power Sources*, 174:2 – 8, 2007. 22

[90] R.S. Conell M.W. Verbrugge. Electrochemical and thermal characterization of battery modules commensurate with electric vehicle integration. *Journal of The Electrochemical Society*, 149:A45 – A53, 2002.

[91] P. Nelson, I. Bloom, K. Amine, and G. Henriksen. Design modeling of lithium-ion battery performance. *Journal of Power Sources*, 110:437 – 444, 2002. 49

[92] J. Newman and K.E. Thomas-Alyea. *Electrochemical systems*. John Wiley, New Jersey, 3rd edition, 2004. 43

[93] J. Newman and W. Tiedemann. Porous-electrode theory with battery applications. *AIChE Journal*, 21:25 – 41, 1975.

[94] J. Newman and W. Tiedemann. Potential and current distribution in electrochemical cells: Interpretation of the half-cell voltage measurements as a function of reference-electrode location. *Journal of The Electrochemical Society*, 140:1961 – 1968, 1993. 85, 87

[95] J. Newman and W. Tiedemann. Temperature rise in a battery module with constant heat generation. *Journal of The Electrochemical Society*, 142:1054 – 1057, 1995. 20

[96] K. Onda, T. Ohshima, M. Nakayama, K. Fukuda, and T. Araki. Thermal behavior of small lithium-ion battery during rapid charge and discharge cycles. *Journal of Power Sources*, 158:535 – 542, 2006. 13

[97] M. Ouyang, G. Liu, L. Lu, J. Li, and X. Han. Enhancing the estimation accuracy in low state-of-charge area: A novel onboard battery model through surface state of charge determination. *Journal of Power Sources*, 270:221 – 237, 2014. 22

[98] M. N. Özisik. *Boundary value problems of heat conduction*. Dover Publications, New York, 1989. 40, 41, 42, 70, 71, 72, 93

[99] C.R. Pals and J. Newman. Thermal modeling of the lithium/polymer battery: I. discharge behavior of a single cell. *Journal of The Electrochemical Society*, 142:3274 – 3281, 1995. 20, 21, 44

[100] S. Panchal. Impact of vehicle charge and discharge cycles on the thermal characteristics of lithium-ion batteries. Master's thesis, University of Waterloo, Waterloo, Ontario, Canada, 2014. 4, 15, 18

[101] Ahmad A. Pesaran. Battery thermal models for hybrid vehicle simulations. *Journal of Power Sources*, 110:377 – 382, 2002. 6

[102] V. Ramadesigan, P.W.C. Northrop, S. De, S. Santhanagopalan, R.D. Braatz, and V.R. Subramanian. Modeling and simulation of lithium-ion batteries from a systems engineering perspective. *Journal of The Electrochemical Society*, 159:R31 – R45, 2012.

[103] V. Ramadesigan, P.W.C. Northrop, S. De, S. Santhanagopalan, R.D. Braatz, and V.R. Subramanian. Modeling and simulation of lithium-ion batteries from a systems engineering perspective. *Journal of The Electrochemical Society*, 159:R31 – R45, 2012.

[104] L. Rao and J. Newman. Heat generation rate and general energy balance for insertion battery systems. *Journal of The Electrochemical Society*, 144:2697 – 2704, 1997.

[105] L. Rao and J. Newman. Heat generation rate and general energy balance for insertion battery systems. *Journal of The Electrochemical Society*, 144:2697 – 2704, 1997.

[106] J. Remmlinger, M. Buchholz, M. Meiler, P. Bernreuter, and K. Dietmayer. State-of-health monitoring of lithium-ion batteries in electric vehicles by on-board internal resistance estimation. *Journal of Power Sources*, 196:5357 – 5363, 2011. 22

[107] D.R. Rolison and L.F. Nazar. Electrochemical energy storage to power the 21st century. *MRS Bulletin*, 36:486 – 493, 2011. 1

[108] D. Kang S. Jung. Multi-dimensional modeling of large-scale lithium-ion batteries. *Journal of Power Sources*, 248:498 – 509, 2014. 21, 22, 23, 105, 110, 111

[109] R. Sabbah, R. Kizilel, J.R. Selman, and S. Al-Hallaj. Active (air-cooled) vs. passive (phase change material) thermal management of high power lithium-ion packs: Limitation of temperature rise and uniformity of temperature distribution. *Journal of Power Sources*, 182:630 – 638, 2008. 45

[110] Vishal Sapru. 2020 vison: Global lithium-ion battery market. *Transparency Market Research, Albany NY United States*, August 2014. xv, 10

[111] N. Sato and K. Yagi. Thermal behavior analysis of nickel metal hydride batteries for electric vehicles. *JSAE Review*, 21:205 – 211, 2000. 68

[112] L.H. Saw, Y. Ye, and A.A.O. Tay. Electro-thermal characterization of lithium iron phosphate cell with equivalent circuit modeling. *Energy Conversion and Management*, 87:367 – 377, 2014. 21, 22, 23, 105

[113] W. Schalkwijk and B. Scrosati. *Advances in Lithium-Ion Batteries*. Springer US, 2002. 18

[114] D.A. Scherson and A. Palencsar. Batteries and electrochemical capacitors. *The Electrochemical Society Interface*, pages 17 – 22, Spring 2006. xv, 2

[115] B. Scrosati and J. Garche. Lithium batteries: Status, prospects and future. *Journal of Power Sources*, 195:2419 – 2430, 2010. 1

[116] J. Shi, F. Wu, S. Chen, and C. Zhang. Thermal analysis of rapid charging nickel/metal hydride batteries. *Journal of Power Sources*, 157:592 – 599, 2006. xiv, xix, 53, 55, 65, 66, 67, 68, 69, 73, 74, 75

[117] J. Shi, F. Wu, D. Hu, S. Chen, L. Mao, and G. Wang. The influence of hydrogen intercalation on inner pressure of ni/mh battery during fast charge. *Journal of Power Sources*, 161:693 – 701, 2006. 52

[118] K. Smith and C.Y. Wang. Power and thermal characterization of a lithium-ion battery pack for hybrid-electric vehicles. *Journal of Power Sources*, 160:662 – 673, 2006. 49

[119] K.A. Smith, C.D. Rahn, and Chao-Yang W. Model-based electrochemical estimation and constraint management for pulse operation of lithium ion batteries. *Control Systems Technology, IEEE Transactions on*, 18:654 – 663, 2010.

[120] K. Somasundaram, E. Birgersson, and A.S. Mujumdar. Thermalelectrochemical model for passive thermal management of a spiral-wound lithium-ion battery. *Journal of Power Sources*, 203:84 – 96, 2012.

[121] L. Song and J.W. Evans. The thermal stability of lithium polymer batteries. *Journal of The Electrochemical Society*, 145:2327 – 2334, 1998. 20, 21

[122] L. Song and J.W. Evans. Electrochemical-thermal model of lithium polymer batteries. *Journal of The Electrochemical Society*, 147:2086 – 2095, 2000.

[123] V.R. Subramanian, V. Boovaragavan, and V.D. Diwakar. Toward real-time simulation of physics based lithium-ion battery models. *Electrochemical and Solid-State Letters*, 10:A255 – A260, 2007. 19

[124] H. Sun, X. Wang, B. Tossan, and R. Dixon. Three-dimensional thermal modeling of a lithium-ion battery pack. *Journal of Power Sources*, 206:349 – 356, 2012. 21, 22, 23, 105

[125] S. Szpak, C.J. Gabriel, and J.R. Driscoll. Catastrophic thermal runaway in lithium batteries. *Electrochimica Acta*, 32:239 – 246, 1987. 6

[126] K.P. Ta and J. Newman. Proton intercalation hysteresis in charging and discharging nickel hydroxide electrodes. *Journal of Electrochemical Society*, 146:2769 – 2779, 1999.

[127] P. Taheri, A. Mansouri, B. Schweitzer, M. Yazdanpour, and M. Bahrami. Electrical constriction resistance in current collectors of large-scale lithium-ion batteries. *Journal of The Electrochemical Society*, 160:A1731 – A1740, 2013. 120

[128] P. Taheri, M. Yazdanpour, and M. Bahrami. Transient three-dimensional thermal model for batteries with thin electrodes. *Journal of Power Sources*, 243:280 – 289, 2013. 120

[129] P. Taheri, M. Yazdanpour, and M. Bahrami. Analytical assessment of the thermal behavior of nickel metal hydride batteries during fast charging. *Journal of Power Sources*, 245:712 – 720, 2014. 120

[130] Peyman Taheri, Abraham Mansouri, Maryam Yazdanpour, and Majid Bahrami. Theoretical analysis of potential and current distributions in planar electrodes of lithium-ion batteries. *Electrochimica Acta*, 133:197 – 208, 2014. 120

[131] A.K. Thapa, G. Park, H. Nakamura, T. Ishihara, N. Moriyama, T. Kawamura, H. Wang, and M. Yoshio. Novel graphite/tio2 electrochemical cells as a safe electric energy storage system. *Electrochimica Acta*, 55:7305 – 7309, 2010. 6

[132] M.W. Verbrugge and R.S. Conell. Electrochemical and thermal characterization of battery modules commensurate with electric vehicle integration. *Journal of The Electrochemical Society*, 149:A45 – A53, 2002. 7, 20, 21

[133] V.D. Diwakar V.R. Subramanian, V. Boovaragavan. Toward real-time simulation of physics based lithium-ion battery models. *Electrochemical and Solid-State Letters*, 10:A255 – A260, 2007.

[134] J. Newman W. Tiedemann. Electrochemical characterization of high-power lithium ion batteries using triangular voltage and current excitation sources. *The Electrochemical Society Proceeding Series, Pennington, NJ*, pages 39 – 49, 1979. 87

[135] S. Wang, M. Verbrugge, J.S. Wang, and P. Liu. Multi-parameter battery state estimator based on the adaptive and direct solution of the governing differential equations. *Journal of Power Sources*, 196:8735 – 8741, 2011.

[136] W. Wang, Q. Luo, B. Li, X. Wei, L. Li, and Z. Yang. Recent progress in redox flow battery research and development. *Advanced Functional Materials*, 23:970 – 986, 2013. 5

[137] J.W. Weidner and P. Timmerman. Effect of proton diffusion, electron conductivity, and charge-transfer resistance on nickel hydroxide discharge curves. *Journal of Electrochemical Society*, 141:346 – 351, 1994.

[138] Inc. Wolfram Research. *Mathematica Edition: Version 9.0*. Wolfram Research, Inc., Champaign, Illinois, 2012. 73

[139] B. Wu, Z. Li, and J. Zhang. Thermal design for the pouch-type large-format lithium-ion batteries: I. thermo-electrical modeling and origins of temperature nonuniformity. *Journal of The Electrochemical Society*, 162:A181 – A191, 2015. 21, 24

[140] B. Wu, M. Mohammed, D. Brigham, R. Elder, and R.E. White. A non-isothermal model of a nickel-metal hydride cell. *Journal of Power Sources*, 101:149 – 157, 2001. 52, 55, 61

[141] M. S. Wu, Y. H. Hung, Y. Y. Wang, and C. C. Wan. Heat dissipation behavior of the nickel/metal hydride battery. *Journal of Electrochemical Society*, 147:930 – 935, 2000. 52

[142] M.S. Wu, Y.Y. Wang, and C.C. Wan. Thermal behaviour of nickel/metal hydride batteries during charge and discharge. *Journal of Power Sources*, 74:202 – 210, 1998. xiv, xviii, 53, 54, 56, 57, 58, 61, 62

[143] S.Y. Choe X. Li, M. Xiao. Reduced order model (rom) of a pouch type lithium polymer battery based on electrochemical thermal principles for real time applications. *Journal of The Electrochemical Society*, 97:66 – 78, 2013.

[144] H. Yang, S. Kannappan, A.S. Pandian, J.-H. Jang, Y.S. Lee, and W. Lu. Achieving Both High Power and Energy Density in Electrochemical Supercapacitors with Nanoporous Graphene Materials. *ArXiv e-prints*, 2013.

[145] M. Yazdanpour, P. Taheri, and M. Bahrami. A computationally-effective thermal model for spirally wound nickel-metal hydride batteries. *Journal of Electrochemical Society*, 161:A109 – A117, 2014. 120

[146] P. Yazdanpour, M.and Taheri, A. Mansouri, and M. Bahrami. A distributed analytical electro-thermal model for pouch-type lithium-ion batteries. *Journal of The Electrochemical Society*, 161:A1953 – A1963, 2014. 120

[147] Y. Ye, N. Shi, Y.and Cai, J. Lee, and X. He. Electro-thermal modeling and experimental validation for lithium ion battery. *Journal of Power Sources*, 199:227 – 238, 2012. 49

[148] J. Yi, U.S. Kim, C.B. Shin, T. Han, and S. Park. Modeling the temperature dependence of the discharge behavior of a lithium-ion battery in low environmental temperature. *Journal of Power Sources*, 244:143 – 148, 2013. 21, 24, 88, 89

[149] J. Yi, U.S. Kim, C.B. Shin, T. Han, and S. Park. Three-dimensional thermal modeling of a lithium-ion battery considering the combined effects of the electrical and thermal contact resistances between current collecting tab and lead wire. *Journal of The Electrochemical Society*, 160:A437 – A443, 2013.

[150] H.P. Zhang, P. Zhang, Z.H. Li, M. Sun, Y.P. Wu, and H.Q. Wu. A novel sandwiched membrane as polymer electrolyte for lithium ion battery. *Electrochemistry Communications*, 9:1700 – 1703, 2007. 11

[151] S.S. Zhang, K. Xu, and T.R Jow. A new approach toward improved low temperature performance of li-ion battery. *Electrochemistry Communications*, 4:928 – 932, 2002. 6